Pressure-Shear Plate Impact Experiments on High-Purity Aluminum at Temperatures Approaching Melt

by

Stephen E. Grunschel

B.S., University of Illinois, 2001

Sc.M., Applied Math, Brown University, 2009

Thesis

Submitted in partial fulfillment of the requirements

for the degree of Doctor of Philosophy

in the Division of Engineering at Brown University

Providence, RI
May 2009

This dissertation by Stephen E. Grunschel is accepted in its present form by the Division of Engineering as satisfying the dissertation requirement for the degree of Doctor of Philosophy.

Date _____ _____
Professor Rodney J. Clifton, Advisor

Recommended to the Graduate Council

Date _____ _____
Professor Kyung-Suk Kim, Reader

Date _____ _____
Professor Clyde L. Briant, Reader

Approved by the Graduate Council

Date _____ _____
Shiela Bonde
Dean of the Graduate School

Vita

Stephen E. Grunschel was born in Arlington Heights, Illinois on July 5, 1979. He graduated with a B.S. in Engineering Mechanics from University of Illinois (Urbana-Champaign) in 2001. He then joined the Division of Engineering at Brown University as a graduate student where, for the duration of his time at Brown, he held a research assistantship under Professor Rodney J. Clifton. He received a Sc.M. degree in Applied Mathematics from Brown University in 2009.

Acknowledgements

First and foremost I would like to acknowledge my advisor Prof. Clifton. He approached all problems, scientific or otherwise, with careful, rational thought, ensuring the basic groundwork to a solution was sound before proceeding. This approach was paramount to my development as a researcher, since I was initially overexcited to get results. His patience and impartial, unassuming attitude has influenced me greatly. I am truly fortunate to have had him as my advisor.

I would like to thank Prof. Kim and Prof. Briant for agreeing to be my committee members. They are both extremely busy people and I am thankful that they were able to make time read my thesis. Their comments were very much appreciated.

I have enjoyed my time working in the Brown University plate-impact facility and during my tenure here, I have benefitted greatly from my interactions with fellow labmates – Tonia Jiao, Sean Teller, Zhizhou Zhang and Al Rydberg. Their assistance and support has been helpful throughout. The experimental assistance, intelligent discussions and overall friendship provided by Tonia Jiao, in particular, has been invaluable. My thanks also go to James Mahoney who, as an undergrad research assistant, was very helpful in preparing samples.

I consider myself very fortunate for having been in the Solid Mechanics group at Brown. The overall talent and approachability of the faculty is incredible and they have provided a great learning environment. I would like to thank all of the engineering

faculty and in particularly I would like to mention Prof. Guduru, Prof. Bower, Prof. Kumar and Prof. Sheldon. I would also like to thank the many members of the staff that have been instrumental to my work, including Chris Bull, Brian Corkum, Charlie Vickers, Mike Packer, Reese Webb, Mike Jibitsky, Barry Breisch, Tony McCormick, and Peggy Mercurio. I am appreciative of the many graduate students in engineering, most of whom have become my good friends, that I have worked with during my time at Brown.

I am ever grateful for the love and support of my family. They have always provided me with opportunities to excel and have instilled in me an insatiable curiosity – a desire to know more. Finally, I would like to thank my girlfriend, Beth. Her support and patience during my time here has been unwavering. She is tirelessly selfless and I can only hope that I will, one day, be as good of a person as she is.

I would like to acknowledge the support of MRSEC and Lawrence Livermore National labs.

To Gladys, Carl, Mary and Joe

Contents

List of Tables

List of Figures

Chapter 1

Introduction

Understanding the behavior of materials deformed at high rates and at elevated temperatures is important in a number of engineering applications, including metal forming, high-speed machining and the development of protective armors. Such understanding is of fundamental importance in determining the mechanisms of shear band formation and fracture that occur at high rates of deformation and that are of central importance in a wide range of impact-related applications. A goal of research in this area is the development of reliable constitutive models for predicting the inelastic response of materials in the regime of high strain rates and high temperatures.

Over the past five or six decades, several experiments have been developed to measure the dynamic response of materials over a range of temperatures. Most notably, the Kolsky (or split-Hopkinson) bar technique has been widely used to study the dynamic response of materials at high rates ($10^2 - 10^4$ s^{-1}). The technique utilizes a stress pulse to load a small sample in compression, tension or torsion. Seo et al. (2005) used a modified Kolsky bar technique that enabled them to measure the dynamic response of a titanium alloy up to temperatures of 1000^oC.

Taylor impact tests are another common experiment used to study the response of materials at high rates deformation. For Taylor impact experiments, a cylindrical sample impacts a rigid wall and the profile of the deformed cylinder is used to determine the material response. Taylor impact tests have been used to test materials at strain rates on the order of $10^4 - 10^5$ s^{-1} and at temperatures up to 1000^{o}C (Gust (1982)). However, since the deformation of the sample is not uniform, the results are not a direct measure of the intrinsic response of the sample material.

In the investigation reported here, plate impact experiments are used to determine the mechanical response of aluminum at elevated temperatures and high strain rates. With plate impact experiments, the impact of two flat, parallel plates generates plane waves than can be interpreted quite directly to improve understanding of the dynamic response of materials. In these experiments, a flyer plate impacts a target plate (or target assembly) generating stress waves which travel through the target assembly and are monitored at the rear surface. The wave propagation is one-dimensional until cylindrical waves, generated from the lateral boundaries of the plates, arrive.

For plate impact experiments where the flyer and target plates are parallel to each other but are inclined with respect to the direction of travel, the impact will generate compression and shear waves that can be used to study the mechanical behavior of materials (Abou-Sayed et al. (1976)). There are a variety of configurations for this oblique impact (or pressure-shear plate impact) experiment that have been used to study an assortment of materials under many different loading conditions. At the Brown University Plate Impact Facility over the past several decades, experiments have been performed using the pressure-shear plate impact configuration to study metals (Klopp et

al. (1985), Gilat and Clifton (1985), Duprey (1999), Zhou (1993)), ceramics (Sundaram (1998), Espinosa (1992)), lubricants (Ramesh and Clifton (1987)), powders (Sundaram (1994)), and polymers (Jiao et al. (2007)) at strain rates between $10^5 - 10^7$ s^{-1}. While most tests have been set up to measure material response at a nominally constant shear strain rate, change of rate tests have been conducted by Tong et al. (1992) to test strain-rate history effects. The pressure-shear plate impact experiment has also been used to study dynamic fracture (Prakash (1993)), shear band propagation (Zhang and Clifton (2003)), time-resolved dynamic friction (Prakash (1993)) and stress-induced phase transformations (Escobar and Clifton (1995)). Dynamic material responses have been tested at low temperatures down to -100°C (Ravichandran (1987)) and at elevated temperatures up to 691°C (Frutschy (1997)). The versatility of the pressure-shear plate impact experiment is due to the well-characterized one-dimensional plane wave loading conditions which simplify the interpretation of the experimental profiles. In the current investigation, the high-temperature, pressure-shear plate impact experiment was used with a target sandwich configuration in order to test the dynamic response of high purity, polycrystalline aluminum at ultra-high shear strain rates (10^6 s^{-1}) and at temperatures that approach melt.

1.1 Motivation

Several authors have shown that temperature and strain rate significantly affect the mechanical behavior of high purity aluminum (Trozera et al. (1957), Tanaka et al. (1970), Yoshida and Nagata (1966), Lindholm and Yeakley (1965), Hauser et al. (1961) Klopp (1987), Morrone and Duffy (1986)). Specifically, the flow stress was shown to

increase with increasing strain rate and decrease with increasing temperature. For high purity polycrystalline aluminum the flow stress increases slowly with the logarithm of strain rate at rates below 10^3 s^{-1}. The strain rate sensitivity increases at strain rates above 10^3 s^{-1} (see Figure 1.1). The flow stress decreases with increasing temperature over the previously tested range of strain rates from 10^{-5} s^{-1} to 10^3 s^{-1}. The current study extends the regime of strain rates and temperatures for which the shearing resistance of high purity aluminum has been measured to strain rates of 10^6 s^{-1} for temperatures approaching melt.

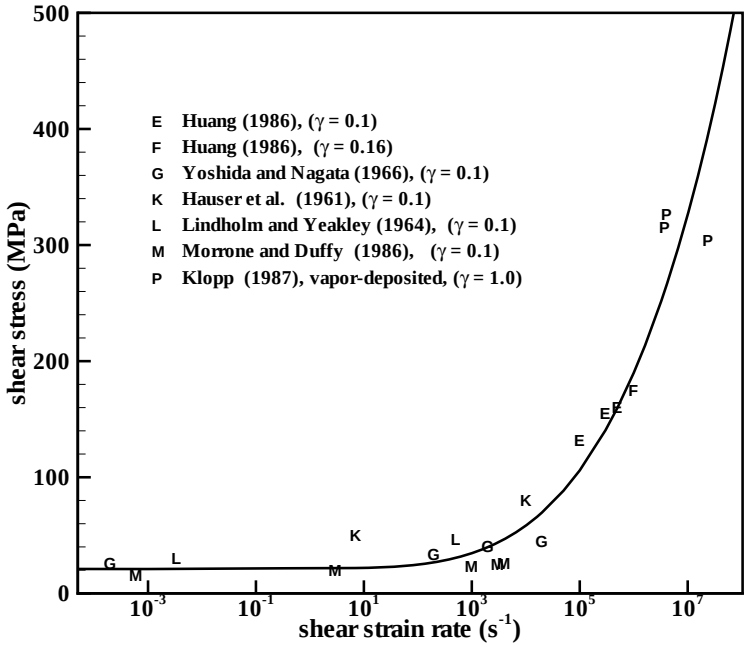

Figure 1.1: Strain rate sensitivity of high purity aluminum.

Frutschy and Clifton (1998a) modified the pressure-shear plate impact experiment in order to test OFHC copper at elevated temperatures. In that study, high-temperature, pressure-shear plate impact tests were conducted on OFHC copper at three elevated starting temperatures (500, 600, and 700°C) and two strain rates (10^5 and 10^6 s^{-1}) to

characterize the responses. The results of that work show that the shearing resistance decreases with increasing temperature and increases with increasing strain rate over the full range of temperatures and strain rates examined (Figure 1.2). However, the flow stress at the highest temperatures and highest strain rates was substantially greater than predicted by models based on rate-controlling processes involving the thermally activated motion of dislocations past obstacles. While conclusive evidence of a change in rate-controlling mechanism was not obtained, the response suggests that the influences of temperature and strain rate may be changing at the highest temperatures. The current study was undertaken to examine whether or not these trends observed by Frutschy and Clifton (1998a) persist at still higher fractions of the melting temperature. Larger fractions of the melting temperature are accessible in the current study due to the lower ambient melting temperature of aluminum, 660°C (933 K).

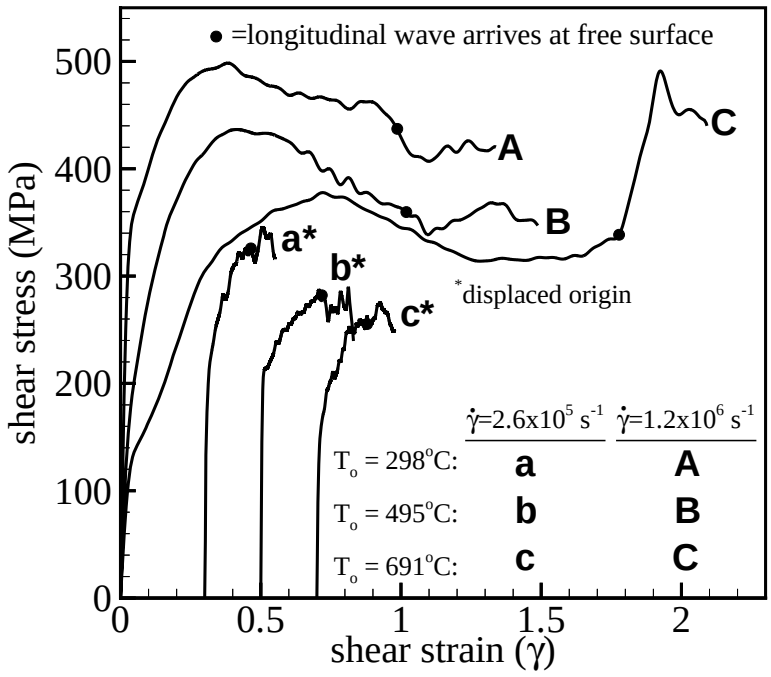

Figure 1.2: Dynamic response of OFHC copper. (Fig. 8 from Frutschy and Clifton (1998a))

1.2 Organization of thesis

Chapter 2 presents the wave theory and experimental procedures associated with a high-temperature, pressure-shear plate impact experiment. Included in this chapter are sections on the production of high-temperature gratings, the optical set up, the alignment technique and the approach used to calculate the tilt angle at impact. Chapter 3 provides a thermodynamic analysis of the high-temperature, pressure-shear plate impact experiment and gives a relation used to predict the change in sample temperature, assuming adiabatic conditions.

The results of five experiments conducted on high purity polycrystalline aluminum at strain rate on the order of 10^6 s^{-1} and at starting temperatures ranging from room temperature up to 591°C are presented in Chapter 4. High-temperature symmetric impact tests on tungsten carbide plates were conducted to validate their use as loading plates in the experiments on aluminum. The results of those tests are also presented in Chapter 4.

In Chapter 5, three constitutive models are used in the finite difference simulations of the high-temperature, pressure-shear plate impact experiment. Due to the short duration of the experiments (typically less than 2 μs), the common understanding is that there is too little time for significant heat diffusion and therefore adiabatic conditions are assumed. This assumption is addressed in Chapter 5.

Final thoughts on the results of the thesis are given in Chapter 6.

Chapter 2

Experimental Technique

To test material response at ultra-high, shear strain-rates (10^5 – 10^7 s^{-1}), a pressure-shear plate impact experiment utilizing a target sandwich configuration can be used (see Figure 2.1), where a thin (5-500 μm) sample is placed between two harder target plates that respond elastically (Li and Clifton (1981)). The flyer and the target plates are parallel to each other and they are both inclined – by the impact angle θ – to the direction of travel. For sufficiently small impact angles (typically less than 20°) there will be no slip at the impact surface and friction will generate shear waves. Therefore, for this configuration, the impact will generate compression and shear waves that travel forward into the target and rearward into the flyer. These waves travel through the target assembly before arriving at the rear surface of the rear target plate where the normal and transverse motion they induce is monitored via laser interferometry. Shear strains of 100-200% are commonly obtained using this high strain-rate, pressure-shear plate impact configuration. Klopp et al. (1985) imposed shear strains as large as 2400% on vapor deposited aluminum samples using this configuration.

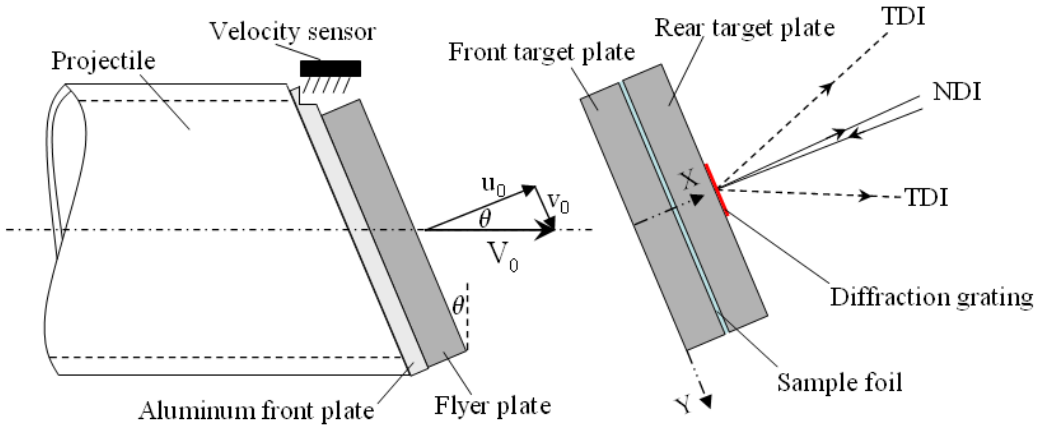

Figure 2.1: Pressure-shear plate impact schematic.

2.1 High strain-rate, pressure-shear plate impact theory

The time-distance (t-x) diagram for a high strain-rate, pressure-shear plate impact experiment is shown in Figure 2.2. The impact is taken to occur at x = 0 at time t = 0. The longitudinal wavefronts travel at the elastic longitudinal wave speed c_1 and are represented by solid lines. The shear wavefronts, represented by the dashed lines, travel at the elastic shear wave speed c_2, where $c_2 < c_1$. In the target, the longitudinal wave travels through the front plate and arrives at the sample before the shear wave. Inside the sample (which has a lower acoustic impedance than the surrounding target plates), the longitudinal wave reverberates through the thickness, ringing the stress up to a uniform state of compressive stress. Only a small amount of plastic strain is associated with this loading (<7.5% according to simulations on aluminum). Upon reaching the rear surface, the longitudinal wave reflects back as a tensile unloading wave. The sample is already under pressure when the shear wave arrives, allowing friction between the sample and the loading plates to transmit the shear stress through the sample.

At impact, cylindrical unloading waves (or boundary waves) are also generated at the edges of the plates and at any holes in the plates. When these waves reach the point being monitored interferometrically – at the rear surface of the target near the center – the motion there is no longer solely induced by readily interpretable plane waves and the displacement record is not used beyond this point. The thicknesses and acoustic impedances of the loading plates vary for different tests and affect the loading history. These differences will be addressed individually in Chapter 4. For the specific case shown in Figure 2.2, the unloading longitudinal wave reflected off the rear surface of the target returns to the sample at the same time as the unloading longitudinal wave that has reflected off the rear surface of the flyer. At this time, the sample experiences a tensile stress, which separates the sample from the loading plates and discontinues the transmission of the shear stress. The transverse motion monitored at the rear surface of the target during the "shear window" (Figure 2.2) can be used to determine the shear response of the sample while it was subjected to shear loading. Tests are designed to maximize the time of the shear window before the boundary waves arrive.

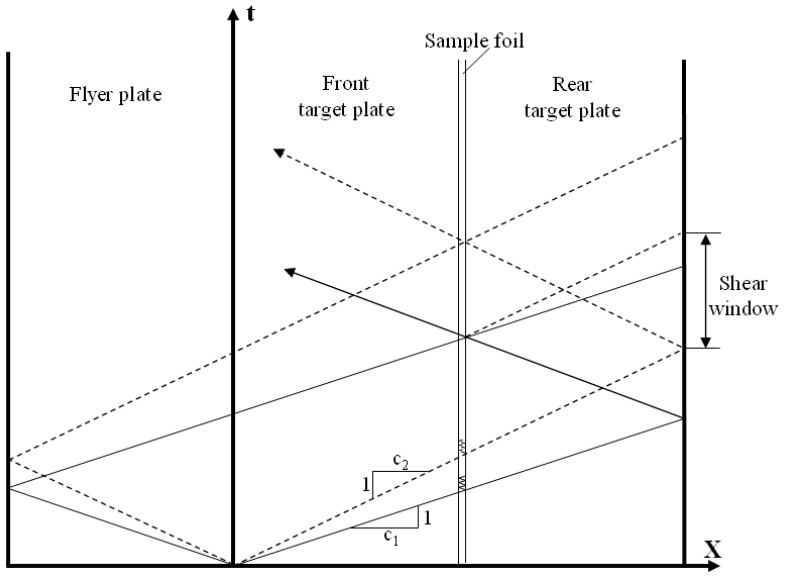

Figure 2.2: Time-distance diagram for a general pressure-shear plate impact experiment.

In the case where the flyer plate is approximately double the thickness of the rear target plate (as shown in Figure 2.3), the reflected unloading wave from the flyer arrives at the sample later and does not affect the loading history. For this pressure-release type experiment, the reflected unloading wave from the rear surface of the target reduces the compressive stress at the sample to zero. If the sample is sufficiently bonded to the bounding target plates, then the sample will continue to be deformed in shear (at nominally the same strain rate) while at nominally zero pressure. The initial shear window is the time, monitored at the rear surface, corresponding to the time when the sample was deformed in shear while under pressure. The second shear window is the time that provides the information for the sample deforming in shear while at nominally zero pressure. When the reflected unloading wave from the rear surface of the target reaches the impact surface, slipping will occur and the shear loading will cease. When the end of that shear pulse reaches the target rear surface, at the end of the second shear window, the test is over.

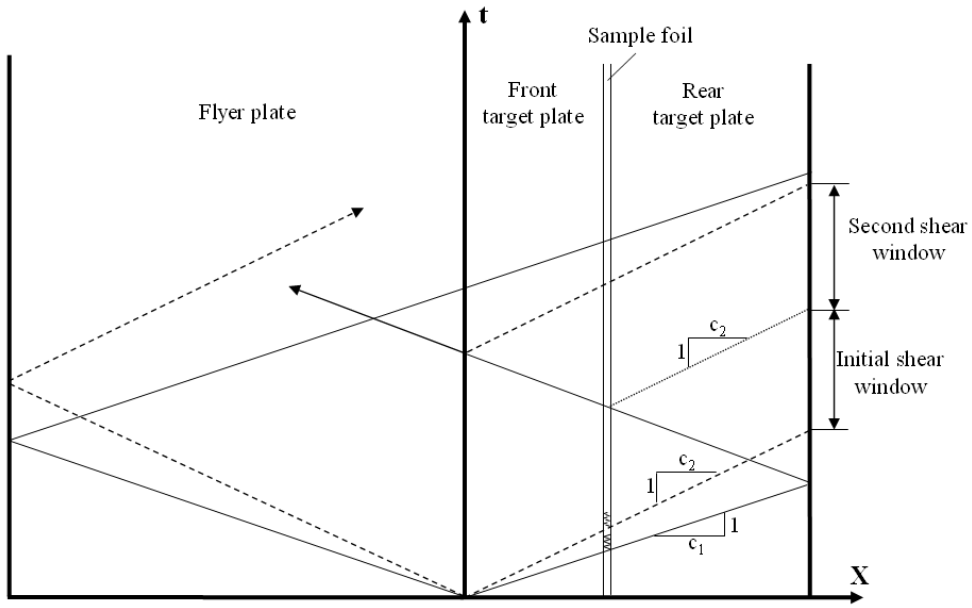

Figure 2.3: Time-distance diagram for a pressure-shear plate impact experiment with a pressure-release configuration.

If the flyer and target loading plates respond elastically, one-dimensional elastic wave theory can be used to calculate the stresses and velocities at the back surface of the sample from the velocities at the rear surface of the target assembly. Wave propagation in a linearly elastic half space is governed by the following partial differential equations

$$\frac{\partial^2 U}{\partial t^2} = c_1^2 \frac{\partial^2 U}{\partial X^2} \tag{2.1}$$

$$\frac{\partial^2 V}{\partial t^2} = c_2^2 \frac{\partial^2 V}{\partial X^2}. \tag{2.2}$$

Where U is the displacement in the direction perpendicular to the impact surface along the Lagrangian spatial coordinate X (Figure 2.1), V is the displacement perpendicular to U along the shearing direction (Lagrangian spatial coordinate Y), c_1 is the longitudinal acoustic wavespeed, c_2 is the shear acoustic wavespeed, and t is time. The solutions to Equations (2.1) and (2.2) are, respectively,

$$\sigma \pm (\rho c_1) u = \text{constant along the characteristics } \frac{dX}{dt} = \mp c_1 \tag{2.3}$$

and

$$\tau \pm (\rho c_2) v = \text{constant along the characteristics } \frac{dX}{dt} = \mp c_2. \tag{2.4}$$

Where $u = \frac{\partial U}{\partial t}$ is the normal particle velocity, σ is the normal stress in the direction of U, $v = \frac{\partial V}{\partial t}$ is the transverse particle velocity and τ is the shear stress. The mass density in the reference configuration is represented by ρ and the longitudinal and shear acoustic impedances are ρc_1 and ρc_2 respectively.

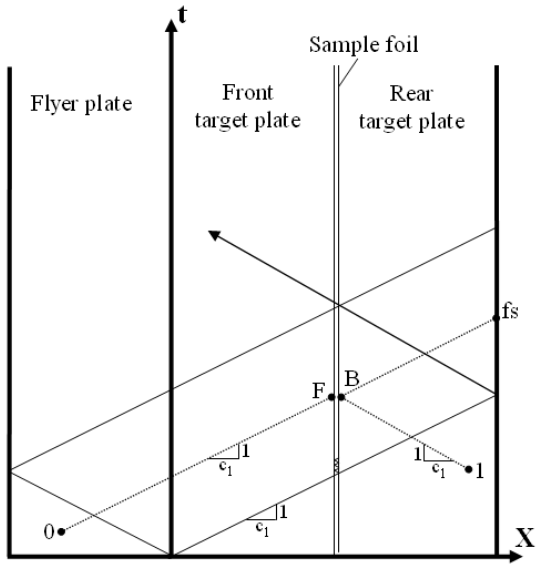

Figure 2.4a

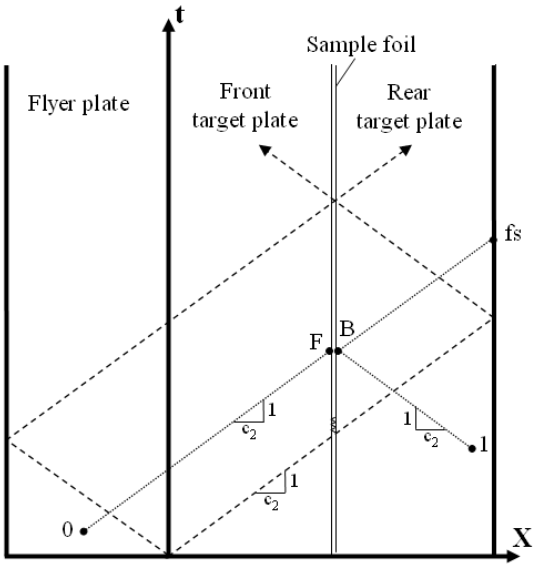

Figure 2.4b

Time-distance diagrams used for characteristic analysis of the normal loading (a) and the shear loading (b).

A characteristic analysis can be used for the longitudinal and shear loading separately (as shown in Figure 2.4). For this initial overview, the longitudinal and shear acoustic impedances, $(\rho c_1)_L$ and $(\rho c_2)_L$ respectively, are assumed to be the same for all loading plates. The subscript '*L*' denotes values for all loading plates.

For the normal loading analysis (Figure 2.4a), along the line $\frac{dX}{dt} = c_1$, from point 0 to point F, the quantity $[\sigma - (\rho c_1)_L u]$ is a constant. And along the line $\frac{dX}{dt} = -c_1$, from point B to point 1, the quantity $[\sigma + (\rho c_1)_L u]$ is a constant. Point F and point B are the states at the front face and the back face of the sample, respectively. Therefore:

$$\sigma_F - (\rho c_1)_L u_F = \sigma_0 - (\rho c_1)_L u_0 \tag{2.5}$$

and

$$\sigma_1 + (\rho c_1)_L u_1 = \sigma_B + (\rho c_1)_L u_B \tag{2.6}$$

The flyer is initially unstressed and travelling at a velocity V_0 (point 0). The velocity can be resolved into the normal flyer velocity ($u_0 = V_0 \cos\theta$ along the *X*-axis) and the transverse flyer velocity ($v_0 = V_0 \sin\theta$ along the *Y*-axis) as shown in Figure 2.1. The target assembly is initially unstressed and at rest (point 1). These initial conditions, written as

$$\sigma_0 = \sigma_1 = 0, \tag{2.7a}$$

$$u_1 = 0, \tag{2.7b}$$

can be used to reduce Equations (2.5) and (2.6) to

$$\sigma_F - (\rho c_1)_L u_F = -(\rho c_1)_L u_0, \tag{2.8}$$

and

$$\sigma_B + (\rho c_1)_L u_B = 0. \tag{2.9}$$

These equations characterize the normal stresses and normal particle velocities at the front and back of the sample, as shown graphically in stress-velocity space in Figure 2.5. The solid line with a slope equal to positive $(\rho c_1)_L$ represents the allowable states of normal stress and particle velocity at the interface between the sample and the rear target plate, as characterized by equation (2.9). Equation (2.8), represented by the solid line with a slope of negative $(\rho c_1)_L$, corresponds to the possible states of normal stress and particle velocity at the front face of the sample. The state of normal stress and particle velocity in the sample, which has a lower acoustic impedance than the loading plates, rings up as shown by the dashed line in Figure 2.5 with a slope of $\pm(\rho c_1)_S$. After the ring up is complete, the normal stress and the particle velocity are continuous through the

thickness of the sample, i.e. $\sigma_F = \sigma_B = \sigma_S$ and $u_F = u_B = u_S$, where the subscript '*S*' represents a uniform state in the sample. Therefore, from Equations (2.8) and (2.9):

$$\sigma_S = -\frac{(\rho c_1)_L u_0}{2} \tag{2.10}$$

and

$$u_S = \frac{u_0}{2}. \tag{2.11}$$

Following a similar characteristic analysis, the normal free surface velocity can be related to the normal stress and particle velocity in the sample:

$$\sigma_S - (\rho c_1)_L u_S = -(\rho c_1)_L u_{fs} \tag{2.12}$$

And from Equation (2.9)

$$\sigma_S + (\rho c_1)_L u_S = 0. \tag{2.13}$$

Combining Equation (2.12) and Equation (2.13) one gets

$$\sigma_S = -\frac{(\rho c_1)_L u_{fs}}{2} \tag{2.14}$$

and

$$2u_S = u_{fs} = u_0. \tag{2.15}$$

Again, these specific relations hold true only for elastic flyer and bounding plates which all have the same acoustic impedances.

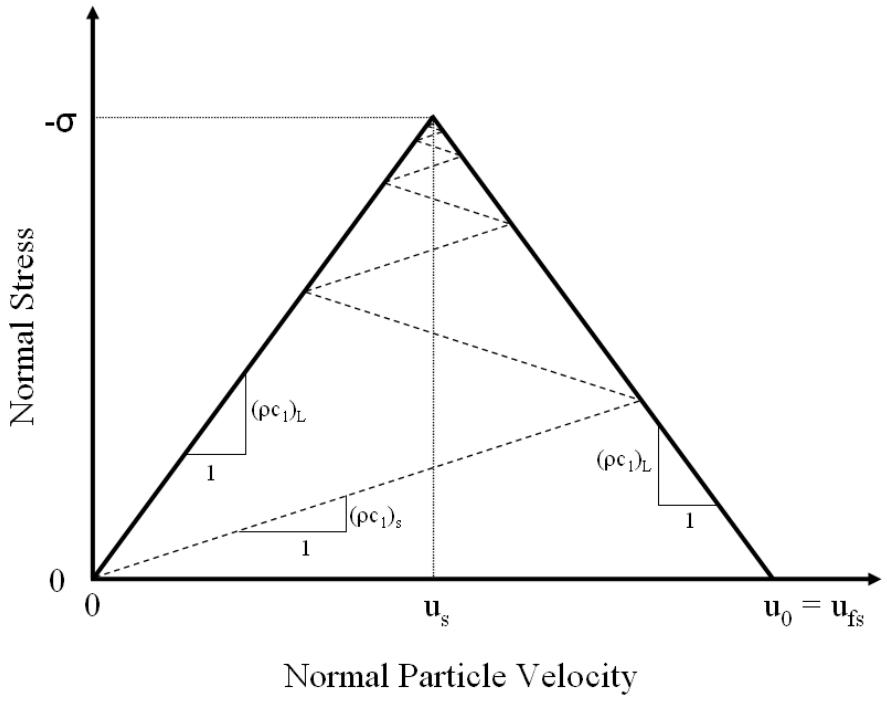

Figure 2.5: Compressive state in sample.

A parallel characteristic analysis can be used to find the shear stress and shear strain rate in the sample. The states of shear stress and transverse particle velocity at the front and back faces of the sample satisfy the following characteristic relations (Figure 2.6):

$$\tau_F - (\rho c_2)_L v_F = -(\rho c_2)_L v_0 \tag{2.16}$$

and

$$\tau_B + (\rho c_2)_L v_B = 0 \tag{2.17}$$

If the sample response is elastic, then the shear stress will ring up to the apex of the triangle and a shear stress of $\tau = 0.5(\rho c_2)_L v_0$. However, if the sample does not respond elastically up to such a shear stress, then the sample will respond plastically and the transverse velocity will not be uniform across the sample. Dividing the velocity

difference of the front and back surfaces of the sample by the thickness of the sample yields the nominal strain rate:

$$\dot{\gamma} = \frac{v_F - v_B}{h}. \tag{2.18}$$

After the shear stress has rung up in the sample, the stress is uniform through the thickness of the sample and therefore $\tau_F = \tau_B = \tau_S$. Using Equation (2.17) and the characteristic relation

$$\tau_S - (\rho c_2)_L v_B = -(\rho c_2)_L v_{fs}, \tag{2.19}$$

the shear stress in the sample can be given as a function of transverse free surface velocity:

$$\tau_S = -\frac{(\rho c_2)_L v_{fs}}{2}. \tag{2.20}$$

With further algebraic manipulation one finds

$$v_B = \frac{v_{fs}}{2} \tag{2.21}$$

and

$$v_F = v_0 - v_B \tag{2.22}$$

Therefore, using Equations (2.18), (2.21) and (2.22), the strain rate can be calculated from the free surface velocity (v_{fs}) and the transverse component of the projectile velocity (v_0):

$$\dot{\gamma} = \frac{v_0 - v_{fs}}{h}. \tag{2.23}$$

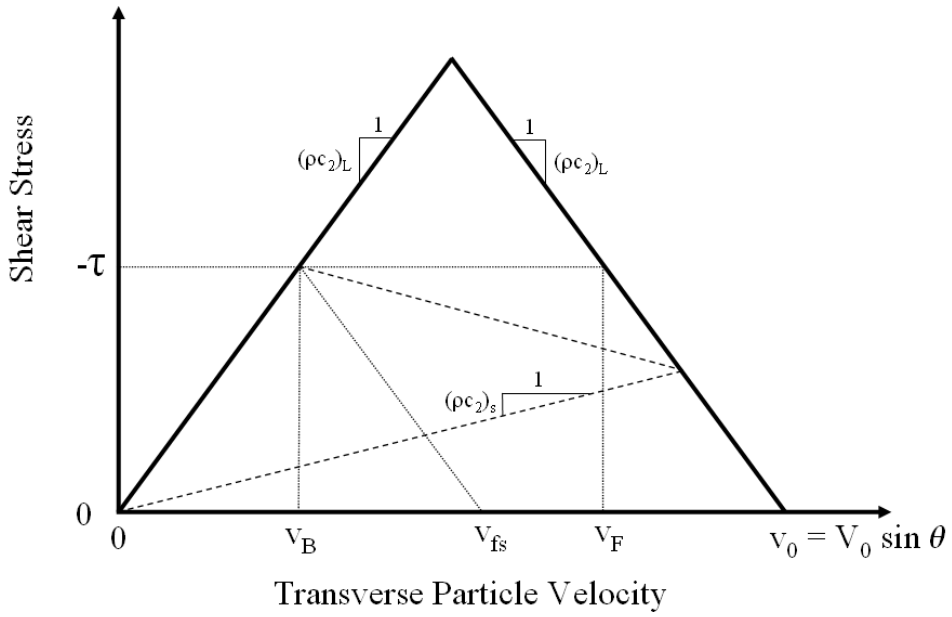

Figure 2.6: Shear state in sample.

This strain rate value is valid only after the sample has reached a uniform state of stress. The shear strain can be calculated by integrating the shear strain rate over time.

For the cases where the impedances of the flyer plate differ from those of the target plates, the relations between the stresses and free surface velocities still hold (from Equations (2.14) and (2.20)):

$$\sigma_S = -\frac{(\rho c_1)_T u_{fs}}{2} \tag{2.24}$$

$$\tau_S = -\frac{(\rho c_2)_T v_{fs}}{2}. \tag{2.25}$$

Here, $(\rho c_1)_T$ and $(\rho c_2)_T$ are the longitudinal and shear acoustic impedances of the target respectively. The shear strain rate, however, becomes

$$\dot{\gamma} = \frac{\dfrac{2(\rho c_2)_{fl}}{(\rho c_2)_{fl} + (\rho c_2)_T} v_0 - v_{fs}}{h} \tag{2.26}$$

where $(\rho c_2)_{fl}$ is the shear impedance of the flyer plate. It can be observed that if the impedance of the flyer matches that of the target, Equation (2.26) reduces to Equation (2.23).

2.2 High-temperature, pressure-shear plate impact experiment

To study pure aluminum at high strain-rates and high temperatures, pressure-shear plate impact experiments were conducted with modifications introduced by Frutschy (1997) that allowed tests to be conducted at elevated temperatures. To heat the target sandwich, the high-temperature, pressure-shear plate impact experiment uses a 20 *kW* induction heater – which is a high-voltage (~10 kV), high-current (~2 *A*) radio frequency (~250 *kHz*) sine-wave generator. High-temperature tests have been conducted on aluminum up to starting temperatures of 591^{o}C. The details of how these tests were conducted are presented in the following sections.

2.2.1 Plate impact facility: General layout and equipment

The target assembly is mounted in the target chamber at the muzzle end of the barrel. A projectile, with the flyer plate attached to the front, is accelerated down a 2.5 meter long, 2.5 inch diameter barrel by compressed nitrogen gas from a single stage gas gun (Figure 2.7). A key on the projectile fits snugly in a keyway in the barrel and prevents the projectile from rotating as it travels down the barrel.

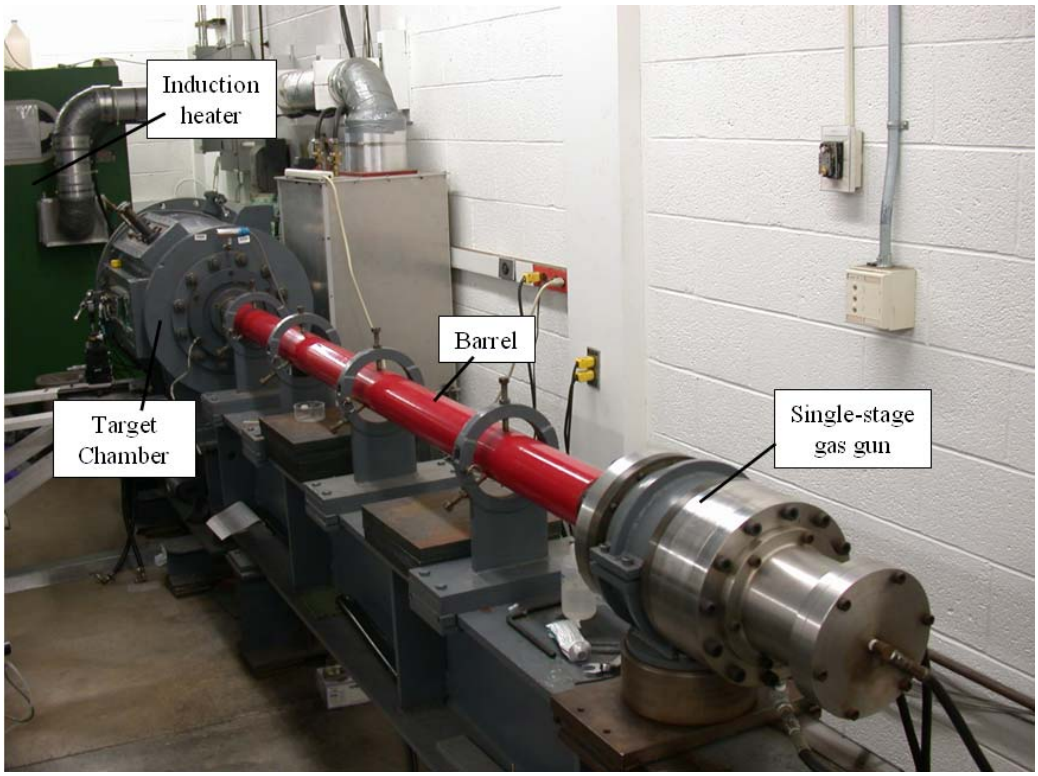

Figure 2.7: Plate impact facility at Brown University.

The velocity of the projectile is measured by means of a velocity sensor (as shown in Figure 2.1) as it emerges from the muzzle end of the barrel. This sensor has five electrically biased pins (0.010" diameter Constantan wires) that are spaced at measured intervals. An aluminum plate, mounted near the front of the projectile and grounded by contact with a series of ground wires, contacts these five pins and shorts them out at times recorded on an oscilloscope (LeCroy model 9314L). From these recorded times, corresponding to the distance traveled between velocity pins, the velocity of the projectile just prior to impact is calculated.

A Verdi solid-state laser is used to measure interferometrically the motion at the rear surface of the target. The laser beam is directed through a window in the side of the target chamber to a central spot on the rear surface of the target where the beam is

reflected and diffracted by a grating that has been manufactured on the surface (see Section 2.2.4). The reflected and diffracted beams are collected and combined to produce interferometers (see Section 2.2.5). The intensity variations of those combined interfering beams are monitored using photodiodes and recorded on two separate oscilloscopes for redundancy. The normal and transverse velocity history of the rear surface of the target is obtained from these records.

A catcher tank, which is filled with corrugated lead and bolted in the rear of the target chamber, safely decelerates the projectile and collects debris from the impact.

2.2.2 Preparation of target assembly and projectile

The flyer and target plates (or loading plates) were all made of tungsten carbide with various compositions. The material parameters of the loading plates for each test or "shot" are listed in Table 4.4. It should be noted that acoustic impedances of these plates are temperature dependent and the values have been adjusted accordingly in Table 4.4 (for more details see Section 4.1).

Electron discharge machining (EDM) is used to cut four bolt holes in the front target plate and six holes – four bolt holes and two holes for thermocouples – in the rear target plate (see Figure 2.8). The holes on the impact face of the front target plate are countersunk by grinding with a 3.3 *mm* diameter diamond burr drill bit. All of the tungsten carbide plates are then lapped to a flatness of better than 0.6 μm over the 50 *mm* plate diameter using a boron carbide lapping slurry on a Lapmaster lapping wheel. The rear target plate is then polished using a 3 μm diamond paste. When the rear surface has been polished to a mirror finish, a laser diffraction grating is manufactured on that

surface using a photolithography process (see Section 2.2.4). The resulting grating has a frequency of either 602 lines per millimeter or 625 lines per millimeter (depending on the lithography process). Such a grating allows the normal and transverse displacement to be monitored using laser interferometry (See Section 2.2.5).

The front target plate is bolted to the rear plate, with the thin aluminum sample sandwiched between, using four countersunk flat-head screws. Care is taken to ensure that the screw heads sit below the impact surface of the front plate.

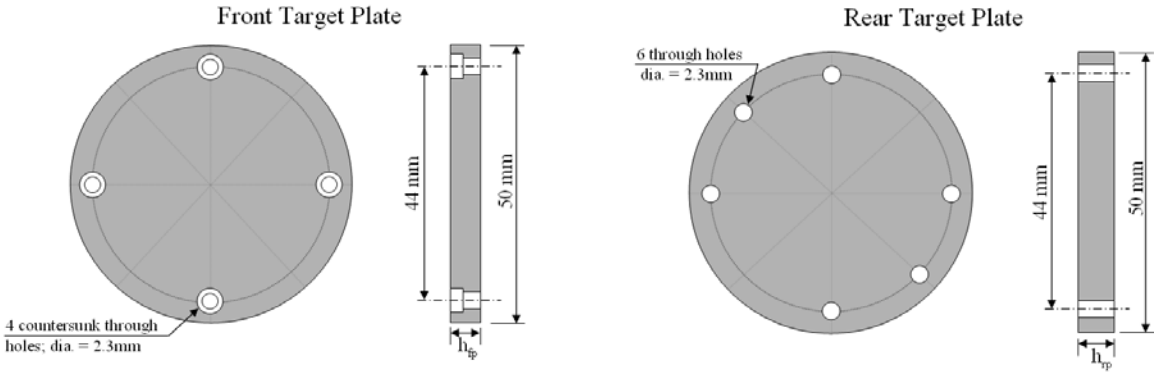

Figure 2.8: Details of target plates.

Type K thermocouples were used to measure the temperature near the edges of the target sandwich. The thermocouples are manufactured from 0.020" diameter alumel and chromel (type K) wires using a TIG welding technique that creates a junction that is between 0.050" and 0.090" in diameter (see Figure 2.9). A thermocouple is inserted into

Figure 2.9: Thermocouple junction.

each of the two thermocouple holes in the rear target plate and is secured in place using OMEGA brand CC high temperature cement. If the thermocouples (and therefore the thermocouple holes) are placed closer to the center of the target, unwanted cylindrical waves would emanate from that location and shorten the length of the interpretable experimental record. The temperature at the center is calculated from the temperatures at the edges using a full body finite element analysis (see Section 3.2).

The target sandwich is fastened into a lava stone sample holder and the thermocouples are fed through Mullite rods to insulate them from the heat and to protect them from electrical shorts. Four hollow, ceramic, mounting rods are glued into holes in the sample holder using Sauereisen brand Aluseal adhesive cement No. 2.

The projectile (or flyer assembly) consists of the flyer plate, an aluminum front plate, a hollow fiberglass tube and an end cap. The fiberglass tube has a 2.5" outer diameter and the front end is cut at the angle θ. An aluminum plate is glued with epoxy to the front end of the projectile tube and the flyer plate is then glued to the aluminum front plate. The end cap has an O-ring that fits snugly in the barrel and a teflon key that fits snugly in the keyway of the barrel. After the end cap has been glued to back end of the projectile, the entire projectile will not rotate in the barrel. To simplify the optics in the experiment, the shear direction is set to be horizontal in the laboratory axis. To accomplish this, the end cap is glued with epoxy to the back of the projectile, and placed in the barrel. Before the epoxy cures, a horizontal laser beam is brought in and reflected back by a mirror that has been attached to the flyer plate. The front part of the projectile is then rotated, while the end cap stays fixed by the key in the barrel keyway, until the

laser beam returns horizontally back on itself. The epoxy is then allowed to cure and the projectile remains in a fixed orientation where the shearing direction will be horizontal in the laboratory axis.

2.2.3 Induction heating equipment

The high-temperature target holder, used for elevated temperature shots, allows the target to be heated by induction while the holder itself and the surrounding equipment in the target chamber remain cool. There is an induction heating coil, consisting of two turns of ¼ inch copper tubing that feeds through the center of the target holder. The target sits near the middle of the induction coil, which is approximately 3 inches in diameter, and the target is heated by the magnetic field that the coil produces (Figure 2.10 and 2.11).

The target and induction heating coil are surrounded on four sides by a water-cooled copper heat shield that is permanently attached to the target holder. A disposable rear heat shield made of 0.005" thick copper foil is crimped onto the back of the water-cooled heat shield just prior to the test while taking care not to block any of the laser beams used in the optical setup. The heat shield confines the thermal radiation from the target and the magnetic field of the induction heating coil to the target area, leaving the outside frame of the target holder and the optical equipment inside the chamber cool.

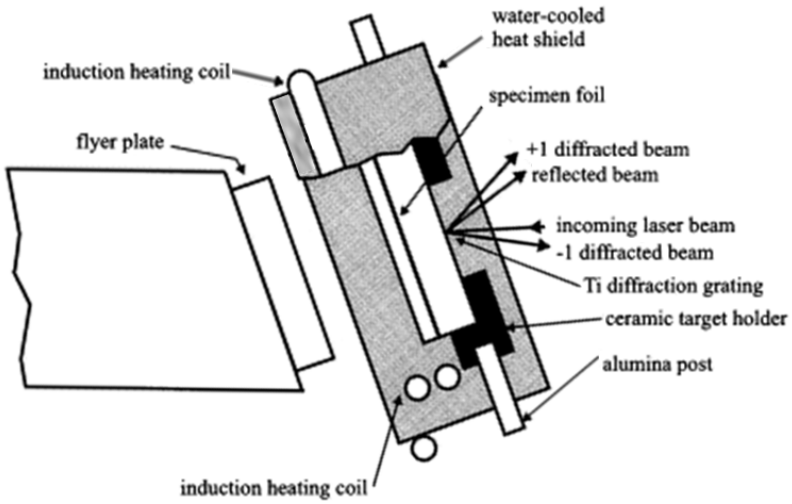

Figure 2.10: Schematic of high-temperature holder.

Heating induced by the magnetic field of the coil is proportional to the current in the coil. To boost the current in the induction heating coil, and reduce the power loss in the transmission line, a 6 to 1 step down transformer is used just outside the chamber. More details about the induction heater can be found in Frutschy (1997).

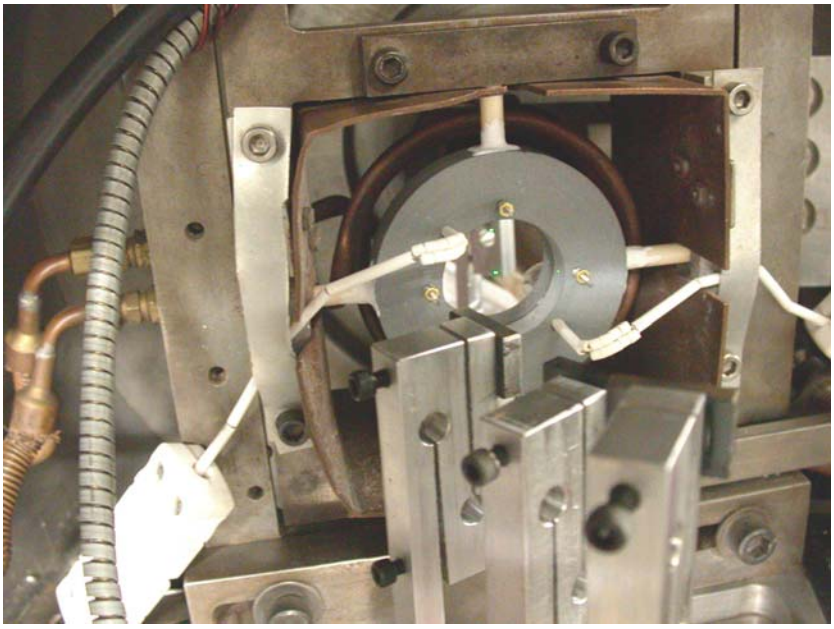

Figure 2.11: High-temperature target holder and target set up.

During the set up of the shot, the induction coil is centered around the projectile, so that the projectile will not damage the coil after impact. Also, the projectile is made long enough – 28 inches long – so that, after it has come to rest in the catcher, part of the projectile remains in the barrel. This ensures that the projectile proceeds straight through the center of the coil and does not get bounced around and destroy the coil during deceleration.

The thermocouples are connected to type K thermocouple monitors so that the temperature at the edges of the sample can be read outside the chamber. The induction heater can be controlled manually or automatically with the use of a Watlow temperature controller. The Watlow controller is set up to read the temperature of one of the thermocouples and control the induction heating unit in order to obtain the desired temperature at the target.

2.2.4 High-temperature gratings

Two different photolithography processes were used to manufacture high-temperature-compatible gratings on the rear surface of the target plates. The first process used electron-beam (e-beam) lithography and the second used a mask aligner technique. Both processes produced a grating of 100 *nm* tall titanium strips on the mirror-polished, rear surface of the rear target plate.

In the e-beam lithography process, which is similar to the process outlined by Frutschy (1997), polymethylmethacrylate (PMMA) is spun onto the rear surface of the target plate at 4500 RPM for 30 seconds. This produces a uniform PMMA layer that is

approximately 300 *nm* thick. The PMMA is then placed in an oven at 170°C for 30 minutes for a soft bake. Next, the electron-beam of a scanning electron microscope (SEM) is used to write a grating pattern into the PMMA. The SEM is programmed to write straight lines with a periodicity of 1.66 μm (or at a frequency of 602 lines per millimeter). The PMMA is developed in a one to three part mixture of methyl isobutyl ketone to isopropyl alcohol (MIBK/IPA), which clears away the PMMA that was exposed to the electron-beam. Reactive ion etching (RIE) is used with a standard oxygen-clean to clear away any debris left on the tungsten carbide surface in the sections that have been removed. With the remaining PMMA acting as a mask, 100 *nm* of titanium is evaporated on the surface and the titanium bonds to the tungsten carbide where the PMMA has been developed away. The PMMA is lifted off in an acetone bath, leaving titanium grating strips on the rear surface of the target with a frequency of 602 lines per millimeter.

The maximum grating area that could be produced with this process was limited by the field of view of the SEM. A 1 *mm* by 1 *mm* area was the largest grating area obtained with this method. In order to make the high-temperature test more reliable, a process that could produce a larger grating area was sought.

A process using a mask aligner was devised that produces a 15 *mm* by 15 *mm* grating area. This process uses an image reversal photoresist called AZ 5214 E IR. The photoresist is spun on the rear surface of the target at 4000 RPM for 40 seconds to produce a uniform layer that is approximately 1.4 microns thick. The photoresist is then baked at 115°C for 50 seconds on a hot plate. After the specimen has cooled it is placed in the mask aligner so that the photoresist is in tight contact with a grating mask. The

mask has a 15 *mm* by 15 *mm* grating area where strips of chrome, 0.08 μm wide, on a quartz substrate alternate with 0.08 μm of transparent space. In other words, the mask is a grating of 625 lines per millimeter of chrome on a transparent quartz substrate. The masked photoresist is exposed to a dose of 15 mJ/cm^3 of infrared light for 3 seconds. The next step is a reversal bake, where the photoresist is baked at 120°C for 2 minutes on a hotplate. The photoresist areas that have been exposed will crosslink during the reversal bake. The specimen is then placed back in the mask aligner without the mask and all of the photoresist is exposed for 40 seconds. The photoresist is then developed in AZ 327 MIF developer. All of the photoresist, except for the areas exposed during the initial mask exposure (which were subsequently cross-linked during the reversal bake), are developed away. An atomic force microscope (AFM) was used to measure the depth of the groove area see if the tungsten carbide surface is exposed. RIE is again used to oxygen-clean the bottom of the grooves all the way down to the tungsten carbide surface prior to titanium evaporation. As in the e-beam lithography process, 100 *nm* of titanium is deposited on the surface and then an acetone bath is used to lift-off the photoresist leaving the titanium grating on the tungsten carbide surface (Figure 2.12).

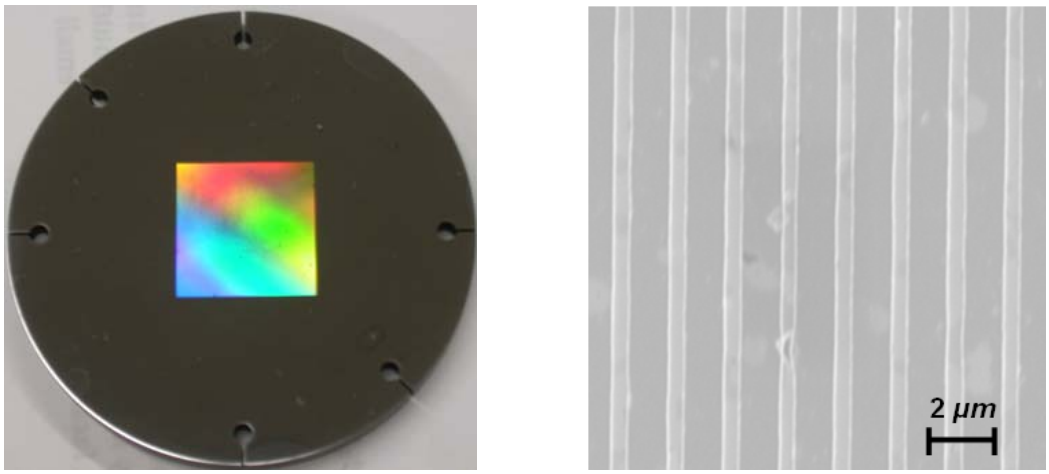

Figure 2.12: Grating on the rear surface of the target (left). SEM mircograph of titanium grating (right).

2.2.5 Optical setup

2.2.5a Combined NDI/TDI

The normal and transverse displacements of a central point on the rear surface of the target are monitored using a normal displacement interferometer (NDI) and a transverse displacement interferometer (TDI), respectively. The optical setup for a combined NDI / TDI is shown in Figure 2.13. A Verdi solid-state laser is used to supply a collimated, single-mode laser beam with a wavelength of 532 *nm*. The incident beam (represented by "I" in Figure 2.13) is directed to the first beam splitter (BS_1) which splits the beam into two beams ("I_1" and "I_2"). One of those beams ("I_1") continues on through a lens (f = 500 *mm*) and is focused to a spot on the grating at the center of the rear surface of the target. Diffracted beams emanate back from the grating at that spot. The zeroth order diffracted beam, or reflected beam ("R" in the Figure 2.13), is used to form the NDI. The first order diffracted beams ("+1D" and "-1D") are used in forming the TDI.

For the NDI (or Michelson-type interferometer), the reflected beam is combined with a beam ("I_2") that is reflected off stationary mirrors. These beams are oriented such that they are collinear after they are combined at the beam splitter (BS_2). The interference of these beams produces a maxima and minima of intensity when they are in and out of phase. A rear surface normal displacement equal to half the wavelength of the laser ($\lambda/2$ = 266 *nm*) produces a 2π phase variation (or one fringe) in the interference record. Two photodiodes (NDI_1 and NDI_2) detect the intensity variation and send a corresponding electrical signal to an oscilloscope where that signal is monitored as a function of time. The intensity profiles recorded by the two diodes should be exactly 180 degrees out of phase with each other. The intensity variation as a function of time can be

converted to a normal displacement versus time record. The derivative of this record yields the normal velocity versus time profile for the rear surface of the target. A raw NDI trace signal is shown for shot SG0802 in Figures 2.14.

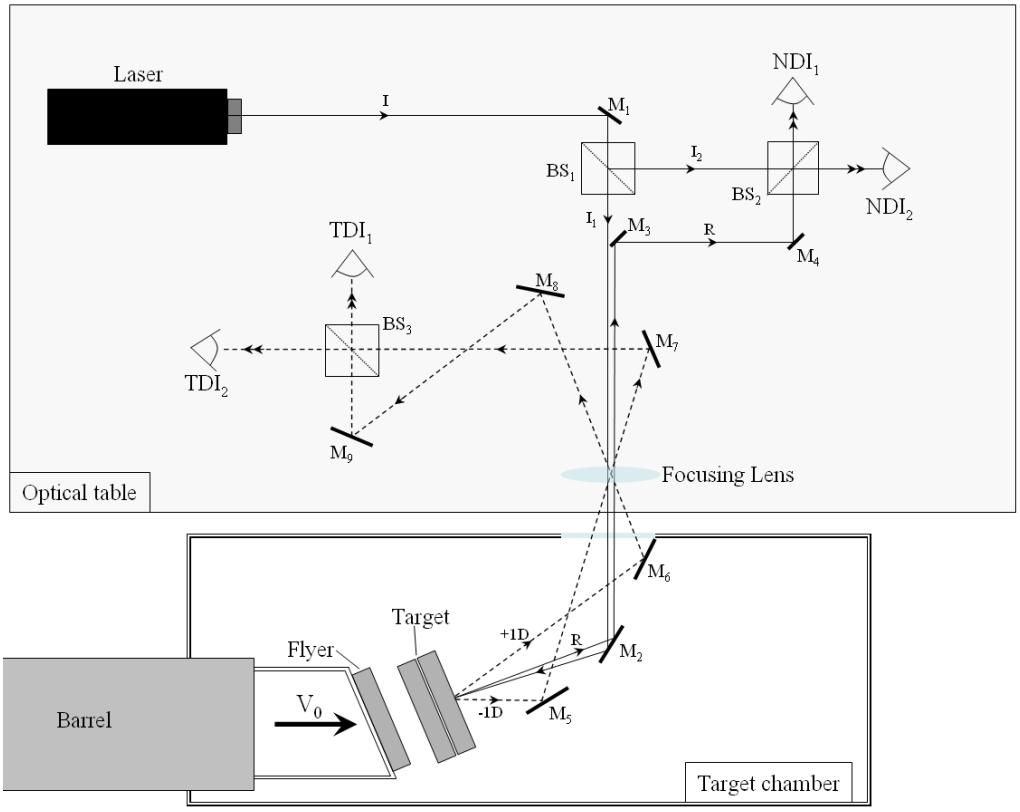

Figure 2.13: Combined NDI/TDI optical set-up.

The TDI is formed by combining the two first-order diffracted beams (Kim et al. (1977)). The TDI mirrors in the chamber ("M_5" and "M_6") are positioned and oriented such that the diffracted beams travel the focal distance (f = 500 *mm*) back to the focusing lens and pass through the center of the lens. This ensures that the resulting beams exiting the lens will be collimated. The intensity variation of the combined first order diffracted beams is recorded as a function of time via another pair of photodiodes (TDI_1 and TDI_2). Here, a phase variation equal to 2π corresponds to a rear surface transverse displacement that is equal to half the pitch of the grating (d/2). The pitch of the grating is the inverse of the grating frequency (d = 1/freq.). The intensity variation as a function of time can be

converted to a time profile of the transverse displacement. The derivative of this record yields the transverse velocity versus time profile for the rear surface of the target. The raw TDI trace signal for shot SG0802 is shown in Figure 2.15. When the longitudinal wave arrives at the rear surface, a small amount of transverse motion is observed due to tilt at impact. This transverse motion induced by the longitudinal wave can be observed as the partial fringe in the TDI trace produced between the arrival times of the longitudinal and shear waves at the rear surface.

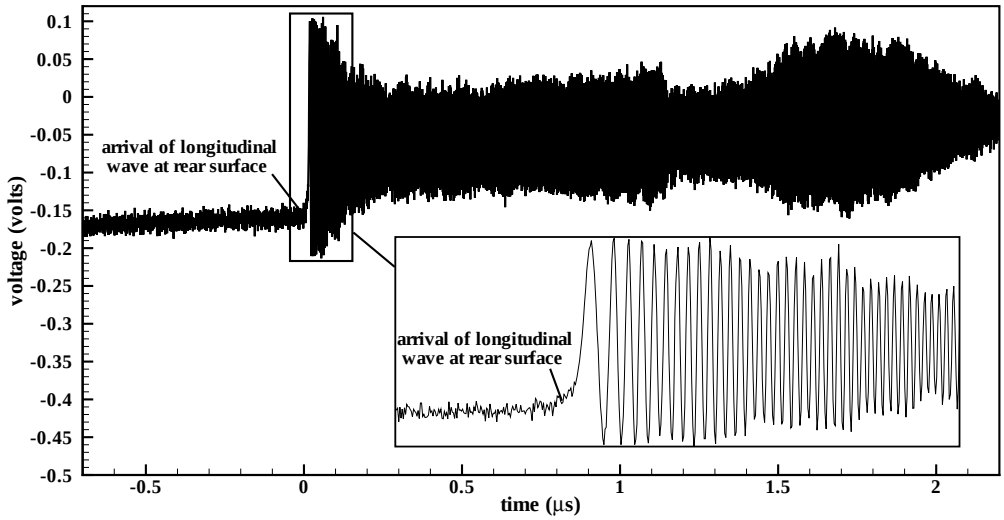

Figure 2.14: NDI trace signal for shot SG0802.

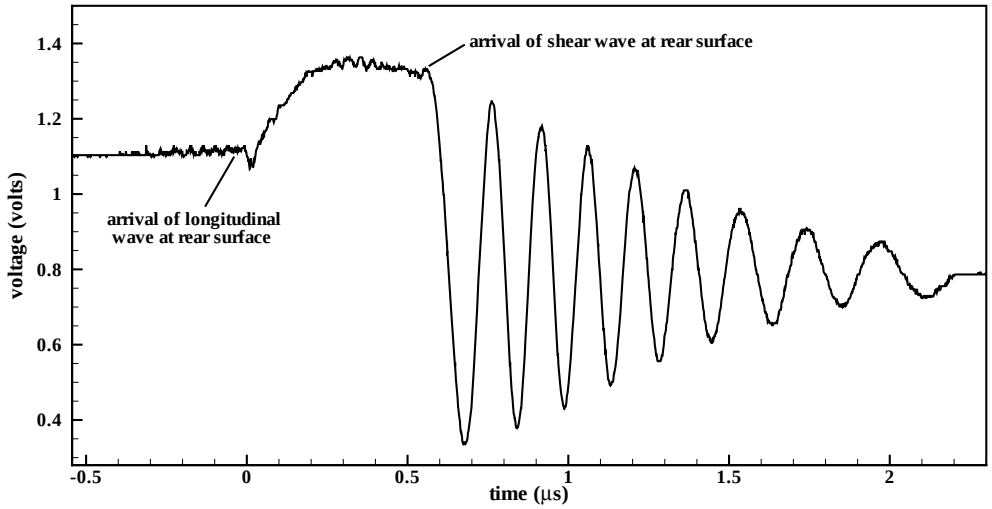

Figure 2.15: TDI trace signal for shot SG0802.

2.2.5b NDI$_A$

For elevated temperature shots, a second NDI (or alignment NDI) is used as well. This interferometer will be referred to as NDI$_A$. The central NDI used in the combined NDI/TDI will be referred to as NDI$_C$ from now on. The spot monitored by the NDI$_A$ is directly above (on the laboratory vertical axis) the spot monitored by the NDI$_C$. The optical setup with the NDI$_A$ is shown in Figure 2.16. The primary function of this interferometer is to record the arrival of the longitudinal wave at this location on the rear surface so it can be compared with the arrival time at the NDI$_C$. This information is used in the measurement of tilt at impact (detailed in Section 2.2.7).

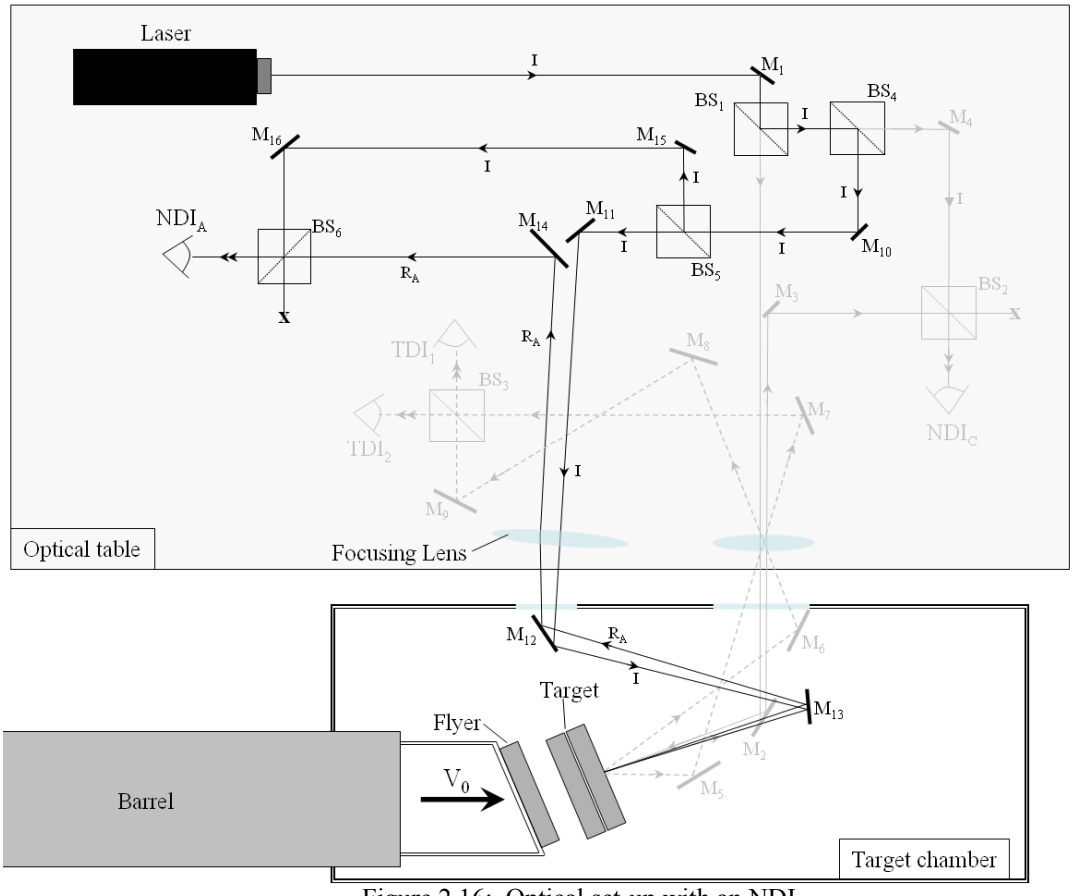

Figure 2.16: Optical set-up with an NDI$_A$.

2.2.5c Triggering

The record length of the oscilloscopes used is less than 20 μs and must capture the entire duration of the test, which lasts over 3 μs. Therefore it is crucial that the oscilloscopes are triggered to start recording at the appropriate time. The most common and reliable triggering method is a point of contact technique where the flyer contacts a wire that is flush with the surface of the target. This contact would close an electrical circuit which triggers the oscilloscopes. Unfortunately, the magnetic field produced by the induction coil causes erroneous triggers with this method.

Therefore, for elevated temperature tests, the oscilloscopes are trigged using the interferometer signal traces with slew triggering for a Tektronix TDS 684A oscilloscope and glitch triggering on an Hewlett Packard 54542A oscilloscope. For slew triggering, the trace signal must pass through a user-defined high and low voltage threshold in less than a specified time interval. When that criterion is met, the oscilloscope is triggered. For glitch triggering, a single voltage level is set and the trace signal must cross that level twice in less than a user specified time. Satisfying that criterion will trigger the oscilloscope.

For several shots, the TDI signals were used to trigger the oscilloscopes. However, at the highest temperatures, there was concern that the frequency of the TDI signals might be too low to trigger the oscilloscopes. Both oscilloscopes also have a built-in function that prohibits triggering if the frequency of the signal is too high. This function is built-in to prevent spurious noise in the signal from triggering the oscilloscopes. Unfortunately, the frequency of the NDI trace is higher than is allowed to trigger the oscilloscopes. Therefore, in order to trigger the oscilloscopes at the highest

temperatures, a different interferometer, which is a desensitized normal displacement interferometer (DNDI), is employed. The DNDI was developed by Espinosa et al. (1996) as a byproduct of their development of the variable sensitivity displacement interferometer (VSDI). The DNDI is formed by combining a first order diffracted beam with the zeroth order reflected beam. The resulting interfering beam will produce a signal that is predictable and has a frequency can trigger the oscilloscopes. The optical setup that includes the DNDI is shown in Figure 2.17.

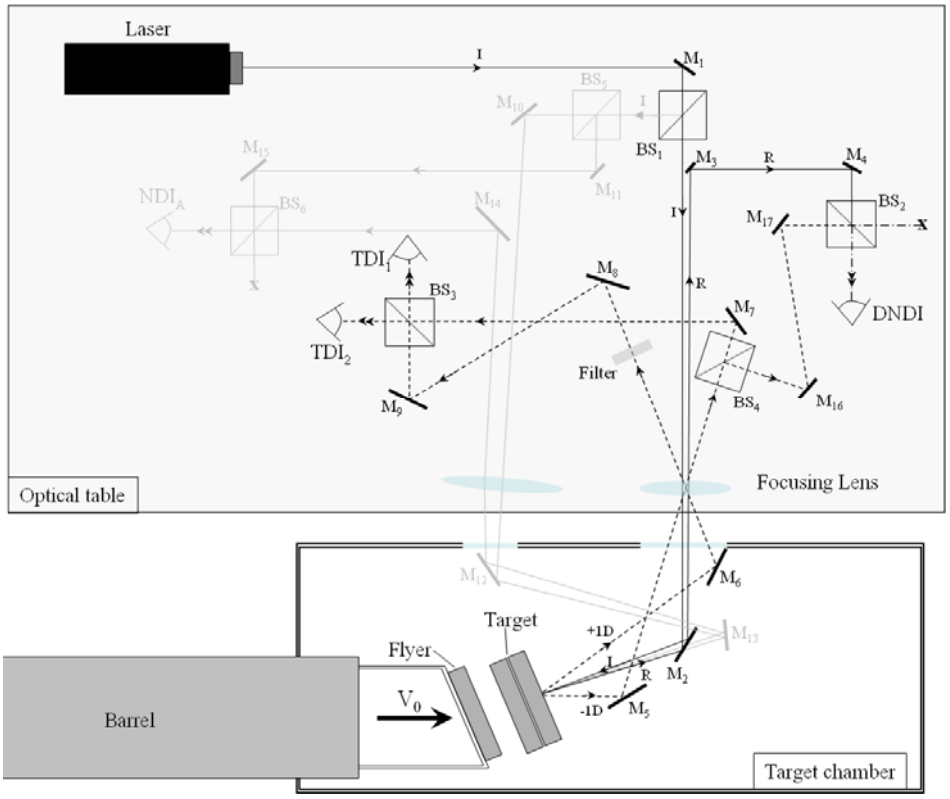

Figure 2.17: Optical set-up with a DNDI.

2.2.6 Alignment technique

Tilt between the flyer and target at impact will generate plane waves that are inclined to the plate surfaces. These inclined waves complicate the calculation of the stress in the sample. Tilt angles less than two milliradians are considered small enough to

use the stress calculations outlined in Section 2.1 because the effect of the inclined waves caused by this tilt is well within the error inherent in the experiment (Klopp and Clifton (1990)). In order to maintain this extremely tight tolerance, the target is first aligned to the flyer to within 0.02 *mrad* using the alignment technique developed by Kumar and Clifton (1977). Then, an optical lever is used to monitor the tilting of the target as it is heated. Any tilt induced by thermal expansion is corrected using remote tilt controls.

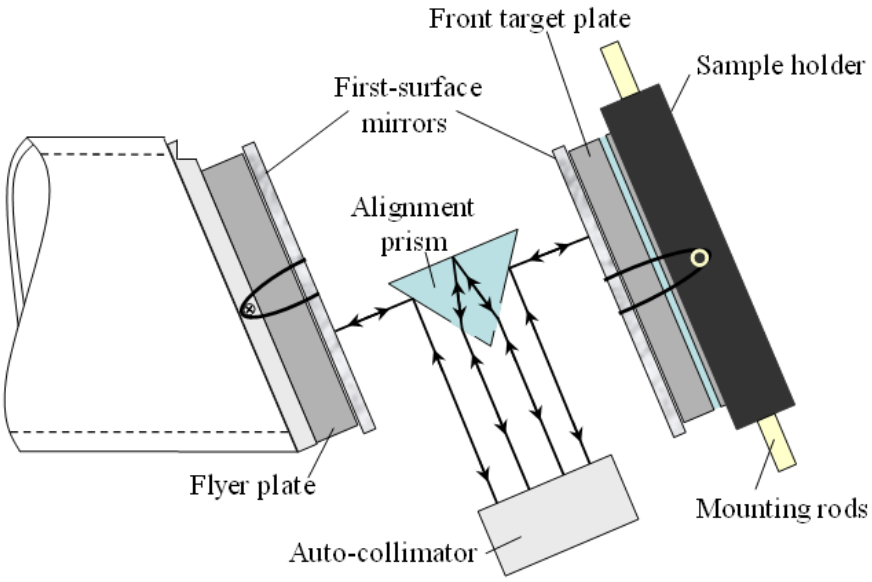

Figure 2.18: Schematic of optical alignment.

2.2.6a Initial alignment

After the flyer orientation has been fixed, by gluing the end cap on the projectile, the impact surface of the target is aligned to be parallel to the impact face of the flyer. First-surface mirrors are placed on the flyer and target plates to assist the optical alignment technique by providing reflective surfaces that are parallel to their respective impact surfaces. A schematic of the optical alignment technique is shown in Figure 2.18. The alignment is done with the use of an alignment prism, which is a partially-silvered,

precision, 90-degree triangular prism. When the prism is viewed straight on with an auto-collimator (as shown in Figure 2.18), a single spot is seen. The prism is aligned to the flyer by observing when a spot reflected off the flyer plate's first-surface mirror overlaps with the spot seen by looking at the prism straight on. This occurs when the rear surface of the prism is perpendicular to the surface of the flyer. Next, the target is aligned to be parallel to the flyer plate, which occurs when the reflection off the target's first surface mirror overlaps with the other two spots. The three spots are shown, as they are seen through the auto-collimator, when they are not aligned in Figure 2.19. This method will get the surfaces parallel to within 0.02 *mrad*.

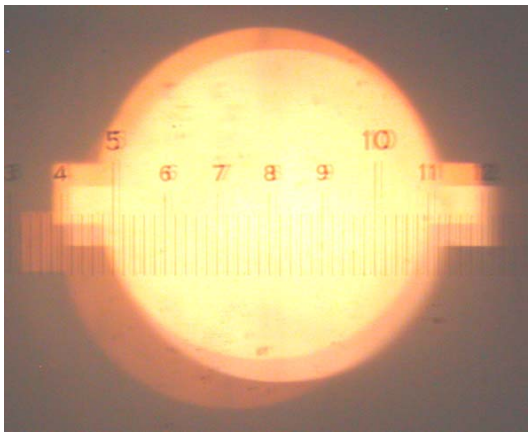

Figure 2.19: Alignment beams seen through the auto-collimator when the system is out of alignment.

2.2.6b Optical lever

In order for the impact faces to remain sufficiently parallel until the time of the shot, an optical lever is used to monitor the tilt of the target after the prism and other alignment equipment have been removed from the chamber. The reflected beam R_A (Figure 2.16), which is used in the NDI_A, is used as the optical lever (or alignment beam). The incident beam for the NDI_A passes directly through the center of the lens that focuses it to a spot on the rear surface of the target. The beam reflected back does not return to

the exact center of the lens. This means that when the lens is present, the incident beam and the reflected beam will be parallel to each other on the optical-table-side of the lens. When the lens is removed, the beams will continue to separate (as seen in Figure 2.20) and the reflected beam will reflect wide of the beam splitter used to form the NDI_A and can be used as an optical lever. After the initial alignment is done (as described in Section 2.2.6a), the R_A beam is reflected across the length of the optical table seven times and directed to a spot on the far wall of the lab. This produces an optical lever that is approximately 83 *ft* (25 *m*) long. Every inch (25.4 *mm*) the alignment beam moves on the wall corresponds to 0.5 *mrad* of tilt of the rear surface of the target.

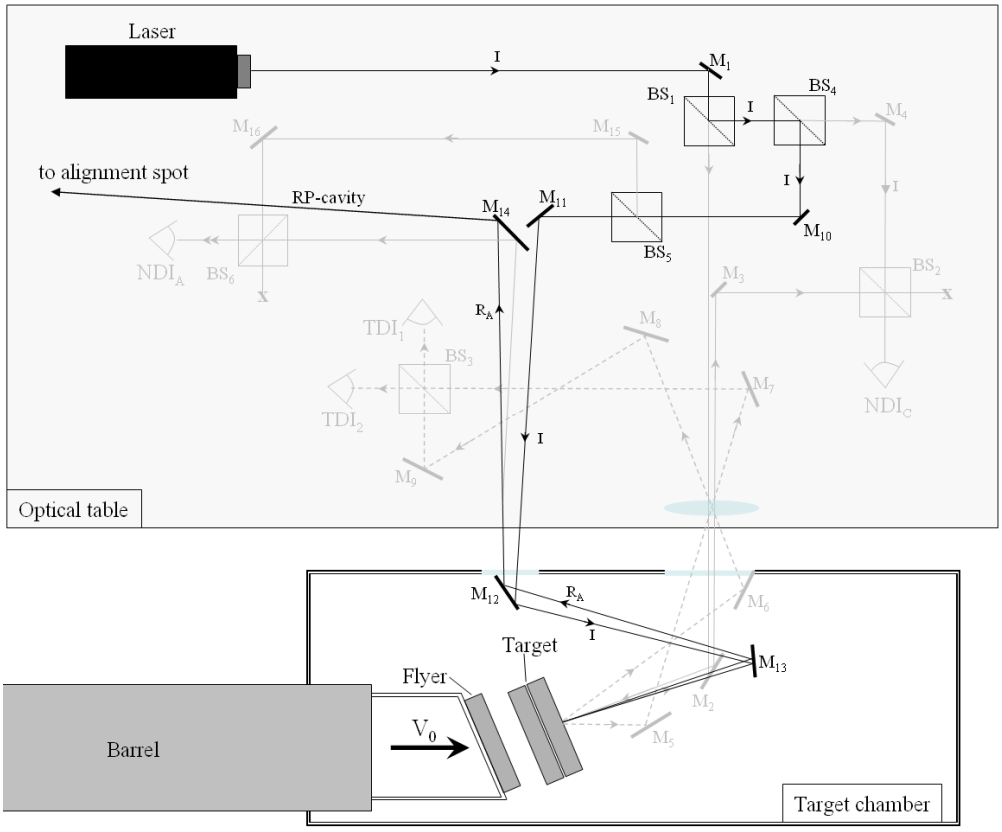

Figure 2.20: Optical set-up for the optical lever.

When the target is being heated, uneven thermal expansion can cause tilt that has to be corrected before the shot is fired. The high-temperature target holder is equipped with remote tilt controls that can correct this tilt from outside the chamber. Using these remote controls, one can return the alignment spot to its original position, thereby returning the target to the correct orientation. After the tilt has been corrected, the focusing lens is returned and the NDI_A is formed again.

2.2.7 Tilt analysis

As previously mentioned, a tilt of less than two milliradians is considered acceptable for these plate impact experiments. Therefore, it is necessary to measure this tilt angle at impact in order to verify the validity of a shot. The motion induced by the inclined longitudinal wave provides all the information necessary to calculate tilt angle and the closure angle Ω (see Figure 2.21). The arrival times of the longitudinal wave at the spots monitored by the NDI_C and NDI_A give the laboratory vertical tilt (tilt around a horizontal axis). The transverse motion induced by the longitudinal wave provides information about the tilt in the horizontal direction (tilt around a vertical axis) (Frutschy (1997)).

The distance between the NDI_C and NDI_A measured spots (Δy) divided by difference in arrival times (Δt) of the longitudinal wave at those spots yields the vertical closure velocity, V_{CL}^{v}. The overall closure velocity V_{CL} is equal to the vertical closure velocity multiplied by the cosine of the closure angle, Ω. The relation between the closure velocity and the tilt angle α is given by:

$$\sin\alpha = \frac{V_0 \cos\theta}{V_{CL}} \approx \alpha . \tag{2.27}$$

The closure angle can then be given by:

$$\Omega = \cos^{-1}\left(\frac{V_0 \cos\theta}{\alpha V_{CL}^{v}}\right) = \cos^{-1}\left(\frac{V_0 \cos\theta \Delta t}{\alpha \Delta y}\right) \tag{2.28}$$

A program was written in Mathematica based on the theory outlined by Klopp and Clifton (1990) to solve the refracted wave problem for wave propagation in the target plate for impact with tilt. The values for V_0, θ, Δt, and Δy are all known and are entered into the code. The values for the tilt α and the closure angle Ω are iterated until the calculated transverse free surface velocity of the target due solely to the inclined longitudinal wave (before the arrival of the shear wave at the rear surface) matches the velocity observed experimentally.

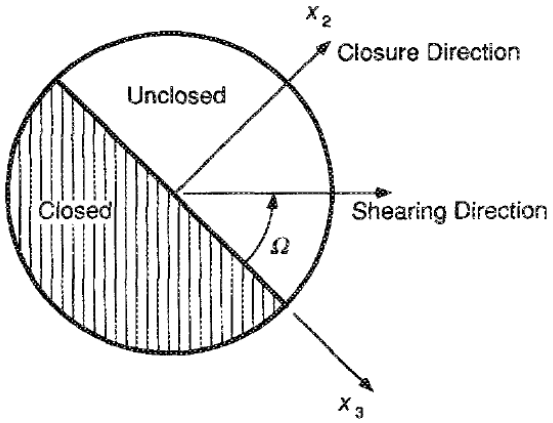

Figure 2.21: Orientation of closure direction relative to shearing direction (FIG. 2 in Klopp and Clifton (1990)).

2.2.8 Conducting the experiment

After the target assembly and projectile have been prepared, the projectile is again put into the barrel with the flyer plate sticking out of the muzzle of the barrel. The target assembly is placed in the target holder so that it is directly centered in the path of the

flyer plate and is locked in place. Thermocouple wires are connected to the temperature monitors. The initial alignment is done using the technique outlined previously. After the target has been aligned to the flyer, the optics are set up to monitor the normal and transverse rear surface motion of the target. When the optics have been set up and the alignment has been rechecked, the optical lever is set up to monitor tilt. Then, the alignment equipment is removed, the projectile is drawn back to the breach end of the barrel and the velocity sensor is put in place at the muzzle end of the barrel. The catcher is then placed in the chamber, the chamber door is closed and the gun breech is sealed.

A mechanical pump is used to obtain a rough vacuum (~60 *mTorr*) in the target chamber so that there will be no air-cushion between the flyer and target at impact. After the rough vacuum has been obtained, the induction heater is turned on and the target is heated automatically, using the Watlow temperature controller, at a rate of 500^{o}C/hr. Once the desired starting temperature has been reached and the alignment beam has settled, any tilt induced by uneven thermal expansion is corrected using the remote tilt controls.

The focusing lens used in the NDI_A is replaced, the optics are retuned, and the oscilloscopes are set to await trigger. The gun is pressurized with nitrogen gas to a load pressure between 115 *psi* and 950 *psi* in order to obtain a desired projectile velocity. The compressed gas is rapidly released and the projectile is accelerated down the barrel to produce impact.

Afterward, the induction heater, laser and vacuum are turned off and the pressure in the chamber is released. The NDI, TDI and DNDI records are saved and analyzed.

2.3 Room temperature experiment

A pressure-shear plate impact experiment was conducted on aluminum at room temperature. For this test, the aluminum sample was sandwiched between the tungsten carbide loading plates and held together with epoxy, which would not have held for the elevated temperature tests. Four wires were lapped flush with the impact surface of the target near the edges. These wires were used to measure the tilt and trigger the oscilloscopes at impact. The times when the flyer plate contacts these electrically biased wires were recorded and used to calculate the tilt. No thermocouples were necessary for this experiment. The target was glued into a delrin sample holder that was secured in a target holder that is not equipped with an induction coil or remote tilt controls.

The grating used for room-temperature experiment was a photoresist grating. The photoresist was spun on the rear surface of the target and then soft baked. The photoresist was then exposed to two laser beams with the same wavelength from opposite angles. The interference of these two beams produces a fringe pattern of light or dark lines. The frequency of the lines is dependent on the angle at which the beams interfere. After exposure, the photoresist was developed revealing a grating pattern in the photoresist. The grating frequency produced for this experiment was 600 lines per millimeter. This method could not be used at elevated temperatures because the photoresist would break down at high temperatures.

The rest of the experiment was conducted in a manner similar to that used for the high-temperature experiments.

Chapter 3

Thermal analysis

Prior to impact in high-temperature pressure-shear plate impact experiments, the temperature near the edge of the sample is monitored using thermocouples as described in Sections 2.2.2 and 2.2.8. However, since the motions measured at the rear surface of the target assembly are induced by waves that have propagated through the center of the sample, it is the temperature at the center of the sample that is relevant. Therefore, a full finite element analysis was done using Abaqus to predict the temperature in the center of the sample following the method laid out by Frutschy (1997). This method is discussed and the starting temperatures T_0 at the center of the sample are estimated in Section 3.2.

In pressure-shear plate impact experiments, the sample is subjected to large pressures and undergoes large plastic deformations. The sample temperature is increased by both the increased pressure and the plastic work done to the sample. Also, the melting temperature for aluminum is higher at larger pressures.

Boehler and Ross (1997) measured the melting curve of 99.999% pure aluminum up to a pressure of 80 GPa using a laser-heated diamond cell. Excellent agreement was

found between their results and theoretical calculations. They found that the melting curve of 99.999% aluminum is best fit by the following relation:

$$T_m = T_{m0}\left(\frac{P}{6.049}+1\right)^{0.531} \tag{3.1}$$

where the ambient melting temperature T_{m0} is 933K (660^{o}C) and P is the current pressure in GPa. The melting curve for 99.999% pure aluminum is shown in Figure 3.1 up to pressures of 8 GPa.

The dynamic evolution of the sample temperature is estimated using the thermodynamic analysis presented in the following section.

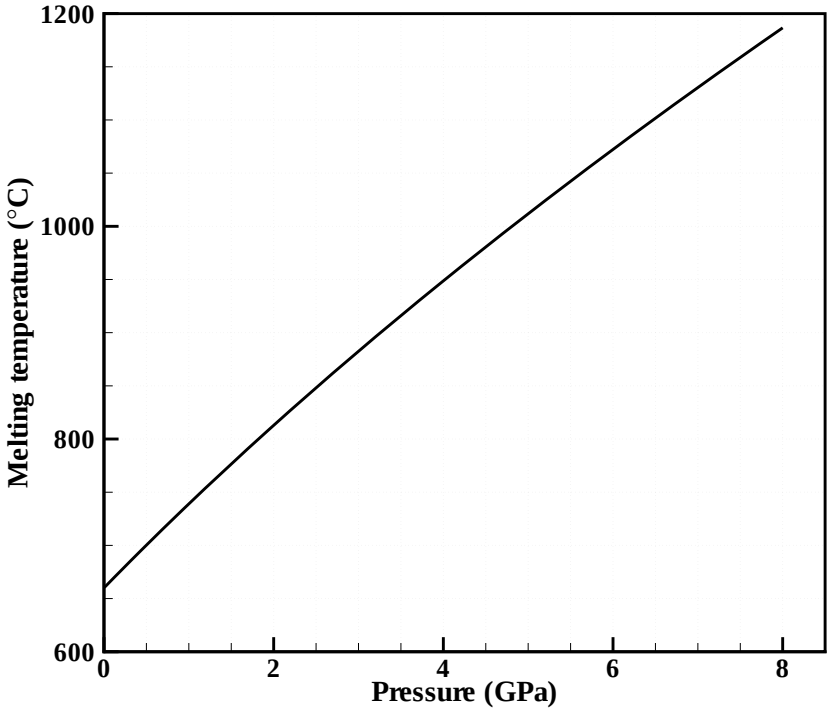

Figure 3.1: Melting curve for high purity aluminum.

3.1 Thermodynamic analysis

Many authors conducting dynamic experiments, including Nemat-Nasser and Guo (2000), Meyers et al. (2001), and Frutschy (1997), have estimated temperature change by assuming adiabatic heating and converting a fraction (usually 90%) of the plastic work into heat.

$$T_f \approx T_0 + \chi\left(\frac{\bar{\gamma}_p \bar{\tau}}{\rho_0 c_P}\right) \tag{3.1}$$

where T_0 and T_f are the measured initial and estimated final temperatures respectively, χ is the fraction of plastic work converted to heat, $\bar{\tau}$ is the average effective flow stress, $\bar{\gamma}_p$ is the effective total plastic strain, ρ_0 is the initial mass density and c_P is the specific heat capacity at constant pressure.

For pressure-shear plate impact experiments, which impose large pressures on the sample, it is important to also consider temperature changes due to pressure changes. A detailed thermodynamic analysis which includes the contribution to temperature change due to pressure change follows.

3.1.1 Thermodynamics analysis of pressure-shear plate impact experiments

From the first law of thermodynamics,

$$dU = \delta Q + \delta W + \delta W', \tag{3.2}$$

where dU is the change in the internal energy for an infinitesimal step in the process and δQ is the incremental quantity of heat transferred to the sample across its boundary. δW and $\delta W'$ are incremental quantities of work done on the sample. More specifically, δW is the incremental quantity of reversible work done on the sample by an external pressure

and $\delta W'$ is the incremental quantity of all other work done on the sample during the process.

For the thermodynamic analysis of the pressure-shear plate impact experiment, the process is assumed to be adiabatic, which means there is no heat flow to or from the sample and therefore $\delta Q = 0$ (the validity of this assumption will be discussed in Chapter 5). The total work done on the system is represented by $\delta W + \delta W' = \sigma_{ij} d\varepsilon_{ij} V_0$ where V_0 is the initial volume, σ_{ij} is the stress on the sample and $d\varepsilon_{ij}$ is the incremental change in the total strain, which can be decomposed into an elastic and a plastic part: $d\varepsilon_{ij} = d\varepsilon_{ij}^e + d\varepsilon_{ij}^p$. The reversible (elastic) mechanical work can be written $\delta W = -P d\varepsilon_{ij}^e V_0 = -PdV$, where $P = (trace\sigma)/3$ is pressure and dV is the change in volume of the sample. If the response of the sample is elastic/plastic and plastic incompressibility is assumed, the incremental quantity of the irreversible plastic work can be written $\delta W' = \sigma_{ij}' d\varepsilon_{ij}{}^p V_0$, where σ_{ij}' = S_{ij} is the deviatoric stress, $S = \sigma - 1/3(trace\sigma)\mathrm{I}$. Using J2-flow, theory the irreversible work can be rewritten $\delta W' = \bar{\tau} d\bar{\gamma}_p V_0$ where $\bar{\tau} = \sqrt{\frac{1}{2} S_{ij} S_{ij}}$ is the effective flow stress and $d\bar{\gamma}_p = \sqrt{2 d\varepsilon_{ij}^p d\varepsilon_{ij}^p}$ is the change in effective plastic strain.

Therefore, assuming adiabatic conditions, the change in internal energy of a sample for a pressure-shear plate impact experiment can be written as

$$dU = -PdV + \bar{\tau} d\bar{\gamma}_p V_0 . \tag{3.3}$$

Choosing a reference state where $\bar{\gamma}_p = 0$, $\bar{\tau} = 0$, and $V = V_0$, an irreversible path can be considered where:

$$\frac{dU}{dt} = -P\frac{dV}{dt} + \dot{\bar{\gamma}}_p \bar{\tau} V_0 . \tag{3.4}$$

The time derivative of the internal energy, $U = U(V,S)$, is

$$\frac{dU}{dt} = \left(\frac{\partial U}{\partial V}\right)_S \frac{dV}{dt} + \left(\frac{\partial U}{\partial S}\right)_V \frac{dS}{dt} \quad . \tag{3.5}$$

where

$$\left(\frac{\partial U}{\partial V}\right)_S = -P \qquad \text{and} \qquad \left(\frac{\partial U}{\partial S}\right)_V = T . \tag{3.6}$$

Therefore, from Equations (3.5) and (3.6)

$$\frac{dU}{dt} = -P\frac{dV}{dt} + T\frac{dS}{dt} . \tag{3.7}$$

Equations (3.4) and (3.7) lead to

$$T\frac{dS}{dt} = \dot{\bar{\gamma}}_p \bar{\tau} V_0 . \tag{3.8}$$

Taking the time derivative of entropy, $S = S(T,P)$, one finds

$$\frac{dS}{dt} = \left(\frac{\partial S}{\partial T}\right)_P \frac{dT}{dt} + \left(\frac{\partial S}{\partial P}\right)_T \frac{dP}{dt} . \tag{3.9}$$

From the definition of heat capacity, C_P:

$$\left(\frac{\partial S}{\partial T}\right)_P = \frac{C_P}{T} . \tag{3.10}$$

Substituting Equations (3.9) and (3.10) into Equation (3.8) one gets

$$C_P\frac{dT}{dt} + T\left(\frac{\partial S}{\partial P}\right)_T \frac{dP}{dt} = \bar{\tau}\dot{\bar{\gamma}}_p V_0 . \tag{3.11}$$

From the Maxwell relation

$$\left(\frac{\partial S}{\partial P}\right)_T = -\left(\frac{\partial V}{\partial T}\right)_P \tag{3.12}$$

and the definition of the coefficient of thermal expansion

$$\alpha = \frac{1}{V_0}\left(\frac{\partial V}{\partial T}\right)_P \tag{3.13}$$

Equation (3.11) reduces to

$$C_P \frac{dT}{dt} - TV_0\alpha\frac{dP}{dt} = \bar{\tau}\dot{\bar{\gamma}}_p V_0 \,. \tag{3.14}$$

Equation (3.14) can be integrated over time and rearranged to find the temperature change:

$$dT = \frac{\bar{\tau}d\bar{\gamma}_p V_0 + TV_0 dP\alpha}{C_P}. \tag{3.15}$$

C_P is the heat capacity and can be replaced by $c_P M_0$ where M_0 is the initial mass and c_P is the specific heat capacity with the units $J/(kgK)$. Also note that $M_0 = \rho_0 V_0$ where ρ_0 is the initial mass density. Therefore, after some algebraic manipulation, the temperature change in the sample can be written:

$$dT \cong \frac{\bar{\tau}d\bar{\gamma}_p + TdP\alpha}{\rho_0 c_P}. \tag{3.16}$$

The values for pressure *P*, effective flow stress $\bar{\tau}$ and effective plastic strain $\bar{\gamma}_p$ are calculated from measurements taken during the experiment. The initial density ρ_0, the coefficient of thermal expansion α, and the specific heat capacity c_P are all known for aluminum at ambient conditions and can be calculated at elevated temperatures and

pressures. Therefore, throughout the test, the change in temperature of the sample can be estimated using Equation (3.16).

If there is no change in pressure (i.e. $dP = 0$) and the fraction of plastic work converted into heat is unity (i.e. $\chi = 1$), Equation (3.16) reduces to Equation (3.1). The coefficient of thermal expansion varies with temperature and the specific heat capacity varies with both temperature and pressure. Those properties are discussed in the next section.

3.1.2 The coefficient of thermal expansion and the specific heat capacity of aluminum at elevated temperatures and large pressures

The volumetric coefficient of thermal expansion for aluminum is given by Raju et al. (2002) for a range of temperatures up to the ambient melting temperature. However, it is possible to reach sample temperatures that are above the ambient melting temperature while still below the current melting temperature if the sample is subjected to large pressures. Therefore, it is necessary to extrapolate the values of the volumetric coefficient of thermal expansion to temperatures above the ambient melting temperature for aluminum (Figure 3.2).

The specific heat capacity of aluminum varies with temperature, but it also varies significantly with pressure. Raju et al. (2001) and Brooks and Bingham (1968) present values for specific heat capacity of aluminum over a range of temperature that approach ambient melt. These values are averaged and extrapolated to temperatures above the ambient melting temperature (Figure 3.3). Kuchhal et al. (1997), Kuchhal et al (1998), and Kumari and Dass (1990) have worked through how to determine the pressure and

temperature dependence of heat capacity in condensed matter. That derivation is shown here and applied to aluminum.

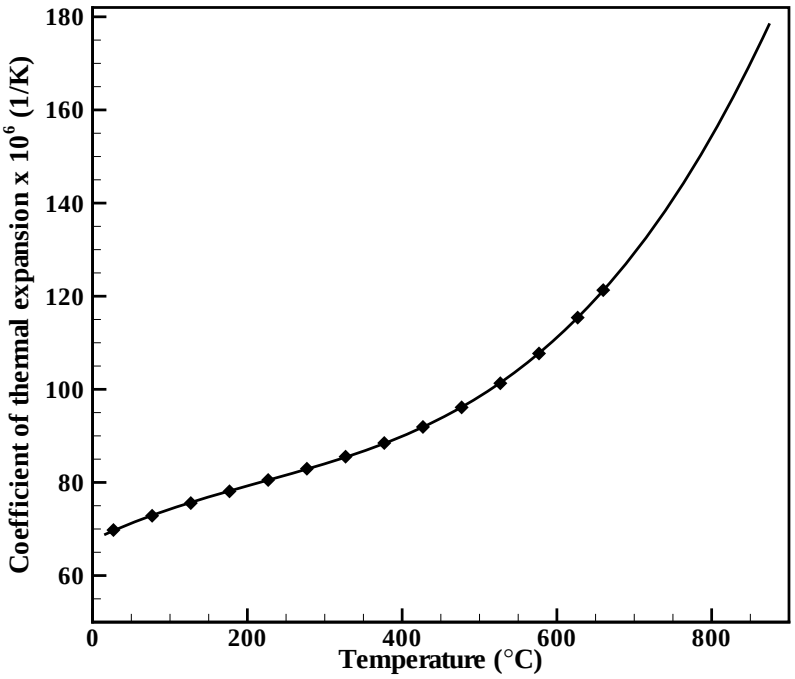

Figure 3.2: Coefficient of volumetric thermal expansion for high purity aluminum (Raju et al. (2002)) extrapolated to higher temperatures.

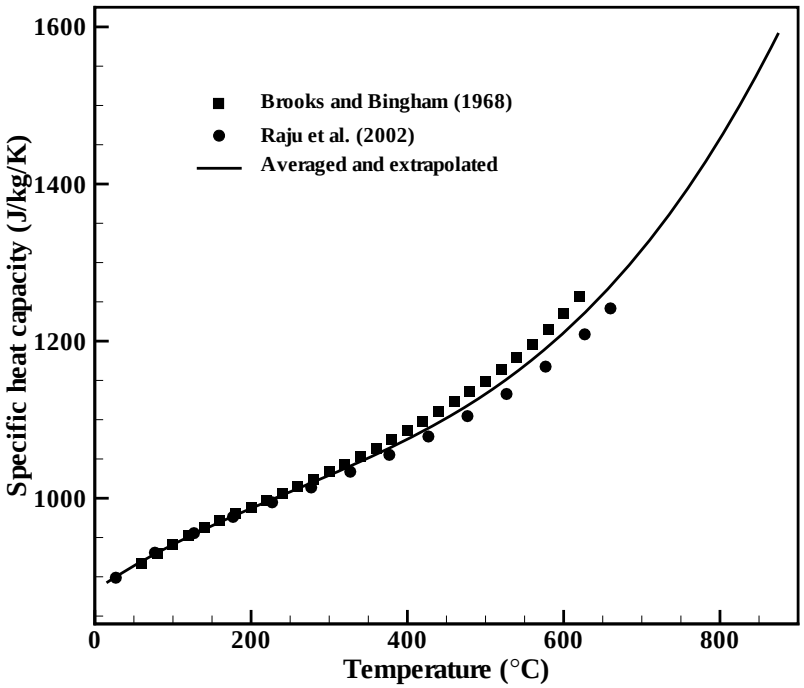

Figure 3.3: Specific heat capacity of aluminum at ambient pressures versus temperature.

The thermodynamic relation

$$\left[\frac{\partial C_P(P,T)}{\partial P}\right]_T = -T\left[\frac{\partial^2 V(P,T)}{\partial T^2}\right]_P, \tag{3.17}$$

can be rewritten (Cf. Equation 6 in Kuchhal et al. (1998))

$$\left[\frac{\partial C_P(P,T)}{\partial P}\right]_T = -T\xi^2\left[\frac{\partial^2 V(P,T)}{\partial P^2}\right]_T = -T\xi^2\left[\frac{\partial}{\partial P}\left(-\frac{V(P,T)}{B_T(P,T)}\right)_T\right] \tag{3.18}$$

where $V(P,T)$ is the specific volume at pressure P and temperature T, $B_T(P,T)$ is the isothermal bulk modulus at pressure P and temperature T and

$$\xi = \left(\frac{\partial P}{\partial T}\right)_V = \alpha(P,T)B_T(P,T) = \alpha(0,T_R)B_T(0,T_R). \tag{3.19}$$

Here, as in Kuchhal et al. (1997), it is assumed that the product of the coefficient of thermal expansion and the isothermal bulk modulus is independent of pressure. T_R is a reference temperature (298 K).

Using Equations (3.18) and (3.19) and integrating (3.17) one obtains

$$C_P(P,T) = C_P(0,T) + \xi^2 T\left[\frac{V(P,T)}{B_T(P,T)} - \frac{V(0,T)}{B_T(0,T)}\right]. \tag{3.20}$$

The values $C_P(0,T)$, ξ and T are known. None of the values in the bracket in Equation (3.20) are known directly. However, the specific volume at ambient temperature and pressure is known to be the inverse of the initial density, $V(0,T_R) = \frac{1}{\rho_0}$. And the value of the isothermal bulk modulus is also known under ambient conditions, $B_T(0,T_R)$. Also, as it will be shown, the ratios $\left[\frac{V(P,T)}{V(0,T_R)}\right]$ and $\left[\frac{B_T(0,T_R)}{B_T(P,T)}\right]$ can be calculated. By rearranging Equation (3.20) and introducing the ratio of the specific volume to the

isothermal bulk modulus at ambient conditions yields (Cf. Equation (3) of Kuchhal et al. (1998))

$$C_P(P,T) = C_P(0,T) + \xi^2 T \frac{V(0,T_R)}{B_T(0,T_R)}\left[\frac{V(P,T)}{V(0,T_R)}\frac{B_T(0,T_R)}{B_T(P,T)} - \frac{V(0,T)}{V(0,T_R)}\frac{B_T(0,T_R)}{B_T(0,T)}\right]. \quad (3.21)$$

Kumari and Dass (1990) assume that the ratio of the second to first pressure derivatives of the isothermal bulk modulus is pressure independent (Cf. Equation (1) Kumari and Dass (1990)),

$$\frac{\left[\frac{\partial^2 B_T(P,T)}{\partial P^2}\right]_T}{\left[\frac{\partial B_T(P,T)}{\partial P}\right]_T} = -Z\,. \quad (3.22)$$

Integration of Equation (3.22) yields

$$B_T'(P,T) = B_T'(0,T_R)\exp(-ZP), \quad (3.23)$$

$$B_T(P,T) = B_T(0,T_R) + \left[\frac{B_T'(0,T_R)}{Z}\right]\left[1-\exp(-ZP)\right], \quad (3.24)$$

and

$$\frac{V(P,T_R)}{V(0,T_R)} = \left[(1+\beta)\exp(ZP) - \beta\right]^{-1/\eta}, \quad (3.25)$$

where $\beta = \dfrac{B_T'(0,T_R)}{B_T(0,T_R)Z}$ and $\eta = B_T'(0,T_R) + ZB_T(0,T_R)$.

Dividing Equation (3.24) through by $B_T(0,T_R)$, one gets

$$\frac{B_T(P,T)}{B_T(0,T_R)} = 1 + \beta\left[1-\exp(-ZP)\right]. \quad (3.26)$$

Kuchhal et al (1997) now alters the isothermal EOS to include thermal effects such that

$$P(T) = P(T_R) + \xi(T - T_R) \tag{3.27}$$

Inserting Equation (3.27) into Equations (3.25) and (3.26) gives

$$\frac{V(P,T_R)}{V(0,T_R)} = \left[(1+\beta)\exp\left(Z\left[P - \xi(T - T_R)\right]\right) - \beta\right]^{-1/\eta} \tag{3.28}$$

and

$$\frac{B_T(P,T)}{B_T(0,T_R)} = 1 + \beta\left[1 - \exp\left(-Z\left[P - \xi(T - T_R)\right]\right)\right]. \tag{3.29}$$

Values for $B_T(0,T_R)$ and $B_T'(0,T_R)$ for aluminum can be found in the literature (Syassen and Holzapfel (1978)). Equations (3.28) and (3.29) can be substituted into Equation (3.21) to find the specific heat capacity at a given temperature and pressure. Figure 3.4 shows the specific heat capacity as a function of pressure at three constant temperatures.

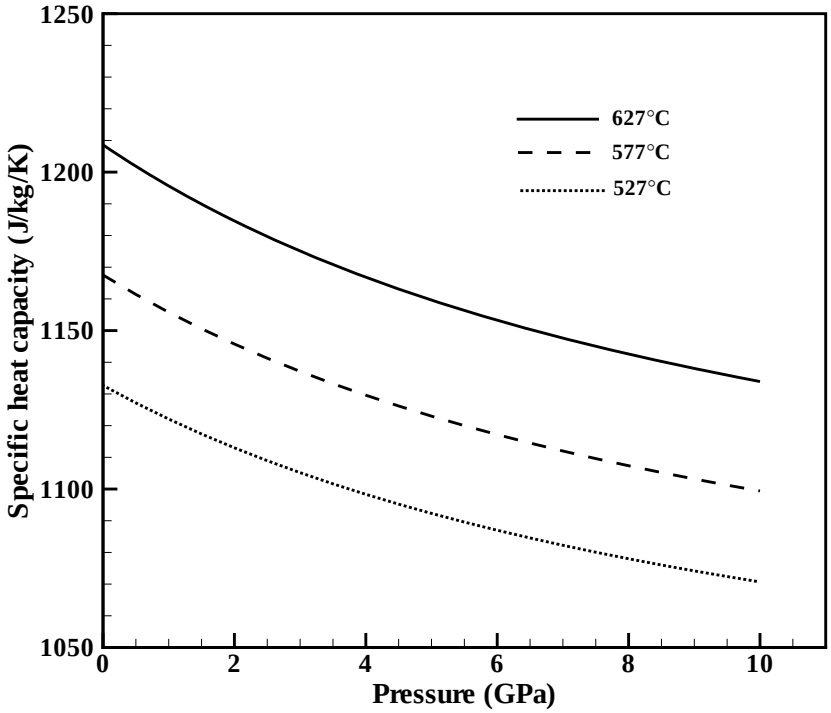

Figure 3.4: Specific heat capacity of aluminum as a function of pressure shown at three constant temperatures.

3.2 Centerline starting temperatures

A full-body finite element analysis using Abaqus was conducted to predict the temperature at the center of the sample from the temperatures measured by the thermocouples located near the edge of the sample. The elements were roughly square, 4-node, linear, axisymmetric heat transfer quadrilateral elements.

Since a large portion of the total power input produced by the magnetic field of the induction coil is concentrated in the skin depth of the target plates (Frutschy (1997)) – approximately 0.4 *mm* for tungsten carbide – the heat input is made to be a constant flux at the surface of the outer edge of the target (surface B in Figure 3.5). The heat loss from a given surface per unit area can be written

$$q_{rad} = \varepsilon\sigma\left(T^4 - T_0^4\right) \tag{3.30}$$

where ε is emissivity, T is the surface temperature, T_0 is the background temperature and σ is the Stefan-Boltzmann constant. The emissivity of surfaces J and I are set to zero because surface J is the symmetric interface and surface I has a mirror-quality polish (Figure 3.5). The emissivity values for the all the surfaces are listed in Table 3.1. The lava stone target holder was taken to be in perfect thermal contact with the rear target plate. To find the centerline temperature (surface J), the flux into surface B was iterated until the temperature at the thermocouple location (marked by a * in Figure 3.5) matched the temperature measured by the thermocouple in the experiments. The temperature contours for shot SG0802 are shown in Figure 3.5. A temperature drop of around 8^{o}C is observed between the thermocouple position and the centerline. Note that the temperature difference between the front of the target and the rear of the target along the centerline is

less than 1°C. The starting temperatures at the centerline for all elevated temperature shots are listed in Table 4.4.

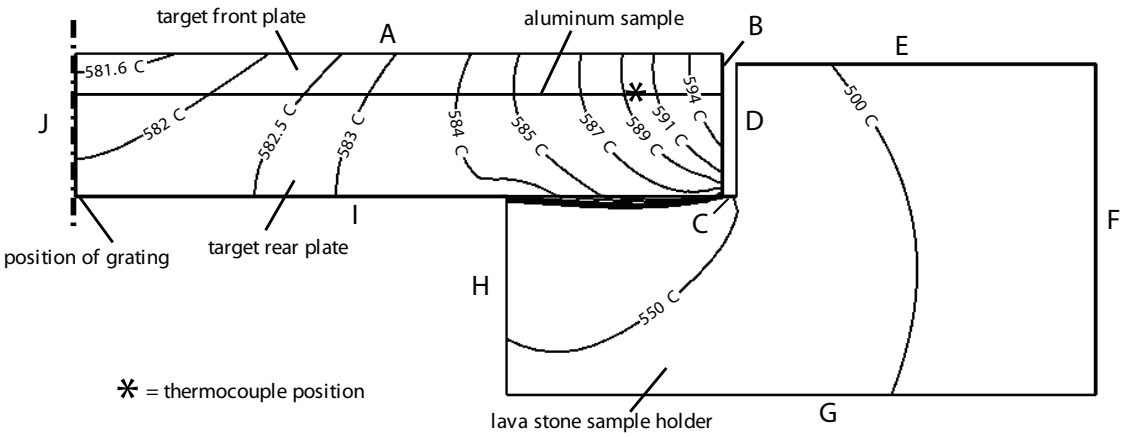

Figure 3.5: Temperature field prediction for shot SG0802.

Table 3.1: Emissivity values used for Abaqus centerline temperature calculations.

surface	A	C	D	E	F	G	H	I	J
emissivity	0.7	0.9	0.9	0.9	0.9	0.9	0.9	0	0

Chapter 4

Experimental Results

For this study, pressure-shear plate impact experiments were conducted on thin ($10 - 25\,\mu m$) aluminum samples, which were sandwiched between tungsten carbide target plates and impacted by a tungsten carbide flyer plate. The experiments were conducted at room temperature and at elevated temperatures up to starting temperatures of 591°C. It is essential to the interpretation of these experiments that the dynamic response of the tungsten carbide plates be known for the temperatures and stresses that these plates experience during the experiments. Therefore, symmetric impact tests, where the flyer and target are both tungsten carbide – and there is no sample foil – were conducted at temperatures up to 643°C in order to characterize the response of the tungsten carbide under stresses and temperatures that result in the sandwich tests on aluminum.

4.1 Symmetric impact tests on tungsten carbide

Tungsten carbide is a high impedance, high yield strength material with a high melting temperature. Through symmetric impact tests on pure tungsten carbide at elevated temperature, Frutschy and Clifton (1998b) showed that pure tungsten carbide is

an excellent material to use for loading plates in high-temperature pressure-shear plate impact experiments.

The target plates used for the sandwich shots reported here were made of a tungsten carbide material with 6% cobalt binder called WC#832 (see Table 4.1 for complete composition). These plates, obtained from Valenite, Inc., were 50 *mm* diameter discs – approximately 4 *mm* thick. Symmetric impact tests were conducted on these plates to validate their use as loading plates for the experiments on aluminum. The wave theory used to relate the free surface velocities measured in those experiments to the stresses in the tungsten carbide target plates is described in the following section (Section 4.1.1). The results of the symmetric impact tests are reported in Section 4.1.2.

4.1.1 Rate-independent theory of elastic/plastic wave propagation

Clifton and Bodner (1966) used the one-dimensional, rate-independent theory of elastic-plastic wave propagation to calculate the dynamic stress-strain curve of a long uniform bar subjected to a short compression pulse. A similar analysis can be applied to the symmetric plate impact experiment to relate the measured free surface velocity to the stresses in the tungsten carbide plates (Frutschy and Clifton (1998b)).

Following that analysis, the velocities at the free surface (point *Q*' in Figure 4.1) can be related to the stress at point *Q* in the plate by

$$\sigma(Q) + \rho_0 c_1 u(Q) = \rho c_1 u(Q') \tag{4.1}$$

where c_1 is the longitudinal elastic wave speed at small stresses, u is the longitudinal particle velocity, σ is the normal stress and ρ_0 is the initial mass density. For a point Q

in the simple wave region OAB, the velocity at point Q (e.g. Clifton and Bodner (1966)) is

$$u(Q) = \int_0^{\sigma(Q)} \frac{d\sigma}{\rho_0 c(\sigma)}. \tag{4.2}$$

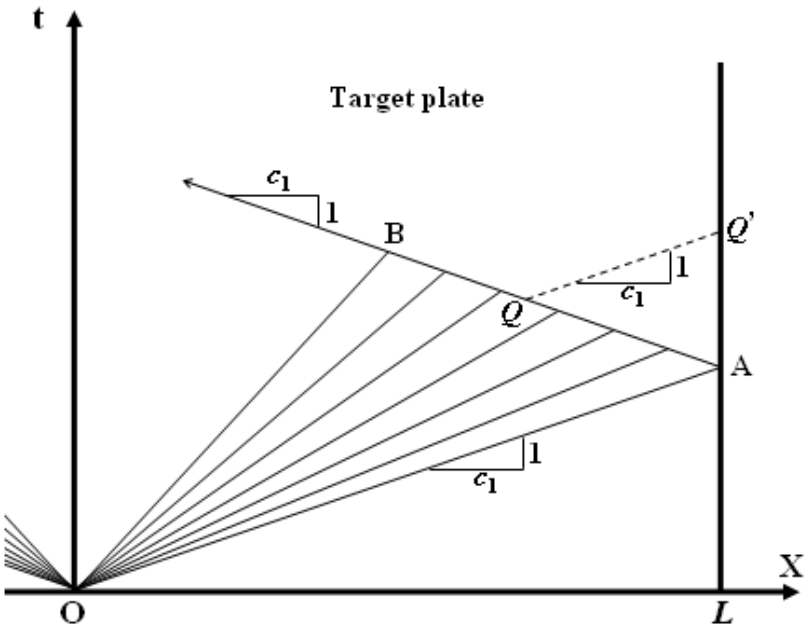

Figure 4.1: Time-distance diagram for simple wave propagation.

Substituting Equation (4.2) into Equation (4.1) one obtains

$$d\sigma(Q) = \frac{\rho_0 c_1}{1 + \frac{c_1}{c(\sigma(Q))}} du(Q'). \tag{4.3}$$

The time after the arrival of the wavefront at the rear surface (marked A on Figure 4.1) can be discretized into intervals corresponding to the sampling rate of the recording oscilloscopes. After n time intervals, the time is represented by $t_n = nh$, where h is the discretized time interval. The point Q_n' denotes Q' at (L, $L/c_1 + t_n$) and the corresponding

point Q is denoted by Q_n. Using an average value for $c(\sigma)$ over the time interval, one can integrate Equation (4.3) to obtain

$$\sigma_n = \sigma_{n-1} + \frac{\rho_0 c_1 (u_n - u_{n-1})}{1 + \frac{c_1}{2}\left(\frac{1}{c_n} + \frac{1}{c_{n-1}}\right)} + \mathrm{O}(\delta\sigma^3) \tag{4.4}$$

where $\sigma_n \equiv \sigma(Q_n)$, $u_n \equiv u(Q_n')$, and $c_n \equiv c(\sigma_n)$. The value for c_n is given by

$$c_n = \frac{2L - (t_n c_1)}{2L + (t_n c_1)}. \tag{4.5}$$

The strain at point Q can be found by changing the variable of integration in Equation (4.2) to obtain

$$u(Q) = \int_0^{\varepsilon(Q)} c(\varepsilon) d\varepsilon \tag{4.6}$$

and then integrating Equation (4.6) from t_{n-1} to t_n , using the relation $2u(Q) = u(Q')$, to obtain

$$\varepsilon_n = \varepsilon_{n-1} + \frac{(u_n - u_{n-1})}{c_n + c_{n-1}} + \mathrm{O}(\delta\varepsilon^3). \tag{4.7}$$

Neglecting higher order terms, one can use the difference equations (Equations (4.4) and (4.7)) to calculate the normal stress-strain curve. The velocity $u(Q')$ is the experimentally measured normal free-surface velocity. In order to calculate the shear stress versus shear strain curve, $u(Q')$ is replaced by the transverse free-surface velocity $v(Q')$ and c_1 is replaced by the elastic shear wave speed c_2.

To use Equations (4.4) and (4.7) to calculate the dynamic stress-strain relation at elevated temperatures, the initial, temperature-dependent stress-free wave speeds of tungsten carbide must be calculated from

$$c_1(T) = \sqrt{\frac{\lambda(T) + 2\mu(T)}{\rho(T)}} \tag{4.8}$$

and

$$c_2(T) = \sqrt{\frac{\mu(T)}{\rho(T)}} \tag{4.9}$$

where $\lambda(T)$ is the Lame modulus and $\mu(T)$ is the shear modulus at temperature *T*. The temperature dependent density $\rho(T)$ can be calculated from the room temperature density and the bulk coefficient of thermal expansion α_{bulk} using the following relation

$$\rho(T) = \frac{\rho(22°C)}{\left[1 + \alpha_{bulk}(T - 22°C)\right]^3}. \tag{4.10}$$

The ratio of the longitudinal wave speed to the shear wave speed yields

$$\frac{c_1(T)}{c_2(T)} = \sqrt{\frac{\lambda(T) + 2\mu(T)}{\mu(T)}}. \tag{4.11}$$

From the definition of the Lamé modulus in terms of the shear modulus and Poisson's ratio $\nu(T)$,

$$\lambda(T) = \frac{2\mu(T)\nu(T)}{1 - 2\nu(T)}, \tag{4.12}$$

the wave speed ratio in Equation (4.11) can be represented in terms of Poisson's ratio alone,

$$\frac{c_1(T)}{c_2(T)} = \sqrt{\frac{2(1 - \nu(T))}{1 - 2\nu(T)}}. \tag{4.13}$$

The temperature dependence of Poisson's ratio for pure tungsten carbide was shown in Frutschy and Clifton (1998b) to have less than a 1 percent effect on the longitudinal and shear wave speeds. Therefore, assuming a similar response for WC#832, Poisson's ratio is taken to be independent of temperature $\nu(T) = \nu(22°C) = \nu$.

The ratio of the longitudinal wave speed at temperature T over the longitudinal wave speed at room temperature gives

$$\frac{c_1(T)}{c_1(22°C)} = \sqrt{\frac{\lambda(T)+2\mu(T)}{\rho(T)}\frac{\rho(22°C)}{\lambda(22°C)+2\mu(22°C)}}\,. \tag{4.14}$$

Using the material constant relations

$$\lambda(T) = \frac{\nu E(T)}{(1+\nu)(1-2\nu)}, \tag{4.15}$$

and

$$\mu(T) = \frac{E(T)}{2(1+\nu)}, \tag{4.16}$$

where $E(T)$ is the Young's modulus at temperature T, Equation (4.14) reduces to

$$\frac{c_1(T)}{c_1(22°C)} = \sqrt{\frac{E(T)}{E(22°C)}\frac{\rho(22°C)}{\rho(T)}}\,. \tag{4.17}$$

Similarly, the ratio of the shear wave speed at temperature T over the shear wave speed at room temperature is found to be

$$\frac{c_2(T)}{c_2(22°C)} = \sqrt{\frac{E(T)}{E(22°C)}\frac{\rho(22°C)}{\rho(T)}}\,. \tag{4.18}$$

Therefore, the wave speeds at a given temperature T can be found if the Young's modulus $E(T)$ is known at that temperature.

Most of the tungsten carbide plates used in the current experiments were manufactured by the Valenite, Inc. and contained between 6-12% cobalt binder. The values for the longitudinal wavespeeds, the densities, and the Young's modulus at ambient conditions, were provided by the manufacturer. The longitudinal wavespeeds were confirmed with an ultrasonic pulse-echo system. The shear wavespeeds were verified using arrival times measured during the pressure-shear plate impact experiment at room temperatures. Pure tungsten carbide was used as the flyer plate in one shot and the material parameters were taken from those reported by Frutschy (1997). The compositions and room-temperature material parameters for the tungsten carbide plates used are shown in Tables 4.1 and 4.2 respectively.

Dawhil and Mal (1965) studied Young's modulus of tungsten carbide as a function of temperature for a variety of compositions (Figure 4.2). The room temperature values of the Young's modulus differ slightly from the values provided here for the tungsten carbide with 6% cobalt. This may be due the small amount of titanium carbide (TiC) and tantalum carbide (TaC) present in tungsten carbide plates used in this study. From Figure 4.2, the variation of the modulus with temperature appears largely independent of cobalt content. Also, looking at the 59%WC-16%TiC-15%TaC-10%Co and 74%WC-16%TiC-10%Co curves, the variation of the modulus with temperature appears to be independent of the tantalum carbide content. Thus it seems reasonable to assume that the Young's modulus of WC#832 has a similar dependence on temperature as that shown for 94%WC-6%Co in Figure 4.2. Based on that assumption, wavespeeds can be found for a given temperature from Equations (4.17) and (4.18). Those

wavespeeds can then be used in Equations (4.4) and (4.7) to calculate the dynamic stress-strain curves from free-surface velocity profiles measured during the symmetric impact tests.

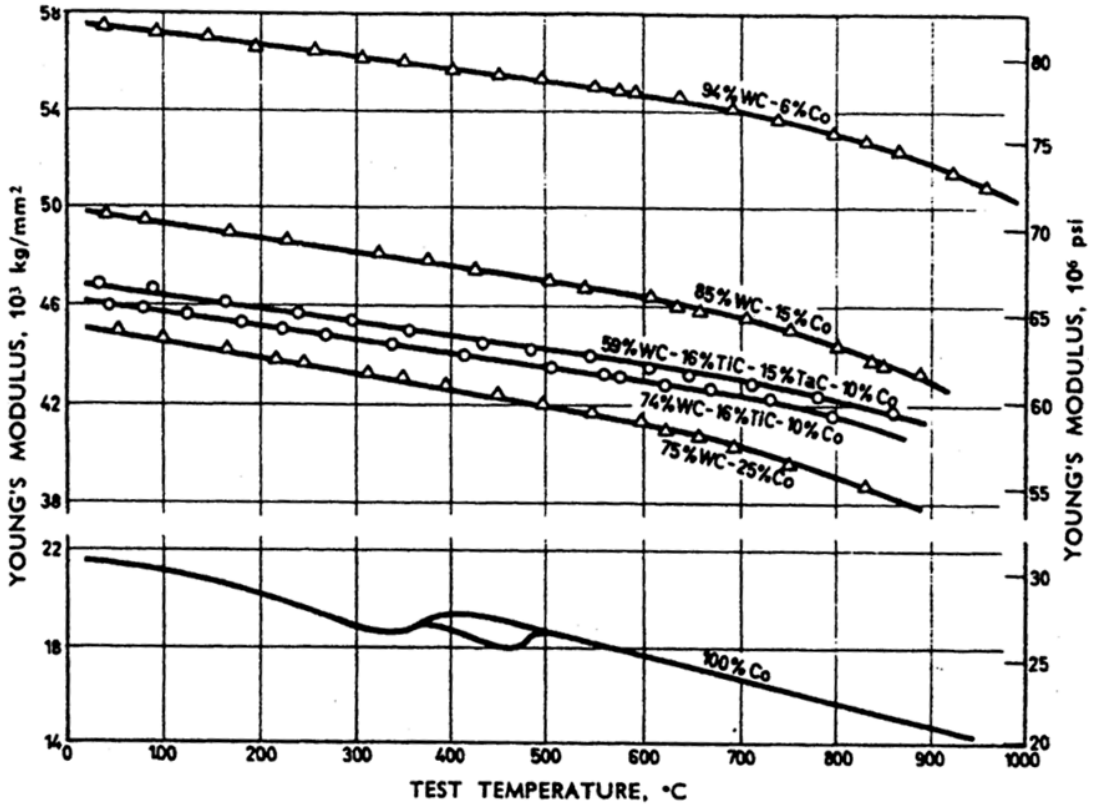

Figure 4.2: Young's modulus as function of temperature for various compositions of tungsten carbide (Fig.4 from Dawhil and Mal (1965)).

4.1.2 Symmetric impact results

Three symmetric impact tests were conducted on tungsten carbide plates with 6% cobalt binder. In shot SG0503, a WC#2 target plate at room temperature was impacted by a WC#2 room-temperature flyer. For shot KF9607, Kristopher Frutschy (Frutschy (1996)) conducted a symmetric impact experiment in which a WC#832 target was heated to 496°C and impacted by a WC#832 room-temperature flyer. And in shot SG0601, a

WC#832 target was heated to 643°C and impacted by a WC#112 room-temperature flyer. The WC#112 flyer was used because it has a better acoustic impedance match with the target than a room temperature WC#832 flyer. The shot conditions for these tests are given in Table 4.3.

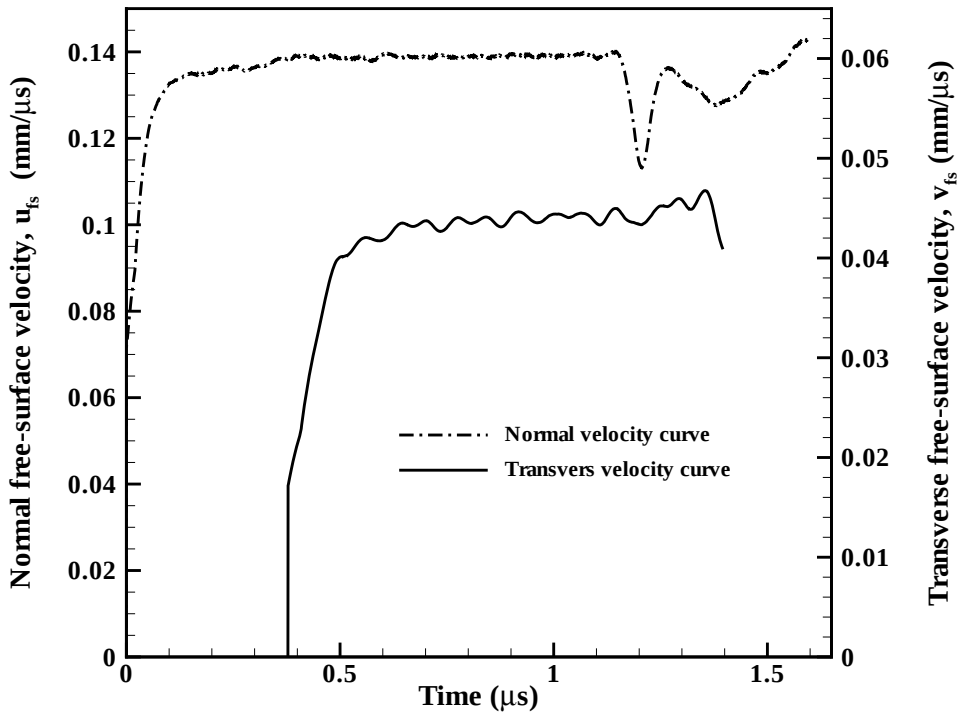

Figure 4.3: Measured normal and transverse free-surface velocities during a symmetric impact test on WC#2 at 22°C (SG0503)

The normal and transverse free-surface velocity-time profiles for shot SG0503 are shown in Figure 4.3. Time zero is taken to be the time when the longitudinal wave arrives at the rear surface of the target. The normal velocity rises sharply and then stays nearly constant at 139 *m/s* until around 1.15 μs when there is a sudden drop in velocity. This drop corresponds to the end of the compressive loading pulse, determined by the thickness of the flyer plate. The shear wave arrives approximately 0.38 μs after the

arrival of the longitudinal wave. The transverse velocity also rises quickly and then reaches a maximum velocity of approximately 45 *m/s*. The end of the transverse velocity record corresponds to the end of the shear loading pulse.

The velocity profiles are used to calculate the dynamic normal and shear stress-strain curves for WC#2 at room temperature (shown in Figures 4.4a and 4.4b). For the compressive stress-strain curve (Figure 4.4a), the slope of the dashed line is equal to $\lambda(22°C)+2\mu(22°C)$ for WC#2. For the shear stress-strain curve (Figure 4.4b), the slope of the dashed line is equal to $\mu(22°C)$ for WC#2. Small deviations from linear response are observed above a compressive stress of 4.8 GPa and a shear stress of 0.79 GPa.

The compressive stress is plotted versus the normal particle velocity in Figure 4.5a. The curve of the shear stress as a function of transverse velocity is shown in Figure 4.5b. For the compressive-stress versus normal-velocity curve (Figure 4.5a), the slope of the dashed line corresponds to the initial, stress-free longitudinal acoustic impedance for WC#2 at room temperature, i.e. $\rho(22°C)c_1(22°C)$. For the shear-stress versus transverse-velocity curve (Figure 4.5b), the slope of the dashed line corresponds to the initial, stress-free shear acoustic impedance for WC#2 at room temperature, i.e. $\rho(22°C)c_2(22°C)$. The experimental results deviate slightly from the ideal linear response only at higher stresses.

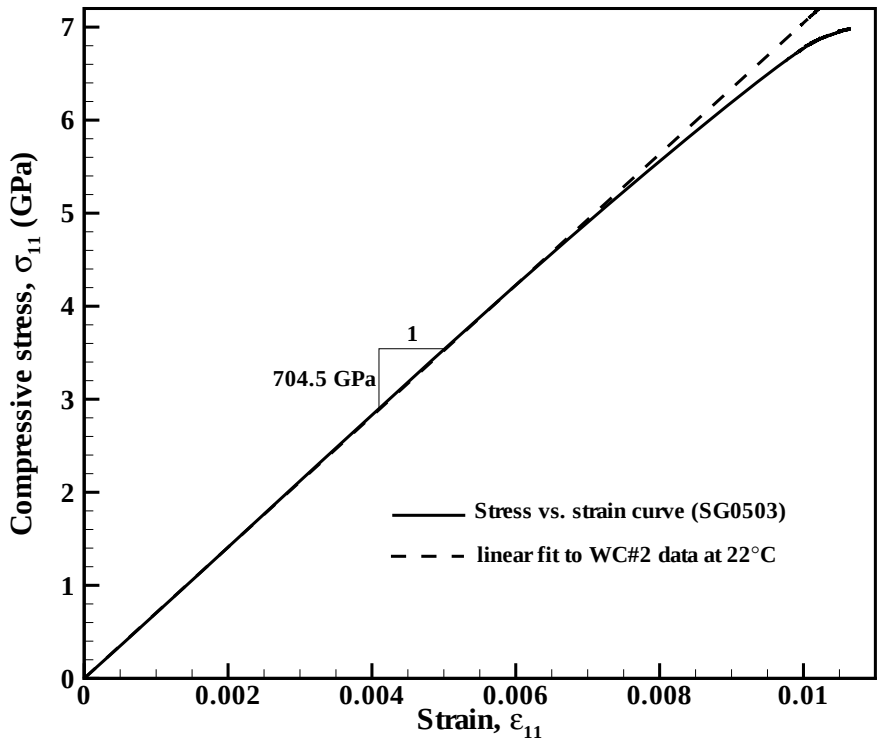

Figure 4.4a: Compressive stress-strain curve for symmetric impact test on WC#2 at 22°C (SG0503)

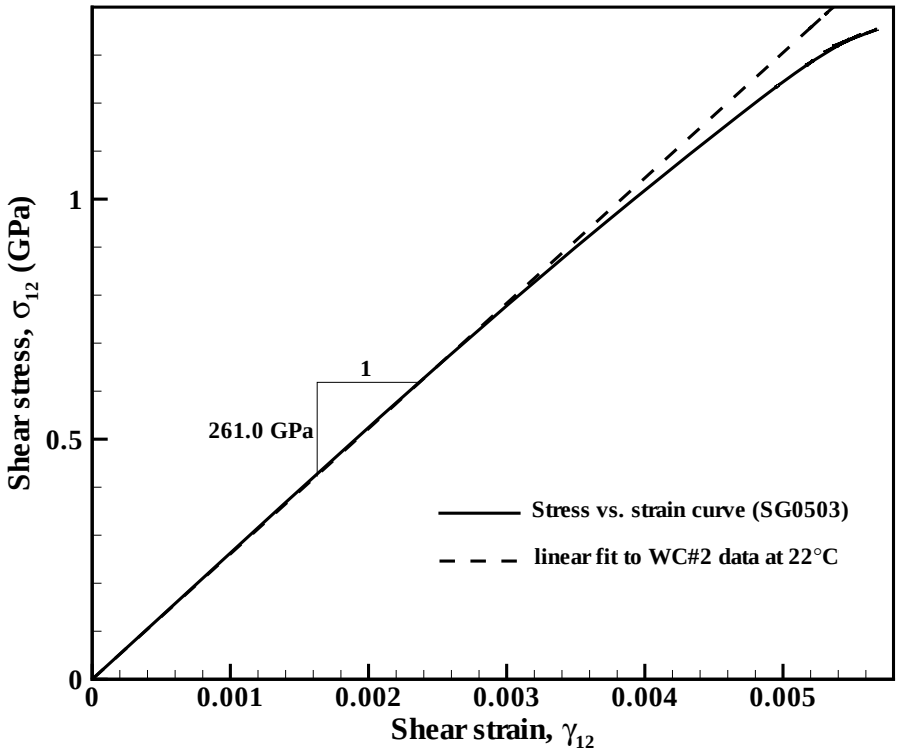

Figures 4.4b: Shear stress-strain curve for symmetric impact test on WC#2 at 22°C (SG0503)

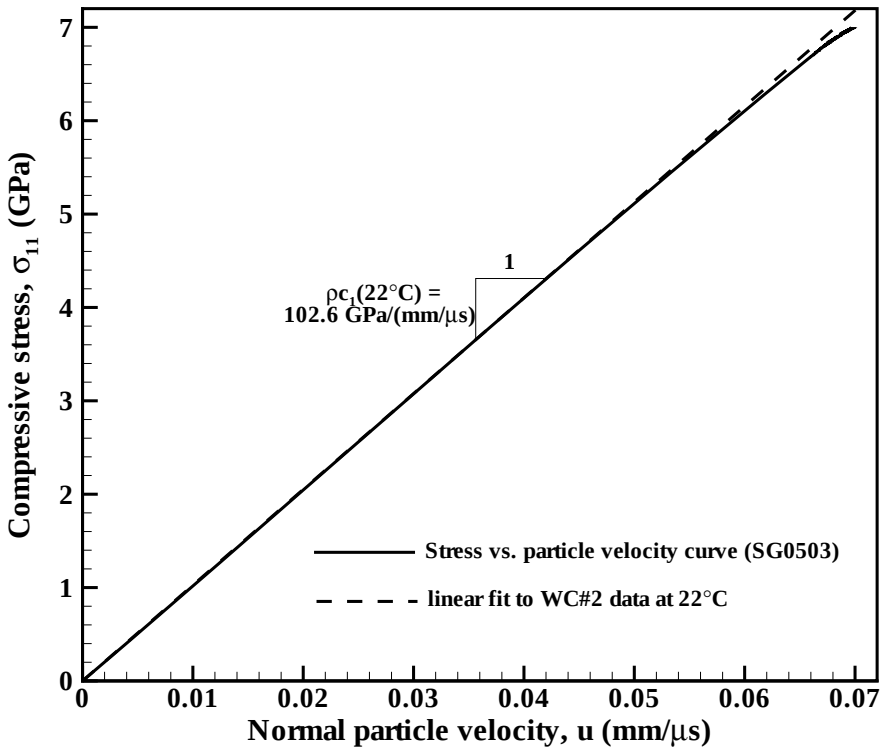

Figure 4.5a: Compressive stress versus normal particle velocity for symmetric impact test on WC#2 at 22°C (SG0503).

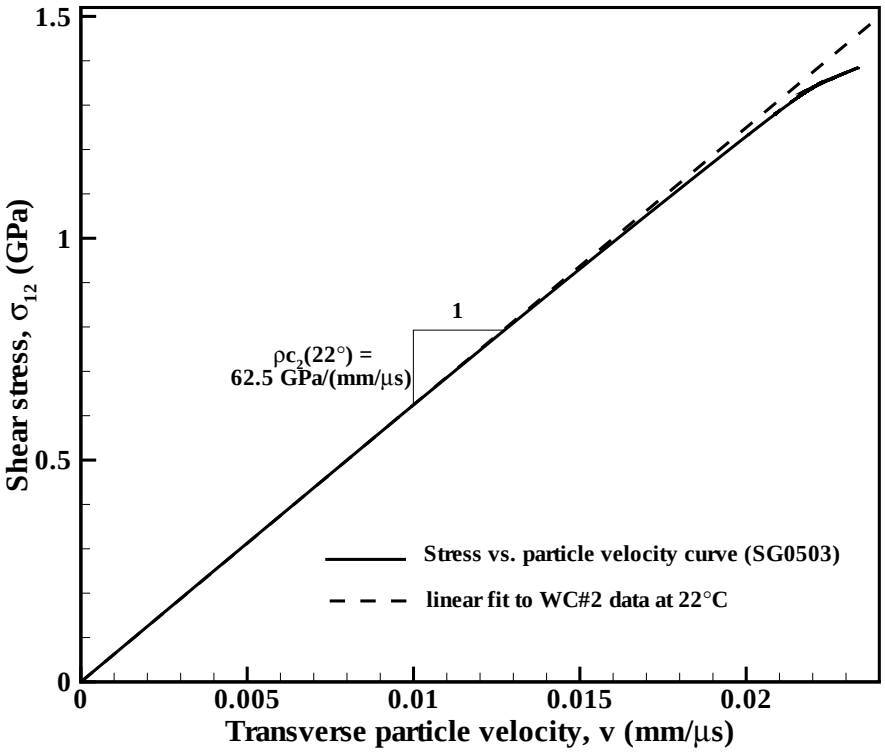

Figure 4.5b: Shear stress versus transverse particle velocity for symmetric impact test on WC#2 at 22°C (SG0503).

Kristopher Frutschy conducted shot KF9607 (Frutschy (1996)) and the normal and transverse free surface velocities measured for that experiment are shown in Figure 4.6. For this shot, the flyer plate was $4\,mm$ thick and the target plate consisted of two $4\,mm$ thick plates. This configuration resulted in the later arrival of the shear wave and a shorter shear window (see Figure 4.6). It is also evident that neither the normal nor transverse velocity rises as sharply as for the room temperature shot (see Figure 4.3).

The dynamic normal and shear stresses for WC#832 at 496°C are calculated using the velocity profiles from Figure 4.6. The compressive stress is plotted versus the normal particle velocity in Figure 4.7a and the shear-stress versus transverse-velocity curve is shown in Figure 4.7b. In these stress-velocity plots, the curves deviate from straight lines more significantly than in the room temperature test (shot SG0503).

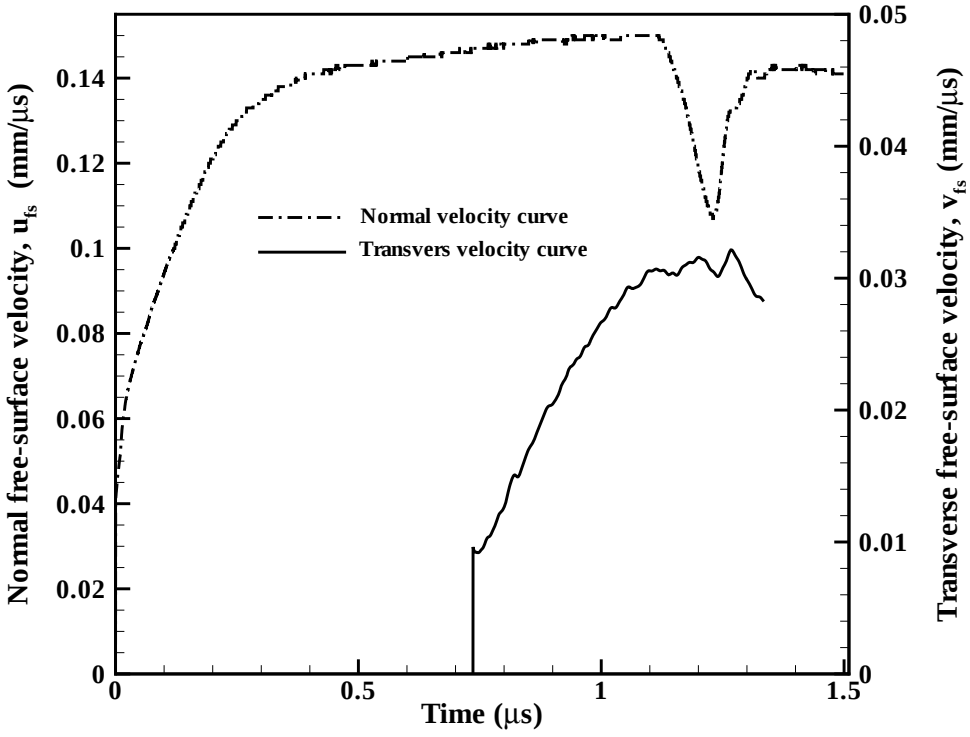

Figure 4.6: Measured normal and transverse free-surface velocities during a symmetric impact test on WC#832 at 496°C (KF9607).

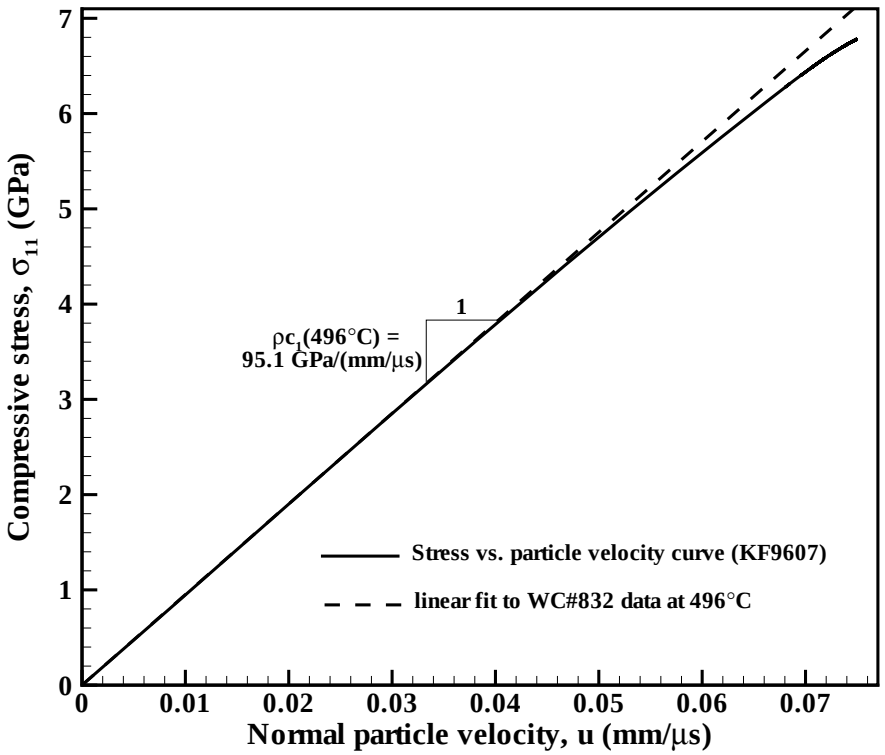

Figure 4.7a: Compressive stress versus normal particle velocity for symmetric impact test on WC#832 at 496°C (KF9607).

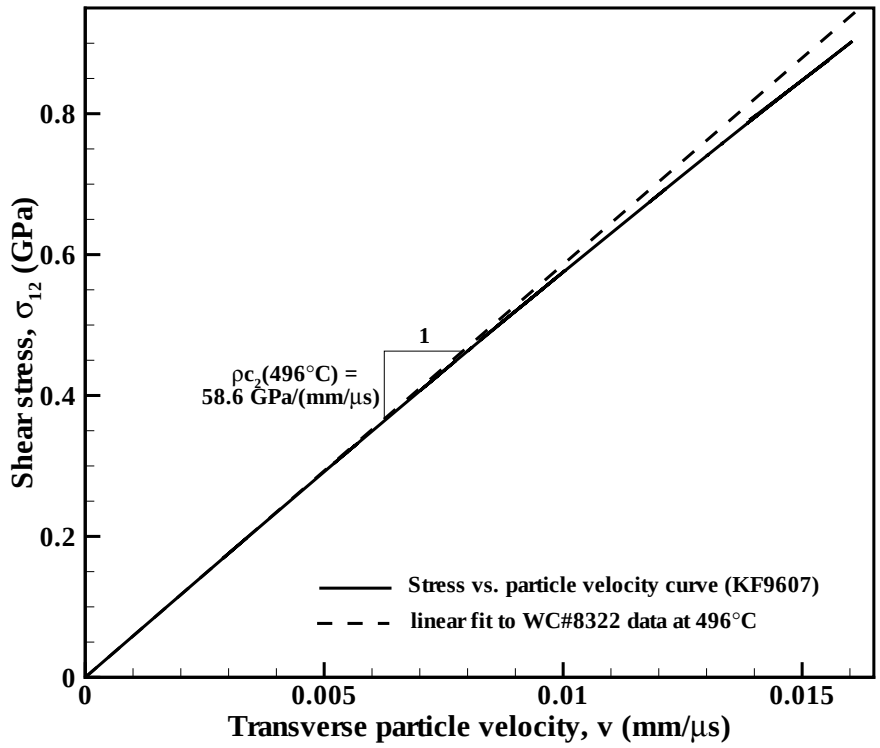

Figure 4.7b: Shear stress versus transverse particle velocity for symmetric impact test on WC#832 at 496°C (KF9607).

The results of shot SG0601 on WC#832 at 643°C are shown in Figures 4.8 – 4.9 and are similar to those for shot KF9607. However, the stress-velocity plots show slightly more deviation from a linear response than for WC#832 at 496°C. This difference is shown more clearly in Figures 4.10a and 4.10b where the stress-velocity responses for shots KF9607 and SG0601 are plotted together. The slope of the dotted lines in Figures 4.10a and 4.10b are, respectively, the stress-free longitudinal and shear acoustic impedances of WC#832 at 22°C.

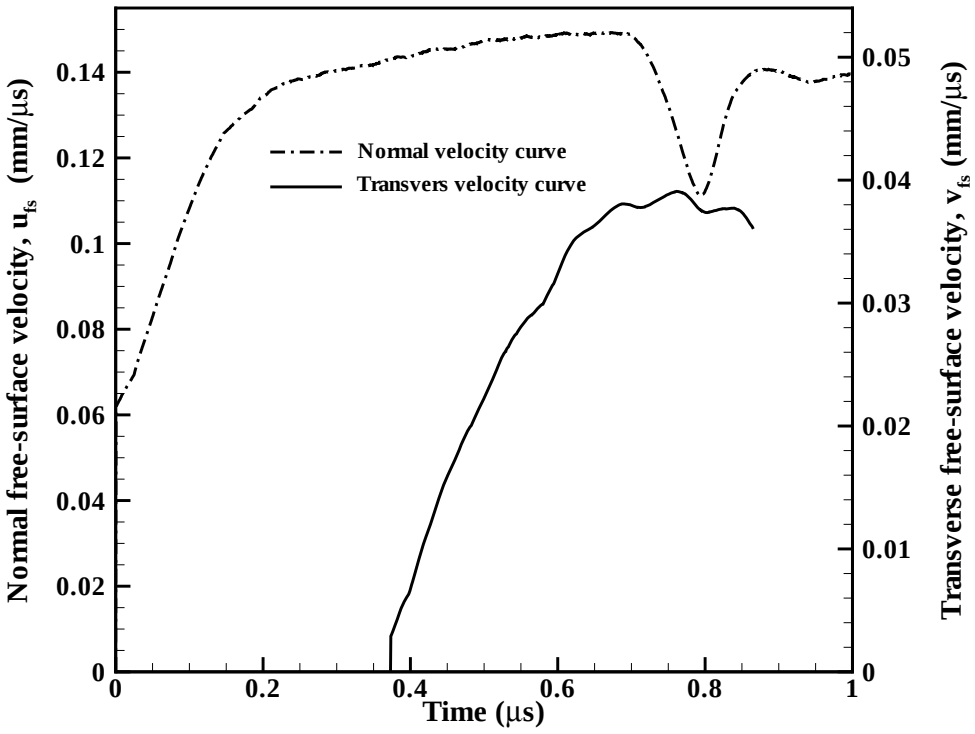

Figure 4.8: Measured normal and transverse free-surface velocities during a symmetric impact test on WC#832 at 643°C (SG0601).

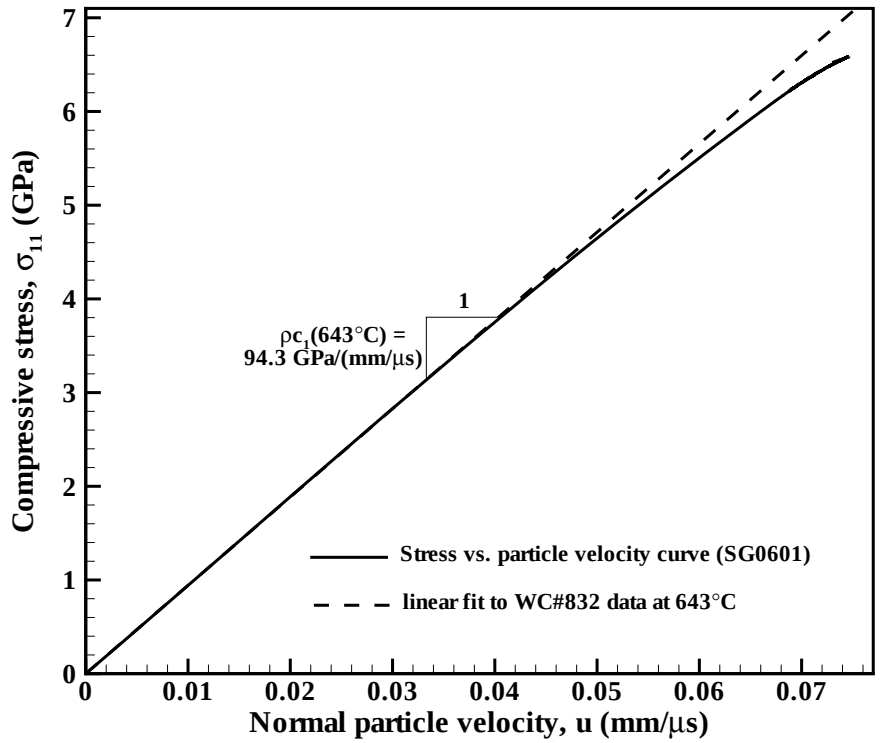

Figure 4.9a : Compressive stress versus normal particle velocity for symmetric impact test on WC#832 at 643°C (SG0601).

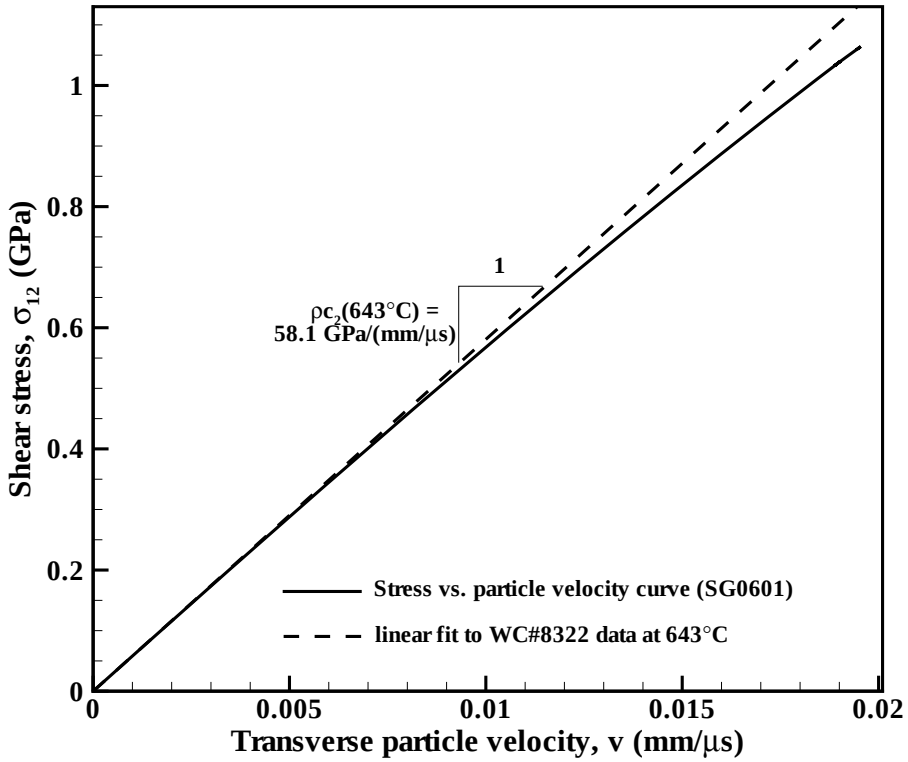

Figure 4.9b: Shear stress versus transverse particle velocity for symmetric impact test on WC#832 at 643°C (SG0601).

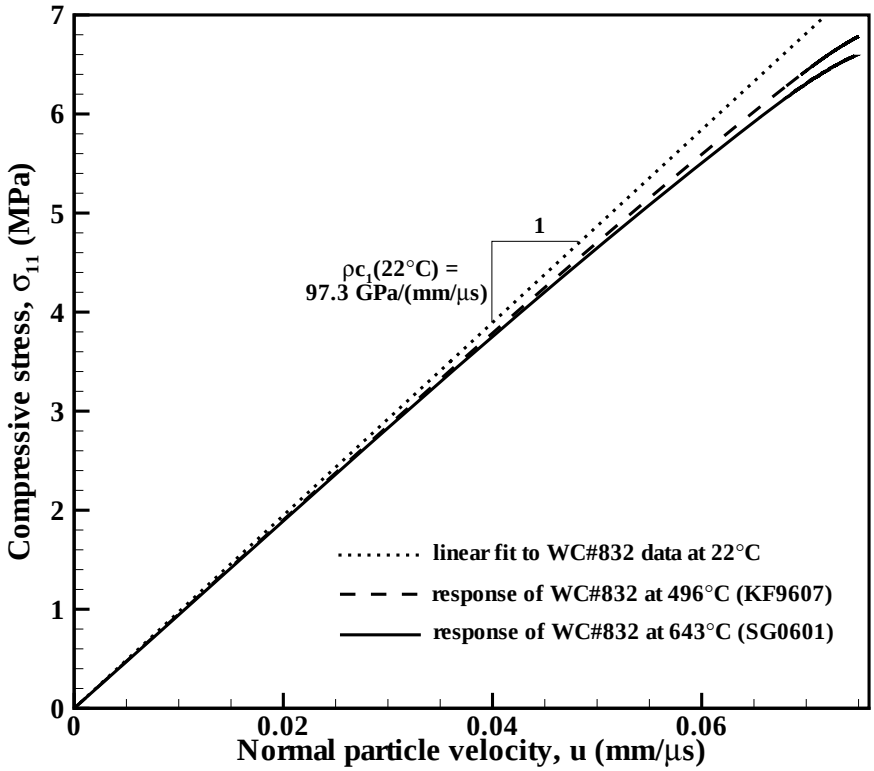

Figure 4.10a: Compressive stress versus normal particle velocity curves for symmetric impact shots on WC#832 at 496°C (KF9607) and 643°C (SG0601).

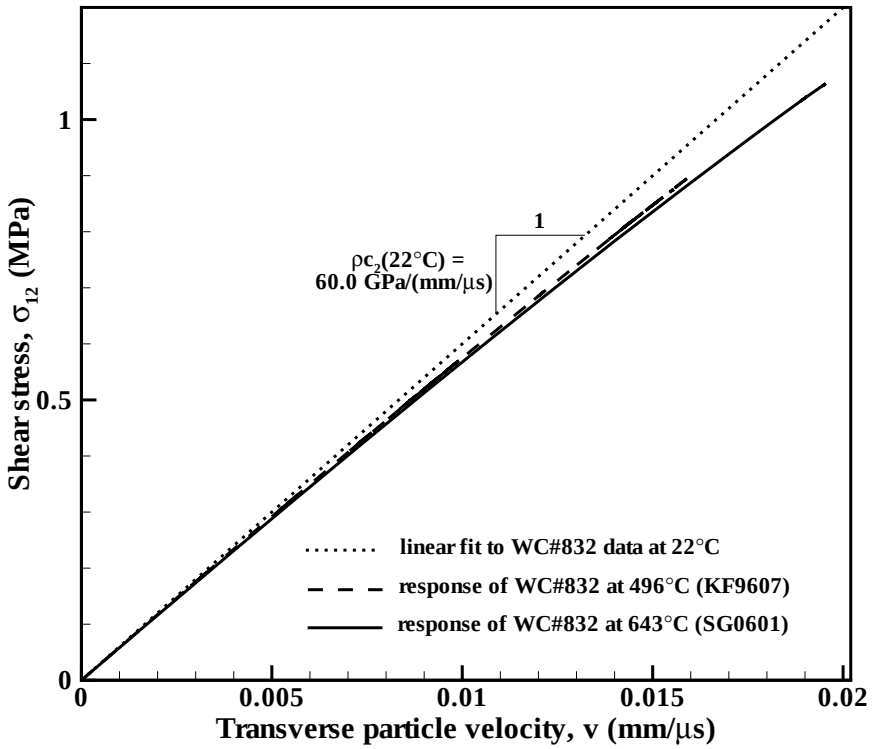

Figure 4.10b: Shear stress versus transverse particle velocity curves for symmetric impact shots on WC#832 at 496°C (KF9607) and 643°C (SG0601).

The maximum shear flow stress measured for the sandwich shots on aluminum at the strain-rates tested are below 250 MPa (Section 4.2). In shot SG0601 it is shown (Figure 4.7b) that the shear response of WC#832 is linear below 250 MPa at 643°C, which exceeds the maximum temperature in the target plates during the high-temperature pressure-shear plate impact experiments on aluminum. This result validates the use of a constant, stress-free shear wave impedance to calculate the shear stress in the sample and the shear strain-rate using the analysis presented in Section 2.1. However, the compressive stresses obtained in the sandwich shots on aluminum exceed the region of linear response in the symmetric impact shots at elevated temperatures. Therefore, in these shots the non-linearity must be taken into consideration when calculating the compressive stress on the sample from the free-surface velocity.

The response of WC#2 at room temperature is linear over the range of stresses tested in the sandwich shot at room temperature (SG0402). Since the compositions and material properties of WC#2 are similar to those of WC#832, the response of WC#832 is also taken to be linear at room temperature.

4.2 High-temperature, high strain-rate response of high-purity aluminum

Five experiments were conducted on high-purity, polycrystalline aluminum at nominally the same strain rates (1.19×10^6 – 1.85×10^6 s^{-1}) and at starting temperatures ranging from room temperature up to 591°C. The shot conditions for these tests are given in Table 4.4.

The goal of these experiments was to measure the shear flow stress in aluminum at high strain rates and at temperatures that approach melt. An important consideration in these experiments is the large increase in the melting temperature of the sample when the sample is subjected to the large pressures of pressure-shear plate impact experiments (Chapter 3). For example, if a sample is heated initially to a temperature of 651°C (924 K), which is 99% of the absolute ambient melting temperature (660°C (933 K)) and the sample is subjected to a large pressure (6 GPa) by the longitudinal wave, then the melting temperature would increase to 1073°C (1346 K) and the sample temperature would increase to approximately 891°C (1164 K). The sample temperature as a percentage of melt is thereby reduced to 86% of the current melting temperature before the shear wave arrives at the sample.

Therefore, to study material response at larger fractions of the melting temperature, it is advantageous to conduct tests at lower pressures. In pressure-shear plate impact experiments, lower pressures can be achieved by reducing the projectile velocity and/or increasing the impact angle θ. However, if the impact angle is too great, there will be undesirable slipping at the impact surface. Decreasing the impact velocity will decrease both the normal and shear pulses. The ideal situation would be to reduce the normal stress without affecting the shear loading. This favorable loading condition can be achieved by using a pressure-release wave configuration, as discussed in Section 2.1 (see Figure 2.3). If the sample is bonded strongly to the surrounding target plates, then unloading longitudinal waves can be used to reduce the pressure and allow the shearing resistance to be measured at near zero pressure and consequently at or near the ambient melting temperature.

In preliminary heating tests, an aluminum sample was sandwiched between two tungsten carbide (with 6% cobalt) plates and heated to desired temperatures. When the target assembly is heated to a temperature of approximately 600°C and held for as little as one hour, the aluminum was observed to form a strong bond with the target plates. This heating provides the bond necessary for a successful pressure-release type experiment. However, when the sample was held at temperatures above 650°C for approximately one hour it was revealed through X-ray diffraction (XRD) analysis that the compound aluminum tungsten (WAl_{12} and/or Al_5W) had formed at the interface. Therefore it is necessary to conduct the experiments at lower starting temperatures and to perform XRD analysis on the sample to confirm the composition of the material tested.

Shot SG0702 was conducted at a starting temperature of 645°C. For this particular test, the induction heater failed after the sample was heated to 630°C. Two months later, after the induction heater had been repaired, the sample was heated to 645°C and held for just over two hours before impact. The shear flow stress measured for this experiment (~ 320 MPa) was notably higher than that for aluminum at any temperature tested (230 MPa). The sample was originally 10 μm thick 99.0% pure aluminum and the post-shot XRD analysis showed that a large fraction if not the entire sample was now aluminum tungsten. This analysis revealed that the sample tested was aluminum tungsten and not aluminum, which is consistent with the large shearing resistance recorded for this experiment. This finding is significant because the response of the softest material in the target assembly is measured during these experiments. Therefore, on tests where there are small amounts of aluminum tungsten present at the

interface between the aluminum sample and the target plates, it is the response of the softer aluminum that will be measured.

In order to ensure that the sample remains purely aluminum, the subsequent starting temperatures were kept below 600°C. Despite the presence of an apparently strong bond between the target plates and the aluminum sample, a sudden drop in shearing resistance coinciding with the drop in pressure would raise questions about the adequacy of the aluminum/tungsten carbide bond. Such a result could indicate a debonding at the interface between the aluminum and the bounding target plates and not a change in the shearing resistance of the sample. Fortunately, as will be shown in Section 4.2.1b, no drop in shear resistance is observed at the time of the pressure drop for the pressure-release experiment.

4.2.1 Shot results for sandwich tests on aluminum

4.2.1a Response of 99.999% pure aluminum at room temperature

Shot SG0402 was conducted at room temperature on a 99.999% pure, $25\,\mu m$ thick aluminum sample. The normal and transverse free-surface velocities measured for this shot are shown in Figure 4.11. Time is measured from the time at which the longitudinal wave arrives at the rear surface. The shear wave arrives at the rear surface $0.500\,\mu s$ after the longitudinal wave. The dip in the normal velocity at $1.124\,\mu s$ corresponds to the end of the compressive loading pulse when the longitudinal unloading wave reflected from the rear surface of the flyer plate reaches the rear surface of the target. If the reflected unloading longitudinal wave, which is much larger than the shear pulse in magnitude, is inclined when it reaches the rear surface, it can alter the transverse

velocity causing the record after that point to be unreliable. The arrival time of this unloading wave at the rear surface is marked by a black dot on the transverse velocity curve in Figure 4.13. However, since there is no break in the transverse velocity versus time curve at this time, it appears that there is no significant tilt-induced anomaly that would preclude the direct interpretation of the transverse velocity record until unloading occurs at approximately 1.4 μs .

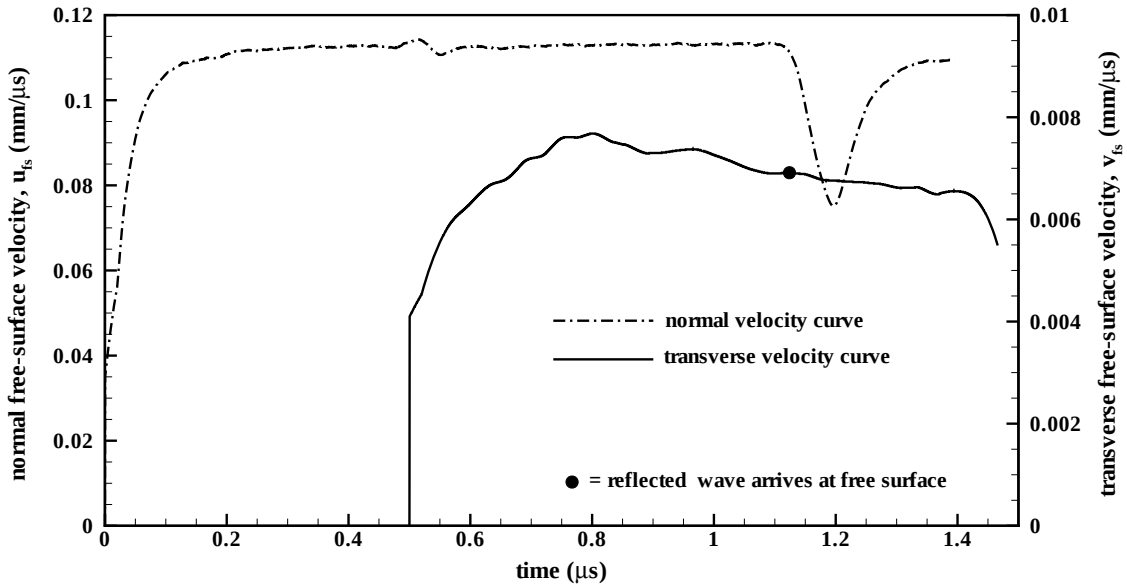

Figure 4.11: Normal and transverse free-surface velocities for shot SG0402. The first longitudinal wave arrives at the free surface at time zero.

The response of the tungsten carbide target plates is taken to be linear at room temperature (see Section 4.1). Therefore, the initial, stress-free values for the acoustic impedances of WC#832 at room temperature are used to calculate the compressive and shear stress versus time profiles shown in Figure 4.12. The shear strain rate obtained using Equation (2.23) is plotted in Figure 4.13. The strain rate values are only valid after the sample reaches a uniform state of stress, which is approximately 35 *ns* (according to simulations) after the shear wave arrives at the sample.

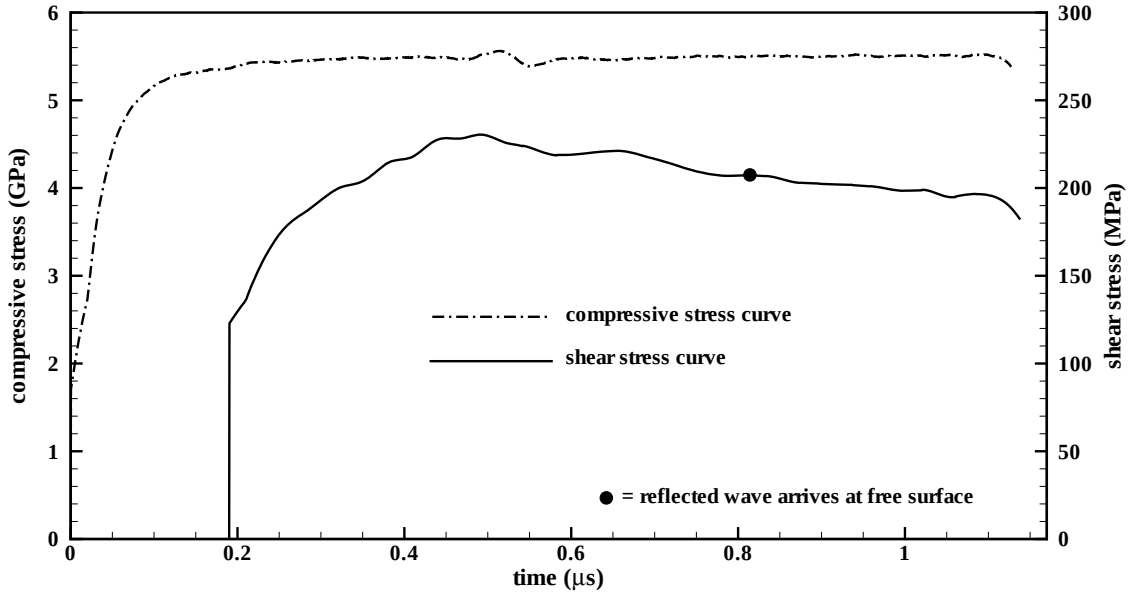

Figure 4.12: Compressive and shear stresses for aluminum at room temperature (shot SG0402). The first longitudinal wave arrives at the sample at time zero.

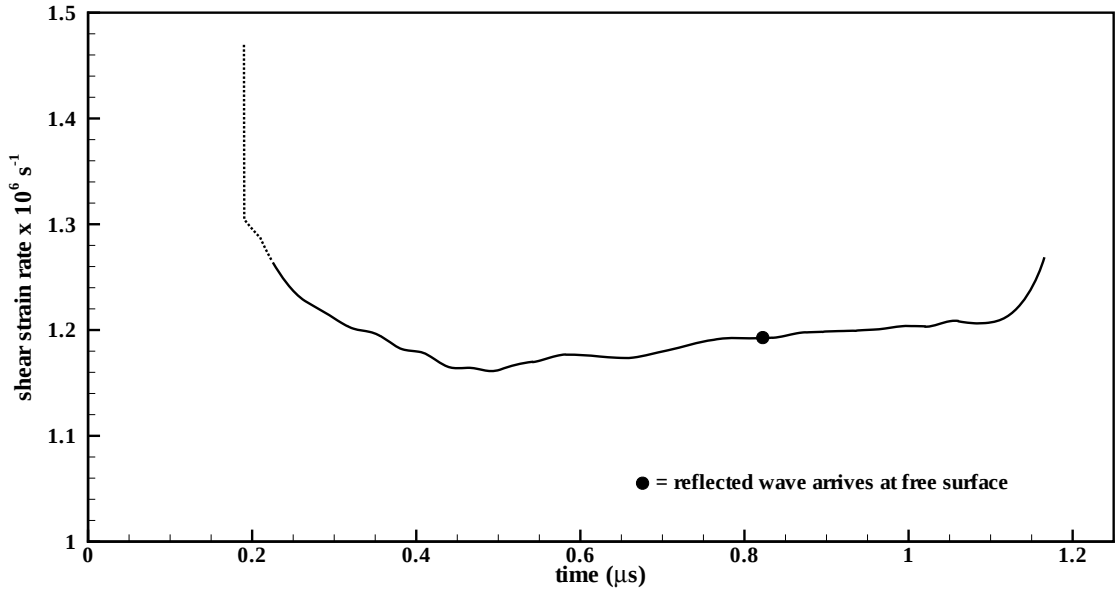

Figure 4.13: Shear strain rate from shot SG0402.

4.2.1b Response of 99.999% pure aluminum at elevated temperatures

Three shots were conducted at elevated temperatures on 99.999% pure, 25 μm thick aluminum samples. Shot SG0504 was conducted at a starting temperature of 495°C. For the other elevated temperature tests, the two thermocouple readings from the

edge of the sample were averaged and used to find the temperature at the center of the sample using the full-body finite element analysis outlined in Section 3.2. For shot SG0504, thermocouple #2 had a minor short in the line which caused the temperature readout to be artificially low. Therefore the 'average' value was taken to be the value from the one thermocouple that was functioning correctly. The flyer material used for shot SG0504 was WC#832.

Shot SG0703 was conducted at a starting temperature of 584°C and was designed to be a pressure-release experiment. The flyer for this shot was made of two WC#112 plates and the intention was for the compressive wave to pass through the interface between those two plates without reflecting back a significant unloading wave. However, a small gap at the interface between the two flyer plates produced an unloading wave which reached the sample just after the unloading wave reflected from the rear surface of the target and consequently subjected the sample to a tensile load. Due to this tensile load, the sample either debonded from the target plates or fractured and the shearing response could not be measured after that point. The test did, however, measure successfully the shearing resistance of aluminum at pressure.

Shot SG0802 was a pressure-release, pressure-shear plate impact experiment that was conducted at a starting temperature of 582°C. For this test, the flyer was one solid plate of pure tungsten carbide that was thick enough for no waves to be reflected back from the flyer plate before the test had concluded.

The normal free-surface velocities for these three elevated temperature tests are plotted versus time in Figure 4.14. The dip in velocity in shot SG0504 at time 1.111 μs

corresponds to the end of the compressive loading pulse. This dip is similar to the unloading observed in shot SG0402. Shot SG0703 shows a sharp increase in normal velocity at 1.115 μs followed by quick dip. In this shot, the release wave reflected off the rear surface of the target reaches the sample and begins to unload it (corresponding to the increase in normal velocity) before an unloading wave reflected from the interface at the middle of the flyer reaches the sample. (Recall that the flyer for this shot was made of two WC#112 plates.) The sharp decrease in normal velocity that follows corresponds to the sample separating from the target plates (or fracturing) when both of those unloading waves arrive at the sample and subject it to a tensile load.

The normal velocity for SG0802 shows a sharp increase at 1.116 μs followed by a gradual decrease. This normal velocity profile is expected for a pressure-release experiment where the release wave reflected off the rear surface of the target returns to the sample and unloads it.

It was shown in Section 4.1.2 that the compressive response of the tungsten carbide is not quite linear at the particle velocities measured in these experiments for these testing temperatures (the particle velocities are equal to one-half of the free-surface velocities). The compressive responses of WC#832 shown in Figure 4.10a for tests at 496°C and 643°C can be interpolated to find the response of the WC#832 at the testing temperatures used for these sandwich shots. Those responses are used to calculate the compressive stresses that are reported in Figure 4.15.

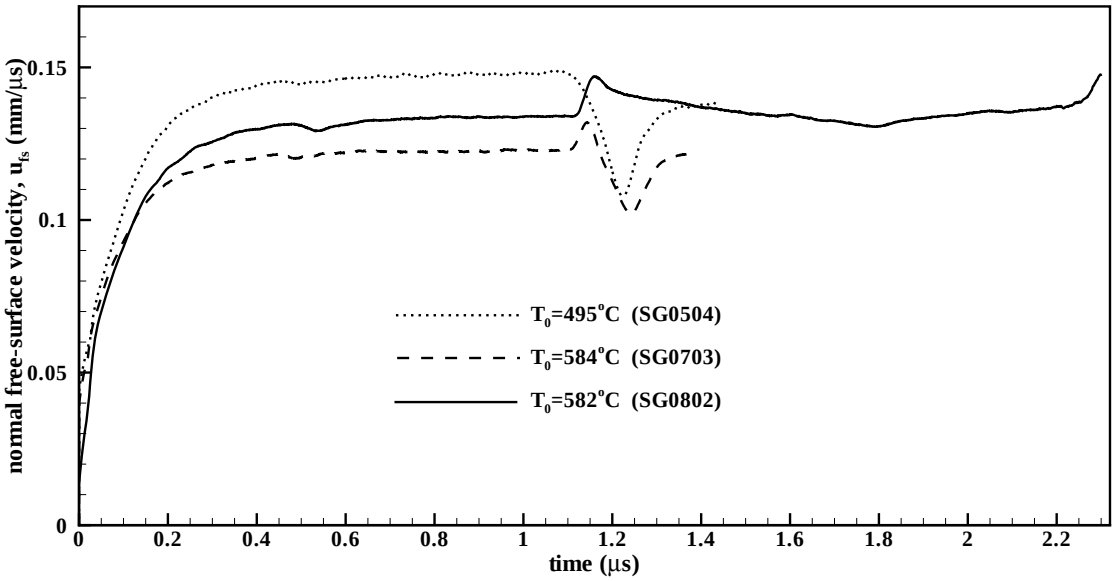

Figure 4.14: Normal free-surface velocities from three elevated temperature shots on 99.999% pure aluminum (SG0504, SG0703, SG0802).

After the time 1.116 μs in shot SG0802, a different characteristic analysis is used to calculate the compressive stress drop. The free-surface velocities after the first unloading wave arrives at the rear surface, $u_{fs}(t)$, are subtracted from the free-surface velocities from a time at the rear surface $\frac{2h_{RP}}{c_1}$ earlier, where h_{RP} is the rear target plate thickness and c_1 is the stress-free longitudinal wave speed of WC#832 at 582°C. That velocity difference is multiplied by the stress-free longitudinal acoustic impedance of WC#832 at 582°C and divided by two to yield the compressive stress in the sample at a time $\frac{h_{RP}}{c_1}$ earlier:

$$\sigma\left(t-\frac{h_{RP}}{c_1}\right)=\left[u_{fs}\left(t-\frac{2h_{RP}}{c_1}\right)-u_{fs}(t)\right]\frac{\rho_0 c_1}{2}. \tag{4.19}$$

For this analysis, t is taken to be the time after the unloading wave first arrives at the rear surface of the target.

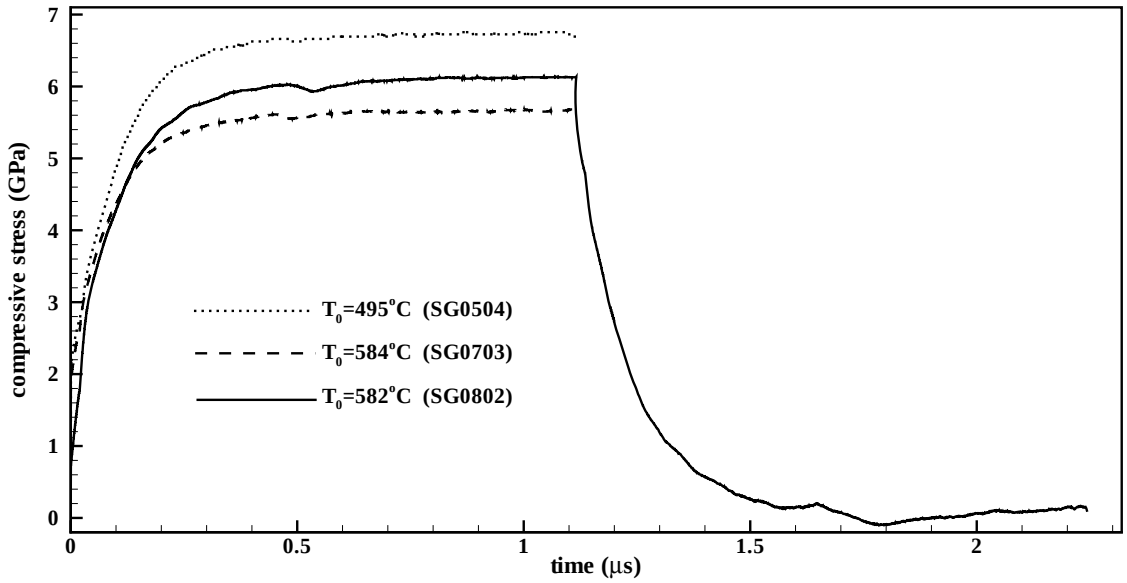

Figure 4.15: Compressive stress vs. time for three elevated temperature tests on 99.999% pure aluminum (SG0504, SG0703, SG0802). Time zero is the arrival time of the first longitudinal wave at the sample.

The transverse free-surface velocities are plotted in Figure 4.16 for the three elevated temperature shots on 99.999% pure aluminum. The black dots on the curves in Figure 4.16 indicate the time at which a reflected longitudinal wave reaches the free surface. Again, if the reflected longitudinal wave is inclined, it can alter the transverse velocity causing the record after that point to be unreliable. For shot SG0504 – as in shot SG0402 – the second longitudinal wave to reach the free surface is the wave that has reflected off the rear surface of the flyer. In shots SG0703 and SG0802, the first longitudinal wave to reach the free surface reflects back towards the sample and is reflected back again at the sample/rear target plate interface. This wave returns to the free surface before the unloading wave from the flyer. For shots SG0504 and SG0802, there is no noticeable break in the transverse velocity record at the time when a reflected wave returns to the rear surface (marked by the black dot). However, for shot SG0703, the transverse velocity shows a slight increase when the reflected wave arrives at the rear

surface. It is possible that this break in the transverse velocity was induced by an inclined reflected wave and that the rest of the transverse velocity record of shot SG073 does not correspond to the shear response of the sample.

As noted in Section 4.1.2, the response of the tungsten carbide target plates in shear, even at these elevated temperatures, can be taken to be linear and the shear stresses in the sample are calculated accordingly. The curves of shear stress versus time are plotted in Figure 4.17. The star on shot SG0802 represents the time of the pressure drop at the sample. The shear strain rates are reported in Figure 4.18. Once again, the strain rate values are only valid after the shear stress is uniform across the sample.

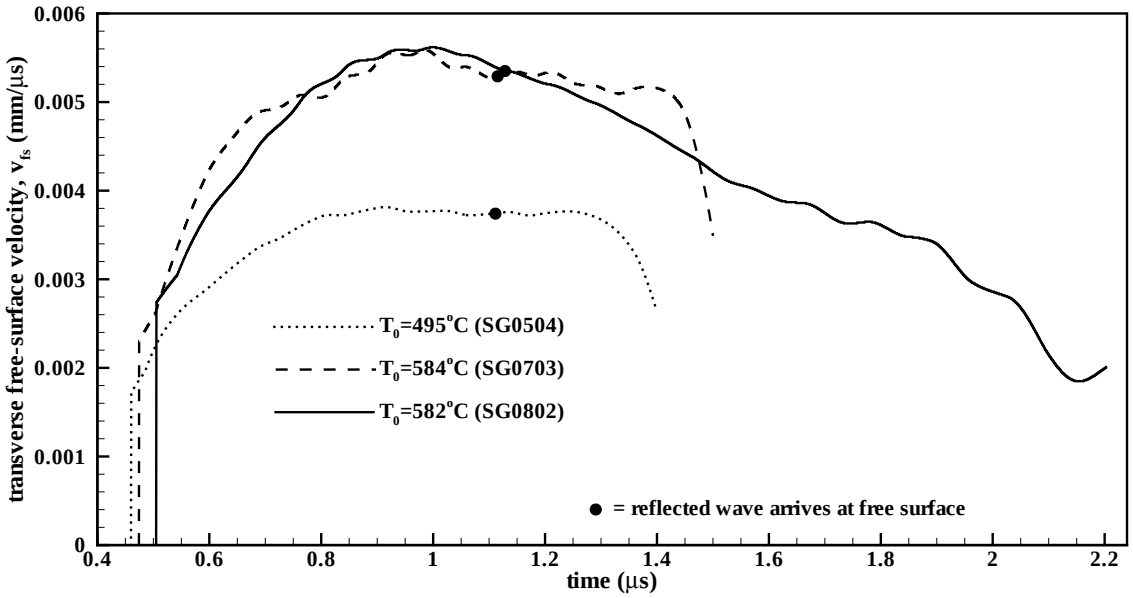

Figure 4.16: Transverse free-surface velocities from three elevated tests on 99.999% pure aluminum (SG0504, SG0703, SG0802). Time zero is the arrival of the first longitudinal wave at the free surface.

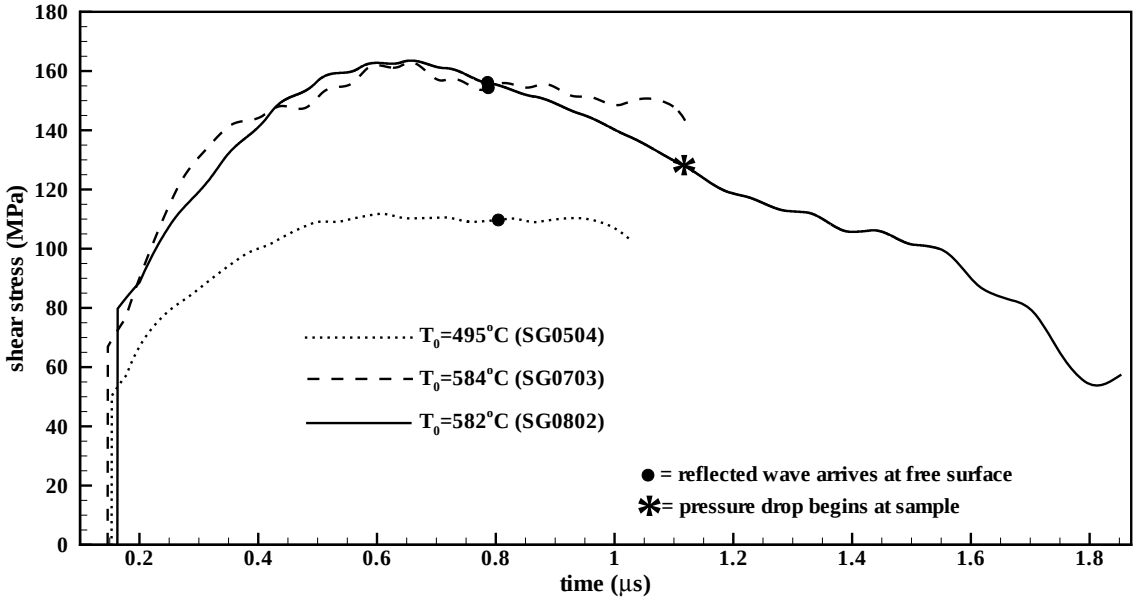

Figure 4.17: Shear stress vs. time curves for three elevated tests on 99.999% pure aluminum. Time zero is the time of the arrival of the first longitudinal wave at the sample.

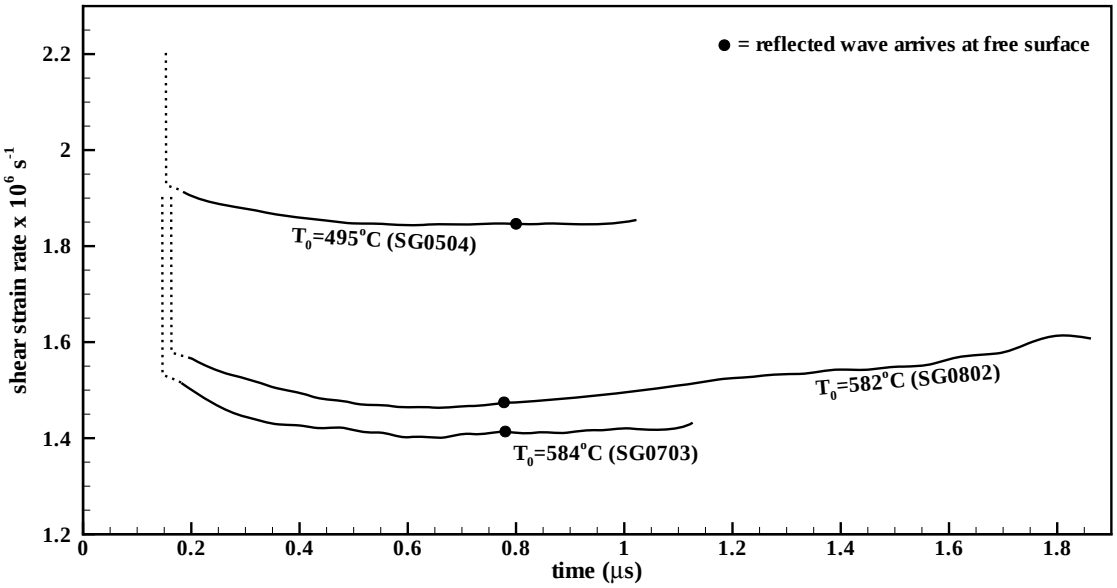

Figure 4.18: Shear strain rate from three shots on 99.999% pure aluminum at elevated temperatures (SG0504, SG0703, SG0802). The arrival of the first longitudinal wave at the sample is taken to be time zero.

4.2.1c Response of 99.0% pure aluminum at 591°C

One shot was conducted on a 99.0% pure, 10 μm thick aluminum sample at a starting temperature of 591°C (shot SG0602). This test utilized a significantly lower impact velocity in order to have a lower pressure on the sample during the shear loading. A lower impact velocity necessitated the use of a thinner sample to keep the strain rate nominally the same as the other tests (see Equation 2.23). The flyer material used for this shot was WC#112. The normal and transverse free-surface velocities for this test are shown in Figure 4.19. The dip in the normal velocity at 1.149 μs corresponds to the end of the compressive loading pulse when the unloading wave reflected from the rear surface of the flyer plate reaches the rear surface.

At this low impact velocity (52.9 *m/s*), the target plates respond linearly in both compression and shear. The compressive and shear stress versus time curves are shown in Figure 4.20. The shear strain rate is shown in Figure 4.21.

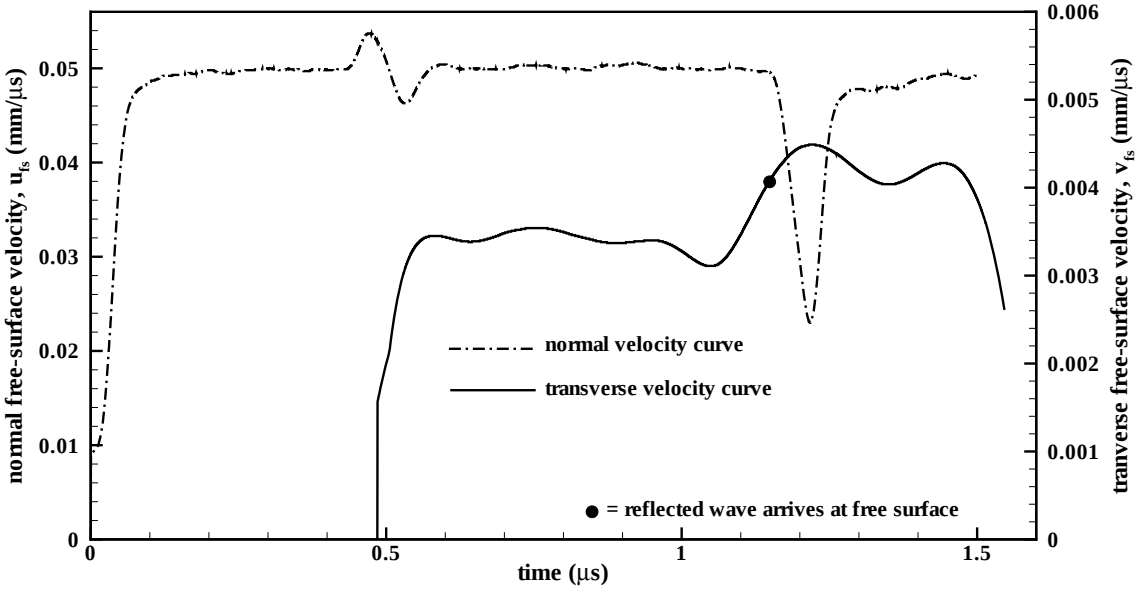

Figure 4.19: Normal and transverse free-surface velocities for shot SG0602. Time zero is the arrival of the first longitudinal wave at the free surface.

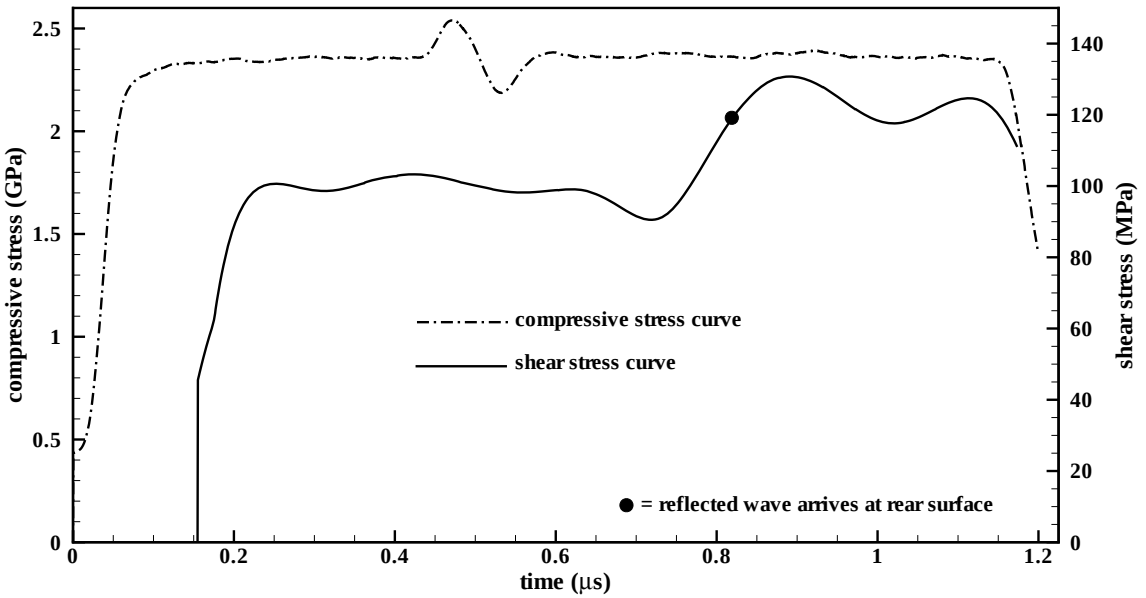

Figure 4.20: Compressive and shear stresses in the aluminum sample for shot SG0602. Time zero is the time of the arrival of the first longitudinal wave at the sample.

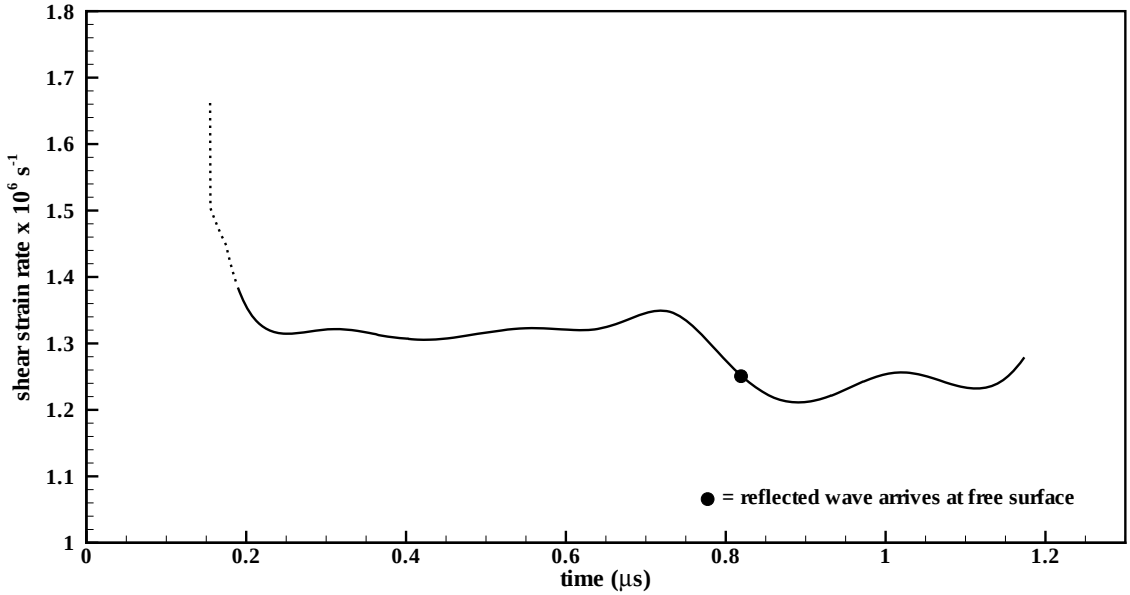

Figure 4.21: Shear strain rate from shot SG0602. Time zero is the time of the arrival of the first longitudinal wave at the sample.

4.2.2 Sample temperature predictions

A program was written in Matlab to take the starting temperatures, compressive stresses, shear stresses and shear strains found experimentally and approximate the instantaneous temperature in the sample during the test. The program uses a fourth order Runge-Kutta method to integrate the temperature-change equation derived in Chapter 3 (Equation (3.16)). These sample temperature predictions assume that the process is adiabatic. The pressure, P, in Equation (3.16) is estimated to be equal to the compressive stress, i.e.

$$P \approx -\sigma_{11} . \tag{4.20}$$

The finite difference simulations of the pressure-shear plate impact experiment, discussed in Section 5.2, show this approximation to be quite accurate. The final sample temperatures, predicted using the adiabatic approximation, are reported in Table 4.4 along with the final sample temperatures as a percentage of the melting temperature at the current pressure.

The sample temperature, melting temperature, and the sample temperature as a percentage of the melting temperature are shown in Figures 4.22 and 4.23 for shots SG0703 and SG0802 respectively. When the longitudinal waves arrive at the sample (at time zero), the sample temperature and melting temperature begin to rise for both tests. After approximately 0.16 μs , the shear wave arrives and begins to plastically deform the sample. The sample temperature increases during shear loading while the melting temperature stays nearly constant. For shot SG0703 (Figure 4.22), the sample temperature reaches a final temperature of 830°C (1103 K), which is 83.0% of the melting temperature at the current pressure (5.73 GPa). Before the pressure drop, shot

SG0802 reaches a sample temperature of 861°C (1134 K), which corresponds to 83.8% of the melting temperature at the current pressure (6.13 GPa). The sample temperature and melting temperature then both drop as the pressure decreases (at 1.12 μs). After the pressure drop, the sample temperature begins to approach the melting temperature and reaches a final temperature of 645°C (918 K), which is 98.9% of the melting temperature at the current pressure (-0.06 GPa). The predicted sample temperature, melting temperature and sample temperature as a percentage of the melting temperature are plotted for shots SG0402, SG0504 and SG0602 in Figures 4.24, 4.25, and 4.26, respectively.

Again, it should be noted that sample predictions made in this section assume adiabatic conditions, which imply that the duration of the test is too short for significant heat diffusion to occur. In Section 5.4, simulations of these experiments are performed under non-adiabatic conditions and heat conduction is shown to have an effect on the sample temperature. Therefore, the adiabatic sample predictions made in this section should be considered as providing an upper bound to the actual temperature in the sample during the tests. The extent of the effect of heat conduction on the final sample temperature is discussed in more detail in Section 5.4. From that analysis a more accurate final sample temperature range can be predicted (Table 4.4).

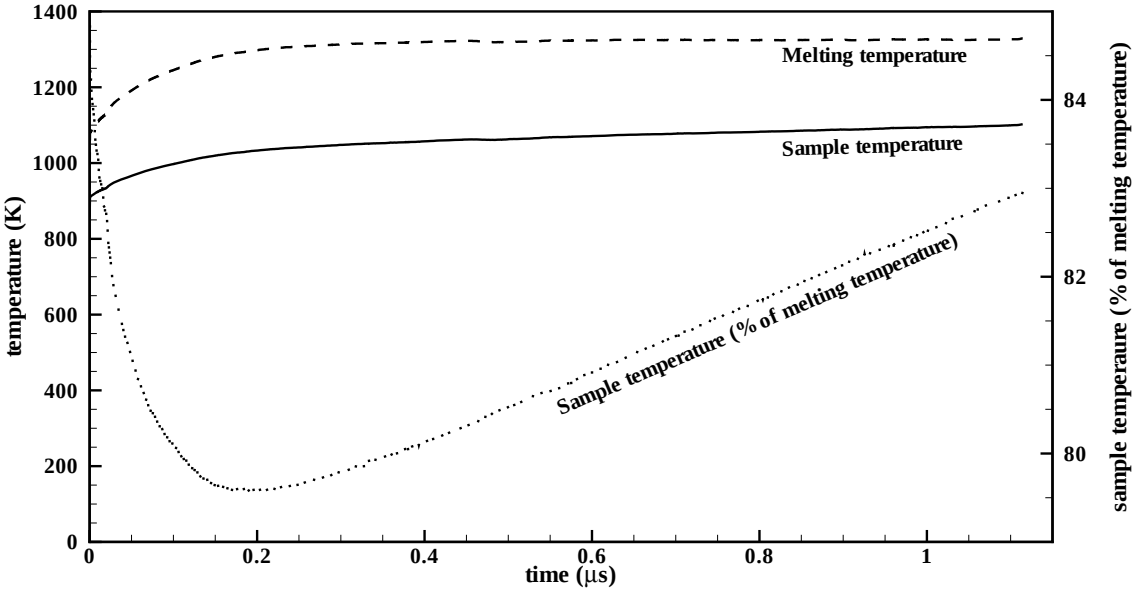

Figure 4.22: Adiabatically predicted sample temperature for shot SG0703.

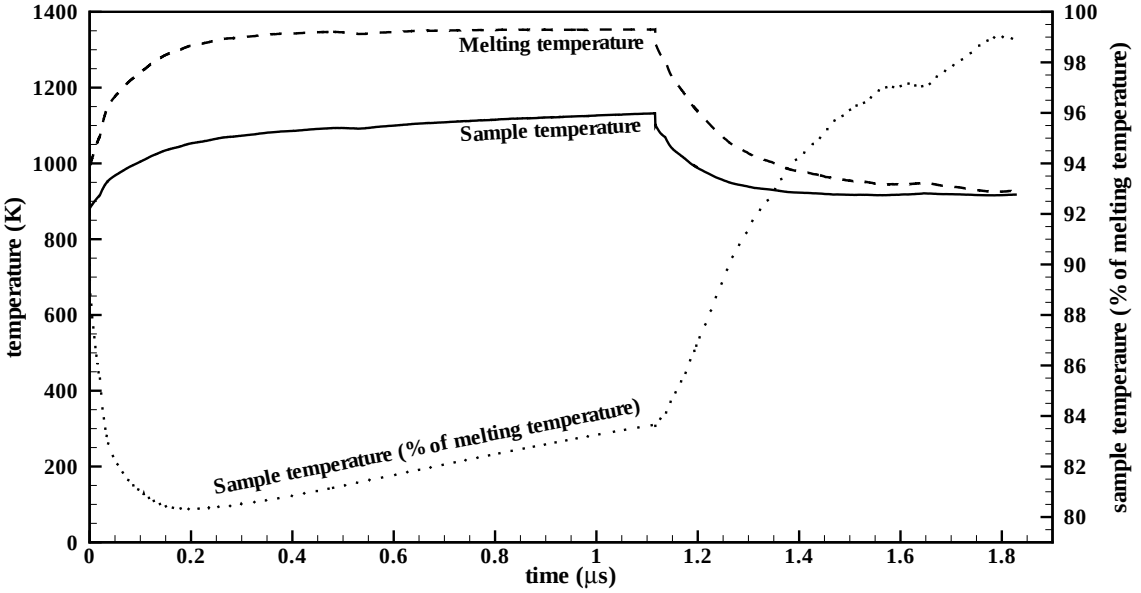

Figure 4.23: Adiabatically predicted sample temperature for shot SG0802.

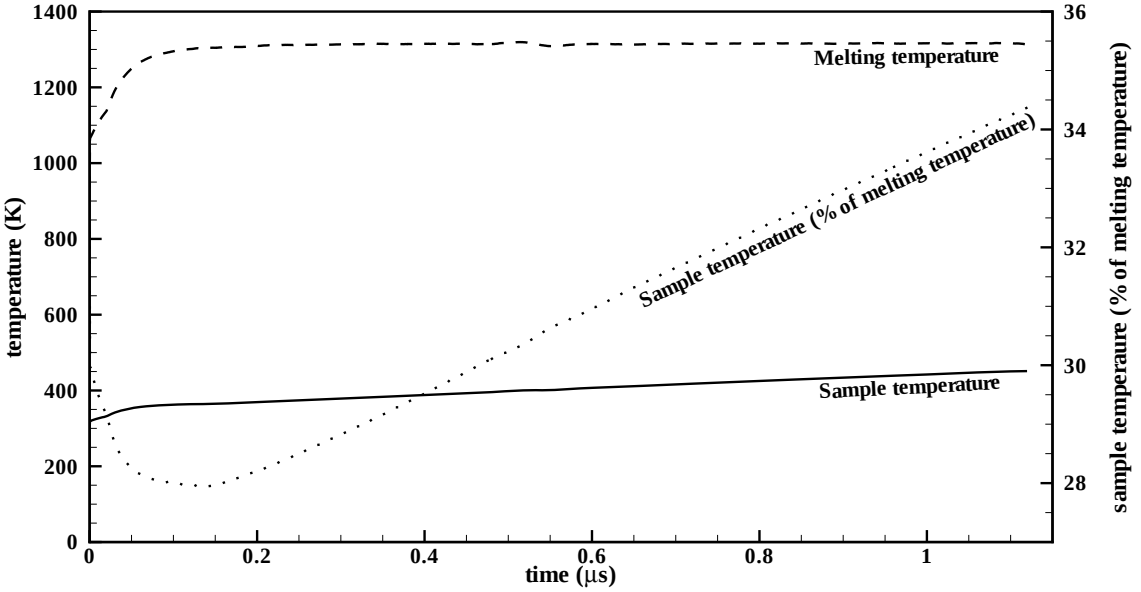

Figure 4.24: Adiabatically predicted sample temperature for shot SG0402.

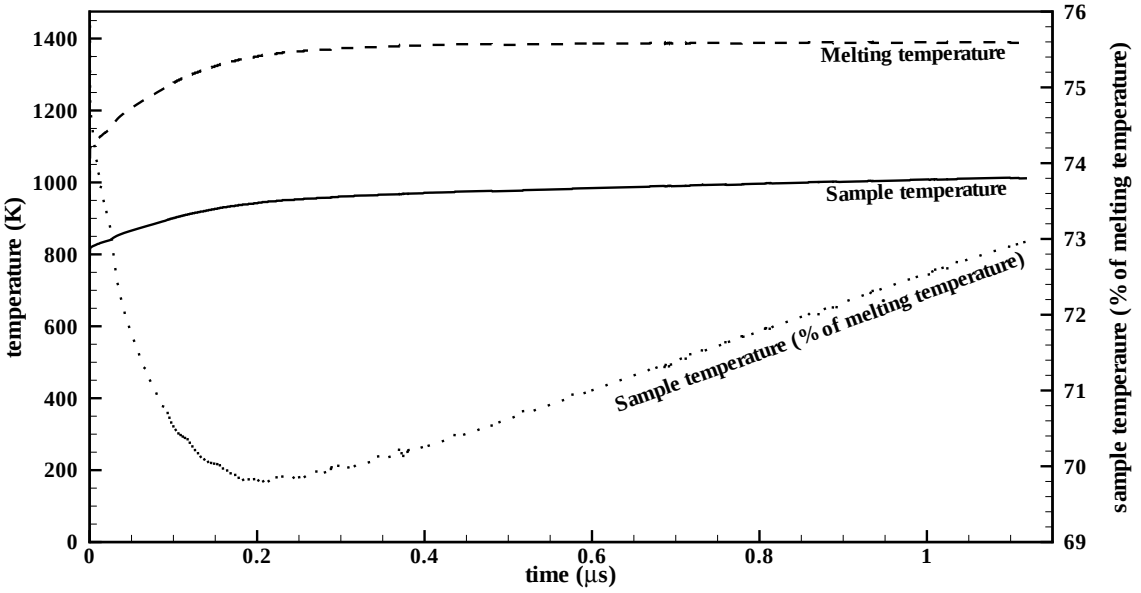

Figure 4.25: Adiabatically predicted sample temperature for shot SG0504.

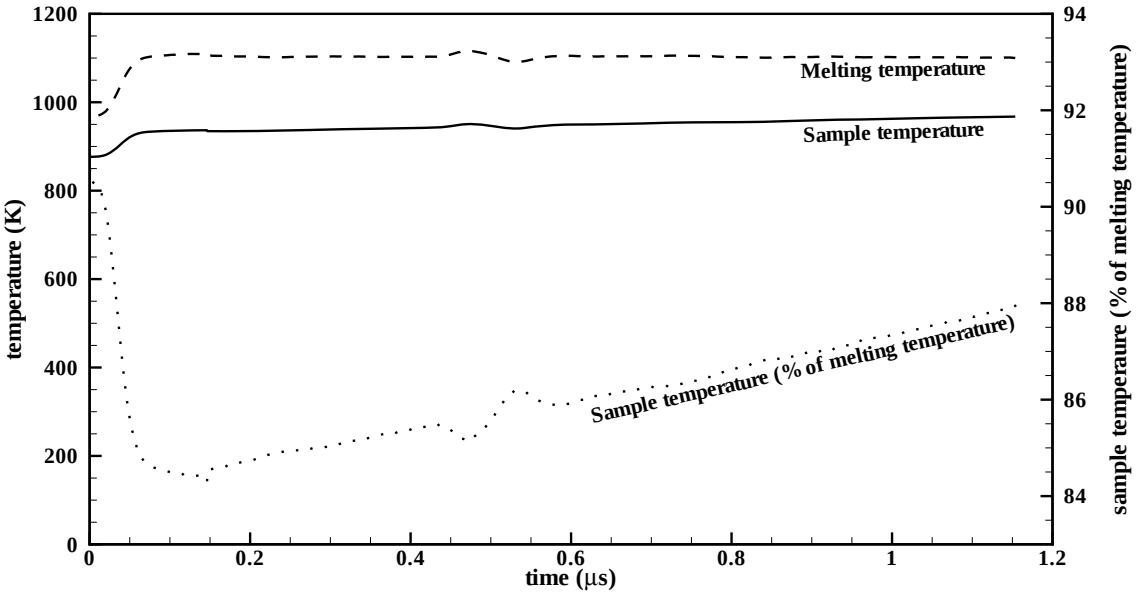

Figure 4.26: Adiabatically predicted sample temperature for shot SG0602.

4.2.3 Metallography

All of the 99.999% pure aluminum test samples originated from the same 25 μm roll of rolled aluminum foil purchased from Alfa Aesar (stock #44233). For 99.999% pure aluminum, the foil "self-anneals" at room temperature. The material properties for pure aluminum are given in Table 4.5. The complete composition for the 99.999% pure aluminum stock is given in Table 4.6. Undeformed samples were polished and etched using a chemical etchant (150 *mL* distilled water, 30 *mL* hydrochloric acid, 10 *mL* nitric acid, and 10 *mL* hydrofluoric acid) in order to find the average grain size. An optical image taken as a top view of the sample is given in Figure 4.27. Grain sizes on the surface are found to be approximately 2-5 μm in diameter.

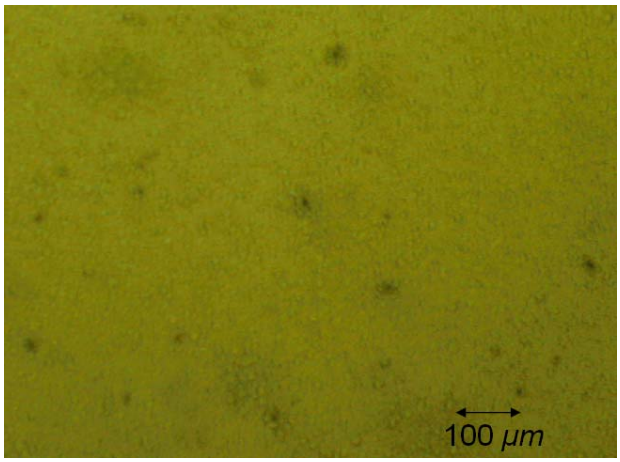

Figure 4.27: Undeformed aluminum sample, top view.

As mentioned at beginning of Section 4.2, several preliminary heating tests were conducted where the samples were heated but not impacted. For one such test, the sample was heated up to 600°C and held for one hour and forty minutes. Figure 4.28 is an optical image taken of the sample after heating and before any polishing or etching. The grains have grown significantly in size to diameters of approximately 80-150 μm.

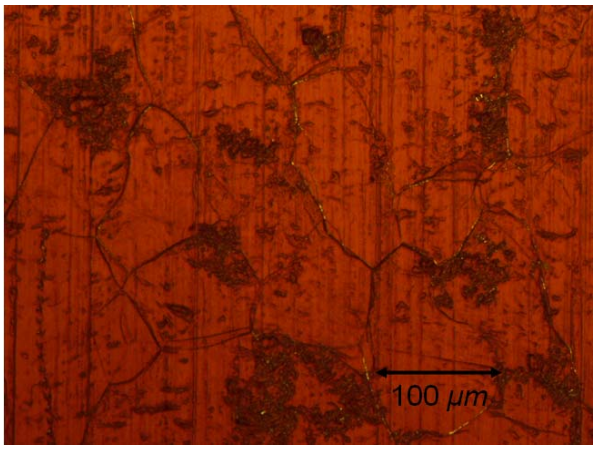

Figure 4.28: Undeformed sample after one hour and forty minutes at 600°C, top view.

Grain growth can be calculated using the annealing equation (Feltham and Copley (1958)):

$$D_f^2 - D_0^2 = Kt \exp\left(\frac{-\Delta H}{RT}\right) \tag{4.21}$$

where D_f is the instantaneous grain size, D_0 is the initial grain size, K is a material constant, t is time, ΔH is the activation energy for grain boundary self-diffusion, R is the gas constant, and T is temperature. The material constant K for aluminum is given by Lundy and Murdock (1962) as K=1.71 cm^2/sec. The activation energy for grain boundary self-diffusion for aluminum has been reported by several authors (Lundy and Murdock (1962), Federighi (1959), DeSorbo and Turnbull (1959), and Nowak (1976)) to be between 27,000 *cal/mole* and 35,725 *cal/mole*. If an activation energy of 30,500 *cal/mole* is chosen, then the annealing equation predicts the 150 μm grain size observed in the heating test. Using ΔH = 30,500 *cal/mole*, the final grain sizes for every shot prior to impact are estimated and listed in Table 4.4.

In plate impact experiments, the target assembly is damaged significantly during deceleration. Due to the brittle nature of the tungsten carbide plates, the target shatters into hundreds of small pieces making post-analysis difficult. However, a shard of tungsten carbide, with the aluminum sample still bonded to it, was recovered and used to find the grain size of the deformed aluminum sample after a high temperature test (shot SG0703). For this test, the sample was heated up to 584^{o}C and held for two hours and ten minutes prior to impact. Figure 4.29 is an optical image of the deformed aluminum sample for shot SG0703. The sample area was found near the edge of the target. Of the few grains that can be observed, the sizes appear to be approximately 100 μm in

diameter. The grain size was estimated to be approximately 149 μm just prior to impact using the annealing equation. It appears that either the grain size prediction was not accurate or the size of the grains decreases during the experiments possibly through dynamic recrystallization.

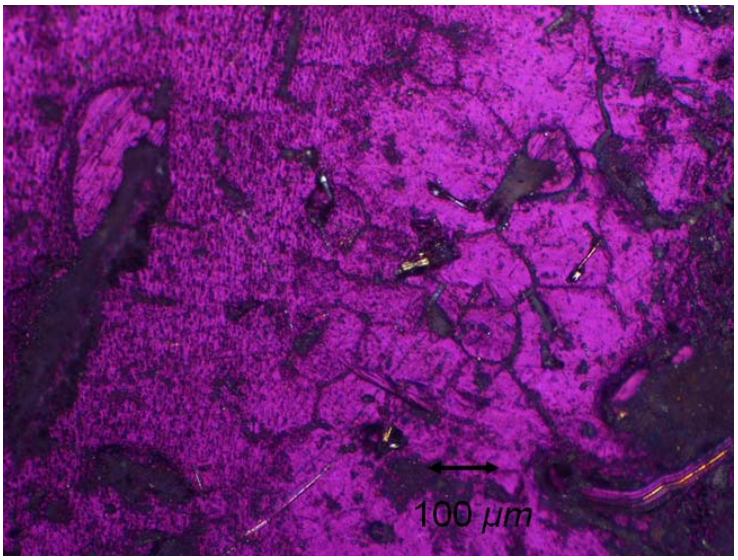

Figure 4.29: Deformed sample from elevated temperature test (SG0703).

4.2.4 Discussion

Figure 4.30 shows the dynamic shear-stress versus shear-strain curves for all five tests performed on polycrystalline aluminum. As predicted by models based on rate-controlling processes involving the thermally activated motion of dislocations, the shear flow stresses for the tests at elevated temperatures are significantly lower than the flow stresses obtained at room temperature (shot SG0402). However, the shearing resistance does not decrease monotonically with increasing temperature. This result is evidenced by shots SG703 and SG0802, which were tested at a higher temperature than shot SG0504, yet displayed a higher shear resistance.

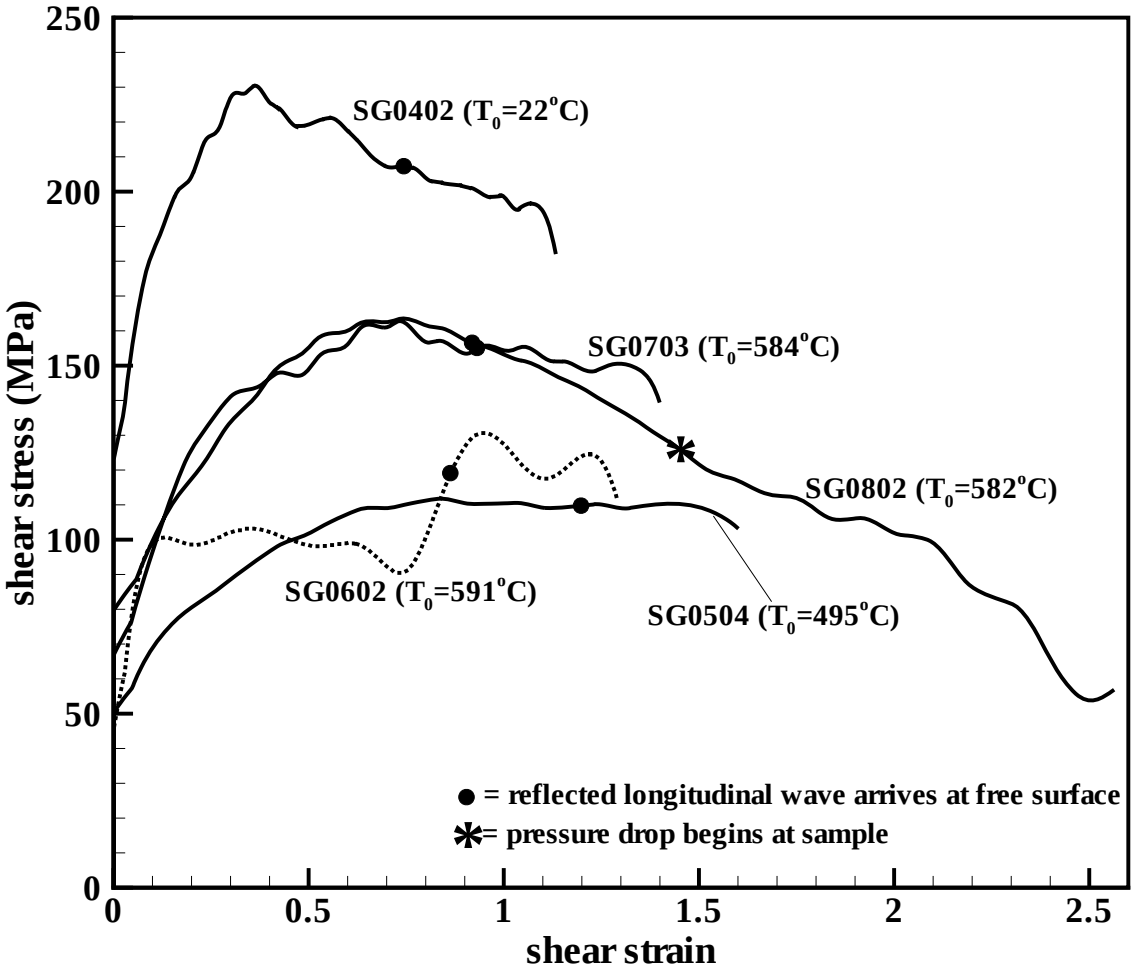

Figure 4.30: Shear stress vs. shear strain curves for shots on polycrystalline aluminum. SG0602 was a 99.0% pure aluminum sample (dotted curve). All other samples were 99.999% pure aluminum.

The room temperature test on aluminum (SG0402) displays a relatively sharp rise in shear stress up to a peak value of 230 MPa at a strain approximately 0.37 before softening. The shear resistance observed in shot SG0402, at a strain rate of 1.2×10^6 s^{-1}, is in good agreement with the strain rate sensitivity curve fitted to previously reported results on high-purity, polycrystalline aluminum tested at room temperature (see Figure 4.31). Also, the degree of softening shown in shot SG0402 is similar to that observed in a test performed by Klopp et al. (1985) at a strain rate of 4×10^6 s^{-1} on commercially pure aluminum.

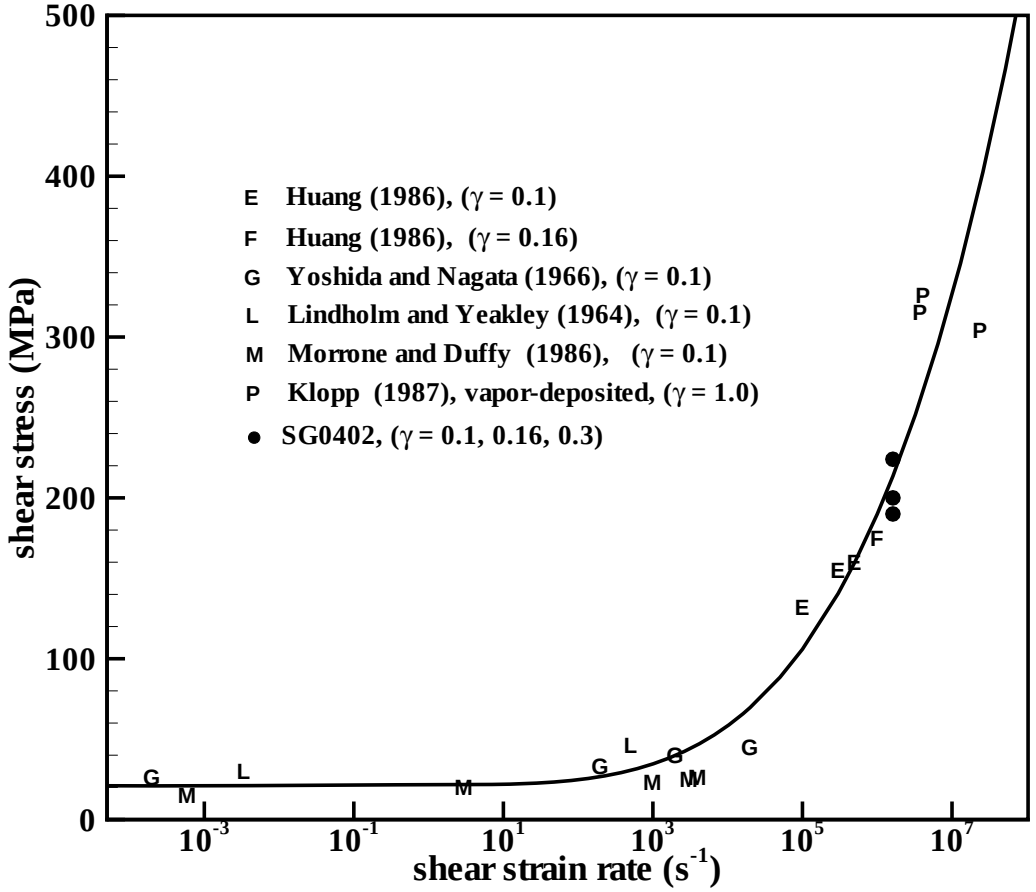

Figure 4.31: Strain rate sensitivity of high-purity, polycrystalline aluminum at room temperature.

Shots SG0703 (T_0=584°C) and SG0802 (T_0=582°C), which have similar testing and loading conditions until the pressure drop occurs in shot SG0802, exhibit similar responses while under pressure. Both shear-stress versus shear-strain curves rise gradually to a peak shear stress of 163 MPa at a shear strain of approximately 0.75 before softening begins. Thus, there appears to be good repeatability in the high-temperature, pressure-shear plate impact experiments.

A gradual increase in shear flow stress, up to a plateau of only 112 MPa, is observed in shot SG0504 (T_0=495°C). This test was conducted at a slightly higher strain

rate than all of the other tests on 99.999% pure aluminum (see Table 4.4) and typically, as observed in Figure 4.31, the shear flow stress increases with increasing strain rate. Despite this, the shear response of this test is lower than that of the tests at higher temperatures (SG0703 and SG0802) and the test at room temperature (SG0402). This test displays very little softening.

The shear-stress versus shear-strain curve for the test on 99.0% pure aluminum (shot SG0602) displays a unique structure. The shear stress rises to a plateau of approximately 100 MPa and stays mostly constant up to a shear strain of approximately 0.6 before dipping slightly and then rising quickly to a shear stress of 130 MPa. Due to the difference in purity, direct comparisons to the other results are not appropriate.

As discussed in Section 4.2.3, the sample tested at room temperature had a smaller average grain size than the samples in the elevated temperature tests. This difference may explain the relatively quick rise and sharp peak observed in the room temperature shear response and the slower rise and wider peaks for the elevated tests.

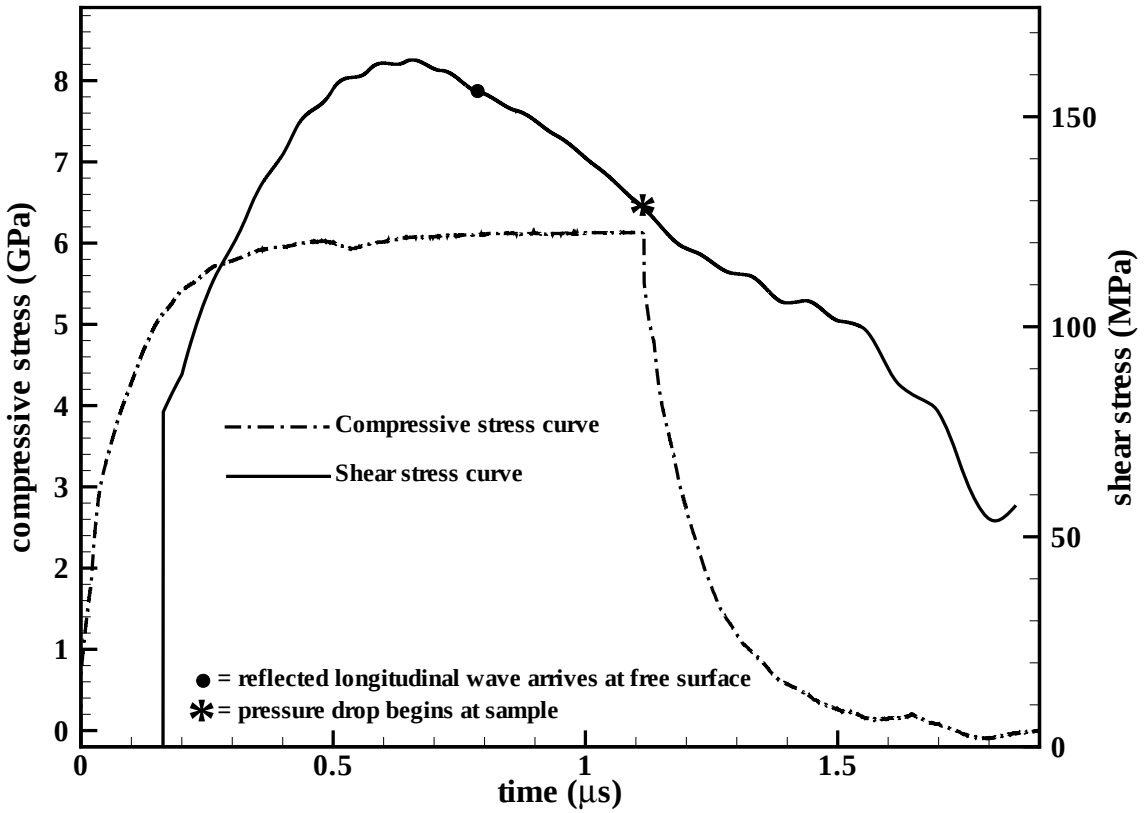

Figure 4.32: Compressive and shear stresses from shot SG0802 plotted against time at the sample. Time zero is the arrival of the first longitudinal wave at the sample.

The compressive and shear stresses for shot SG0802 are plotted versus time, at the sample, in Figure 4.32. At the time of the pressure drop (1.12 μs) the shear stress is 127 MPa and decreasing steadily. After the pressure drop the shear stress continues to fall as at the same rate until 1.19 μs. At that time, at a compressive stress of approximately 2.9 GPa, the shear stress begins to decrease less quickly. Then, the shear stress begins to fall more quickly again at 1.56 μs. At a time of approximately 1.75 μs, the sample goes into tension. The maximum tension observed is 90 MPa. The shear response appears smooth after the pressure drop and it is presumed that the aluminum stays bonded to the target plates and that there is no fracture in the sample.

When the pressure drops, there is a jump in temperature (see Equation (3.16)). This temperature jump can be viewed as either a decrease in absolute sample temperature or an increase in absolute temperature as a fraction of the melting temperature at the current pressure (see Figure 4.23). In either case, the continuous response of the shear stress suggests that a temperature jump does not have a direct effect on the flow stress, but may influence the subsequent flow stress through a change in hardening rate.

Chapter 4 Tables

Table 4.1. Compositions of tungsten carbide plates.

	WC#2	WC#112	WC#832	Pure WC
% Tungsten Carbide	93.28	86.9	85.13	100
% Tantalum Carbide	0.3	0.5	6	-
% Titanium Carbide	0.12	0.3	2.5	-
% Niobiom Carbide	-	-	0.07	-
% Cobalt	6.3	12.3	6.3	-

Table 4.2. Room temperature properties of tungsten carbide plates

Property (at 22°C)	WC#2	WC#112	WC#832	Pure WC
$c_1\left(mm/\mu s\right)$	6.88	6.69	6.88	6.85
$c_2\left(mm/\mu s\right)$	4.19	4.05	4.24	4.3
$\rho \quad \left(kg/m^3\right)$	14910	14255	14150	15400
$\rho c_1\left(GPa/\left(mm/\mu s\right)\right)$	102.58	95.37	97.35	107
$\rho c_2\left(GPa/\left(mm/\mu s\right)\right)$	62.47	57.73	60	67.1
Young's modulus, $E\left(GPa\right)$	631	656.6	607.4	609.1
Shear modulus, $\mu\ \left(GPa\right)$	261.8	233.7	254.4	287
Possion's ratio, υ	0.205	0.21	0.194	0.2
k (W/*m*K)	100	100	100	102
Cp (J/kgK)	200	200	200	204
α_v (K^{-1} x 10^{-6})	9.0	9.0	9.0	17.7

Table 4.3. Shot parameters for symmetric impact tests.

Parameters	SG0503	KF9607	SG0601
Target material	WC#2	WC#832	WC#832
Target thickness, (*mm*)	4.02	8	4.03
T_0, (°C)	22	496	643
$c_1\left(T_0\right),\left(mm/\mu s\right)$	6.88	6.77	6.72
$c_2\left(T_0\right),\left(mm/\mu s\right)$	4.19	4.17	4.14
$\rho\left(T_0\right),\ \left(kg/m^3\right)$	14910	14050	14019
$\rho c_1\left(T_0\right),\ \left(GPa/\left(mm/\mu s\right)\right)$	102.58	95.1	94.25
$\rho c_2\left(T_0\right),\ \left(GPa/\left(mm/\mu s\right)\right)$	62.47	58.61	58.09
Impact velocity, V_0 (*m/s*)	148.9	155	158
Impact angle, θ (°)	18	16	18
Tilt angle, α (°)	0.73	0.57	0.23
Closure angle, Ω (°)	44.75	90	16
Flyer material	WC#2	WC#832	WC#112
Flyer thickness, (*mm*)	4.054	4	2.41
$\rho c_1\left(22°C\right),\ \left(GPa/\left(mm/\mu s\right)\right)$	102.58	97.35	95.17
$\rho c_2\left(22°C\right),\ \left(GPa/\left(mm/\mu s\right)\right)$	62.47	60	57.66

Table 4.4: Shot conditions for tests on aluminum.

Parameter	SG0402	SG0504	SG0602	SG0703	SG0802
Thermocouple (T/C) 1 (^{o}C)	-	500	599	601	597.5
Thermocouple (T/C) 2 (^{o}C)	-	432*	601	585	582.5
Average T/C (^{o}C)	-	500	600	593	590
Centerline T_0 (^{o}C)	22	495	591	584	582
Adiabatic T_f (^{o}C)	178	738	695	830	645
Adiabatic T_f (% of melt)	34.4	72.9	88.0	83.0	98.9
Approximate T_f (^{o}C)	137	657	627	753	609
Approximate T_f (% of melt)	31	67	82	77	95
Shear strain rate, $\dot{\gamma}$ (s^{-1})	1.19×10^6	1.85×10^6	1.29×10^6	1.41×10^6	1.52×10^6
Peak shear stress (MPa)	230	112	130	163	163
Maximum pressure, P (GPa)	5.35	6.76	2.37	5.66	6.13
Total shear strain, γ_{tot}	1.13	1.6	1.29	1.4	1.46/2.56**
Impact velocity, V_0 (m/s)	118.8	159.6	52.9	131.4	127.5
Impact angle, θ (^{o})	18	18	18	18	18
Tilt angle, α (^{o})	0.5	0.51	0.25	0.6	0.67
Closure angle Ω (^{o})	180	191.5	47.2	50.7	173
Aluminum purity (%)	99.999	99.999	99.0	99.999	99.999
Sample thickness, h (μm)	25	25	10	25	25
Initial grain size, D_0 (μm)	2-5	2-5	-	2-5	2-5
Time held at T_0, (min.)	-	90	140	130	137
Estimated grain size prior to impact, D_f (μm)	2-5	44	-	149	150
Target material	WC#832	WC#832	WC#832	WC#832	WC#832
Front target thickness, h_{fp} (mm)	1.83	1.65	1.68	1.59	1.76
Rear target thickness, h_{rp} (mm)	4	4.06	4.01	3.85	3.84
$c_1(T_0)$, ($mm/\mu s$)	6.88	6.77	6.74	6.74	6.74
$c_2(T_0)$, ($mm/\mu s$)	4.24	4.17	4.15	4.15	4.16
$\rho c_1(T_0)$, (GPa/($mm/\mu s$))	97.35	95.1	94.55	94.58	94.62
$\rho c_2(T_0)$, (GPa/($mm/\mu s$))	60	58.61	58.27	58.29	58.31
Flyer material	WC#832	WC#832	WC#112	WC#112	pure WC
Flyer thickness, h_{flyer} (mm)	3.96	4.05	4.05	8.06 ***	7.96
c_1(22^{o}C), ($mm/\mu s$)	6.88	6.88	6.69	6.69	6.86
c_2(22^{o}C), ($mm/\mu s$)	4.24	4.24	4.05	4.05	4.3
$\rho c_1(22°C)$, (GPa/($mm/\mu s$))	97.35	97.35	95.17	95.17	107
$\rho c_2(22°C)$, (GPa/($mm/\mu s$))	60	60	60	57.66	67.1

* A minor short was found in this thermocouple, leading to a lower temperature reading

** Total plastic strain at time of pressure drop/at end of test

*** The flyer for shot SG0703 was two plates of equal thickness (4.03 *mm* each)

Table 4.5: Room temperature properties of aluminum

Property (at 22°C, 1 atm)	Aluminum
$c_1 \left(mm/\mu s\right)$	6.42
$c_2 \left(mm/\mu s\right)$	3.04
$\rho \quad \left(kg/m^3\right)$	2698
$\rho c_1 \left(GPa/\left(mm/\mu s\right)\right)$	17.32
$\rho c_2 \left(GPa/\left(mm/\mu s\right)\right)$	8.2
Young's modulus, E $\left(GPa\right)$	67.5
Shear modulus, μ $\left(GPa\right)$	25
Possion's ratio υ	0.33
T_{melt} (K)	933
k (W/mK)	210
Cp (J/kgK)	896
α_v (K^{-1} x 10^{-6})	70

Table 4.6: Complete composition of 99.999% pure aluminum foil. Values are give in ppm.

As	0.017	B	0.05	Ce	0.016
Cl	0.019	Co	0.0012	Cr	0.01
Cu	0.3	Fe	0.3	K	<0.005
La	0.005	Li	<0.0006	Mg	0.4
Mn	0.014	Na	<0.0007	Nd	0.003
Ni	0.003	P	0.17	Pb	0.004
S	0.15	Sb	0.012	Sc	0.02
Si	1	Th	0.0007	Ti	0.04
U	0.0003	V	0.013	W	0.007
Y	0.0012	Zn	0.016		

Chapter 5

Finite Difference Simulations of Pressure-Shear Plate Impact Experiments on Aluminum

Numerical simulations of the high-temperature, pressure-shear plate impact experiment were performed to gain a better understanding of the dynamic response of aluminum. The finite difference method used in these simulations originated in the work by Ranganath and Clifton (1972). The method was implemented into pressure-shear plate impact problems by Gilat and Clifton (1985) and was then extended to include the case of finite deformations by Ramesh and Clifton (1992). The finite deformation formulation is discussed briefly in the following sections. A detailed formulation is provided by Tong et al. (1992).

5.1 Finite deformation formulation

5.1.1 Finite-deformation kinematics for pressure-shear

If the wave propagation is taken to be in the X_1 direction and the shearing is taken to be in the X_2 direction, then the deformation in a pressure-shear experiment can be written

$$\begin{aligned} x_1 &= \lambda(t)X_1, \\ x_2 &= X_2 - \kappa(t)X_1, \\ x_3 &= X_3 \end{aligned} \tag{5.1}$$

where the location (x_1, x_2, x_3) represents the spatial position of a particle at time t (i.e. in the current configuration) that was initially at the spatial coordinate (X_1, X_2, X_3) in the reference configuration. $\lambda(t)$ is the stretch in the X_1 direction and $\kappa(t)$ is the shear. For the deformation described in Equation (5.1), the total deformation gradient is

$$F = \begin{bmatrix} \lambda & 0 & 0 \\ -\kappa & 1 & 0 \\ 0 & 0 & 1 \end{bmatrix}. \tag{5.2}$$

The spatial velocity gradient is given by

$$L = \dot{F}F^{-1} = D + W = \begin{bmatrix} \dot{\lambda}/\lambda & 0 & 0 \\ -\dot{\kappa}/\lambda & 0 & 0 \\ 0 & 0 & 0 \end{bmatrix}, \tag{5.3}$$

where the symmetric part of the velocity gradient is the rate of deformation tensor, $D = \left(L + L^T\right)/2$, and the skew-symmetric part of the velocity gradient is the spin rate

tensor, $W = \left(L - L^T\right)/2$. The time derivates of λ and κ are written $\dot{\lambda}$ and $\dot{\kappa}$, respectively.

5.1.2 Momentum balance and compatibility relations

The balance of linear momentum is given by

$$\frac{\partial \Sigma_{11}}{\partial X_1} = \rho_0 \frac{\partial u}{\partial t}, \tag{5.4a}$$

$$\frac{\partial \Sigma_{21}}{\partial X_2} = \rho_0 \frac{\partial v}{\partial t}, \tag{5.4b}$$

where ρ_0 is the initial mass density and u and v are the particle velocities in the directions X_1 and X_2 respectively. Σ_{ij} are the components of the first Piola-Kirchhoff stress tensor Σ, which represent forces in the current configuration per unit area in the reference configuration. The Cauchy stress tensor σ, representing forces in the current configuration per unit area the current configuration, can be written in terms of the first Piola-Kirchhoff stress tensor as

$$\sigma = \frac{1}{J} F \Sigma^T, \tag{5.5}$$

where $J = \det F = \lambda(t)$ is the Jacobian which is the ratio of the current local volume to the corresponding reference volume.

The balance of angular momentum requires the Cauchy stress tensor to be symmetric, i.e.

$$\sigma = \sigma^T, \tag{5.6}$$

which imposes the following restriction on the first Piola-Kirchhoff stress tensor

$$F\Sigma^T = \Sigma F^T. \tag{5.7}$$

This restriction limits the form of the first Piola-Kirchhoff stress tensor for pressure-shear deformations to

$$\Sigma = \begin{bmatrix} \Sigma_{11} & \kappa\Sigma_{11} + \lambda\Sigma_{21} & 0 \\ \Sigma_{21} & \Sigma_{22} & 0 \\ 0 & 0 & \Sigma_{33} \end{bmatrix}, \tag{5.8}$$

The compatibility conditions are found by differentiating Equation (5.1) with respect to X_1 and t:

$$\frac{\partial u}{\partial X_1} = \frac{\partial \lambda}{\partial t}, \tag{5.9a}$$

$$\frac{\partial v}{\partial X_1} = -\frac{\partial \kappa}{\partial t}. \tag{5.9b}$$

5.1.3 Constitutive relations

The aluminum sample is modeled as an elastic/viscoplastic solid. The deformation gradient can be decomposed into an elastic part and a plastic part:

$$F = F^e F^p. \tag{5.10}$$

Substituting Equation (5.10) into the definition of the spatial velocity gradient (Equation (5.3)) one can decompose the spatial velocity gradient as:

$$\begin{aligned} L &= \dot{F}^e F^{e-1} + F^e \dot{F}^p F^{p-1} F^{e-1} \\ &= L^e + L^p = \left(D^e + W^e\right) + \left(D^p + W^p\right). \end{aligned} \tag{5.11}$$

Tong et al. (1992) report the complete derivation of the constitutive relation concluding with the final relation which is used to calculate stress changes from changes in deformation:

$$\dot{\Sigma}^T = F^{-1}\left(C^e : D\right) + \Sigma^T L^T - F^{-1}\left(C^e : D^p\right) - F^{-1} D^p F \Sigma^T - \Sigma^T D^p. \tag{5.12}$$

For isotropic materials the elastic stiffness tensor, C^e, has components given by

$$C^e_{ijkl} = \mu^e\left(\delta_{ik}\delta_{jl} + \delta_{il}\delta_{jk}\right) + \lambda^e\delta_{ij}\delta_{kl}, \tag{5.13}$$

where λ^e and μ^e are the elastic Lamé and bulk moduli respectively.

In this formulation, deformations of small elastic strains but large plastic strains are considered. The plastic deformation is taken to be incompressible, and therefore

$$\det F^p = 1. \tag{5.14}$$

The rate of plastic deformation tensor D^p is given by the flow law

$$D^p = \Phi\frac{S}{2\bar{\tau}} \tag{5.15}$$

where

$$S = \sigma - \frac{1}{3}(trace\sigma)\mathrm{I} \tag{5.16}$$

is the deviatoric stress tensor and $\bar{\tau}^2 = \frac{1}{2}S_{ij}S_{ij} = J_2$ is the second invariant of *S*. The plastic strain rate function is $\Phi = \dot{\bar{\gamma}}_p = \sqrt{2D^p_{ij}D^p_{ij}}$ – which is a function of the effective shear stress $\bar{\tau}$, the deformation history, the temperature *T*, and the effective plastic shear strain, $\bar{\gamma}_p = \int_0^t \dot{\bar{\gamma}}_p dt$. Three constitutive models for the plastic strain rate function are considered to simulate the dynamic response of aluminum (section 5.2).

Using the compatibility equations (Equations (5.9)) to replace the rates of deformation ($\dot{\lambda}$ and $\dot{\kappa}$) with the velocity gradients, one can write the constitutive relation (Equation 5.12) as

$$\frac{\partial \Sigma_{11}}{\partial t} = A_1 \frac{\partial u}{\partial X_1} - R_1, \tag{5.17a}$$

$$\frac{\partial \Sigma_{21}}{\partial t} = B_2 \frac{\partial v}{\partial X_1} - R_2, \tag{5.17b}$$

$$\frac{\partial \Sigma_{22}}{\partial t} = A_3 \frac{\partial u}{\partial X_1} + B_3 \frac{\partial v}{\partial X_1} - R_3, \tag{5.17c}$$

$$\frac{\partial \Sigma_{33}}{\partial t} = A_4 \frac{\partial u}{\partial X_1} - R_4, \tag{5.17d}$$

where

$$A_1 = \frac{\Sigma_{11}}{\lambda} + \frac{2\mu^e + \lambda^e}{\lambda^2} \tag{5.18a}$$

$$R_1 = \frac{\dot{\bar{\gamma}}_p}{\lambda \bar{\tau}} \left(\lambda S_{11} \Sigma_{11} + S_{21} S_{21} + \mu^e S_{11} \right) \tag{5.18b}$$

$$B_2 = \frac{\Sigma_{11}}{\lambda} + \frac{\mu^e}{\lambda^2} \tag{5.18c}$$

$$R_2 = \frac{\dot{\bar{\gamma}}_p}{2\lambda \bar{\tau}} \left(4PS_{21} - 2\Sigma_{33} S_{21} + 2\mu^e S_{21} \right) \tag{5.18d}$$

$$A_3 = \frac{\lambda^e}{\lambda} \tag{5.18e}$$

$$B_3 = \Sigma_{21} + \frac{\kappa}{\lambda} \Sigma_{11} + \frac{\kappa}{\lambda^2} \mu^e \tag{5.18f}$$

$$R_3 = \frac{\dot{\bar{\gamma}}_p}{\lambda \bar{\tau}} \left(\lambda S_{22} \Sigma_{22} + \kappa \lambda S_{21} \Sigma_{11} + \lambda S_{21} S_{21} + \mu^e \left(\lambda S_{22} + \kappa S_{21} \right) \right) \tag{5.18g}$$

$$A_4 = \frac{\lambda^e}{\lambda} \tag{5.18h}$$

$$R_4 = \frac{\dot{\bar{\gamma}}_p}{\bar{\tau}} S_{33} \left(\Sigma_{33} + \mu^e \right). \tag{5.18i}$$

S_{ij} are components of the deviatoric stress tensor (Equation (5.16)) and $P = \left(\sigma_{11} + \sigma_{22} + \sigma_{33} \right)/3$ is the pressure.

Equations (5.17) and the momentum balance equations (Equations (5.4)) make up a system of quasilinear, strongly hyperbolic, partial differential equations which can be written as difference equations along characteristics:

$$d\Sigma_{11} \mp \rho_0 c\,du = -R_1 dt\,, \qquad c = \pm c_f \tag{5.19a}$$

$$d\Sigma_{21} \mp \rho_0 c\,dv = -R_2 dt\,, \qquad c = \pm c_s \tag{5.19b}$$

and

$$d\Sigma_{22} = \frac{A_3}{A_1}\left(d\Sigma_{11} + R_1 dt\right) + \frac{B_3}{B_2}\left(d\Sigma_{21} + R_2 dt\right) - R_3 dt\,, \qquad c = 0 \tag{5.19c}$$

$$d\Sigma_{33} = \frac{A_4}{A_1}\left(d\Sigma_{11} + R_1 dt\right) - R_4 dt\,, \qquad c = 0 \tag{5.19d}$$

where $c_f = \sqrt{A_1/\rho_0}$ is the fast wave speed and $c_s = \sqrt{B_2/\rho_0}$ is the slow wave speed. These wavespeeds become the elastic longitudinal and shear wave speeds (c_1 and c_2) at small deformations.

5.1.4 Numerical scheme and stability conditions

A finite difference scheme based on integration along characteristics – developed by Ranganath and Clifton (1972) – is used to solve Equations (5.19). The method is explicit, second order accurate, and conditionally stable. Using a Courant-Friedrichs-Levy (CFL) number less than one ensures the stability of the method for the system of hyperbolic partial differential equations. However, heat flow is governed by parabolic equations which apply an additional constraint on the time step. Shawki and Clifton (1989) provide a composite stability condition that, if satisfied, ensures stability in the current simulations:

$$\frac{\Delta t}{\Delta x} \le \min\left(\frac{1}{c_1}, \frac{\Delta x}{2D}\right) \tag{5.20}$$

where D is the thermal diffusivity, c_1 is the longitudinal wave speed, Δx is the mesh size and Δt is the time step.

The thermal analysis (Chapter 3) details the temperature change in a sample for the pressure-shear plate impact experiment if the process it taken to be adiabatic. For these simulations, the process is not assumed to be adiabatic and heat is allowed to flow out of the sample. The heat generation is simulated using Equation (3.16) where the volumetric coefficient of thermal expansion is temperature dependent and the specific heat capacity is pressure and temperature dependent. The temperature is calculated at every time step using a forward time – central difference scheme.

5.2 Constitutive models

5.2.1 Johnson/Cook model

Three constitutive models for the plastic strain rate function Φ were used to carry out the numerical analysis of aluminum. The first was a model developed by Johnson and Cook (1985) and is commonly used for impact problems. They proposed the following constitutive law:

$$\sigma = \left(A + B\varepsilon^n\right)\left[1 + C\ln\left(\frac{\dot{\varepsilon}}{\dot{\varepsilon}_0}\right)\right]\left(1 - \left(\frac{T - T_0}{T_m - T_0}\right)^m\right), \tag{5.21}$$

where A is the static shear strength, B is the strain-hardening modulus, C is the rate sensitivity coefficient, m is the thermal-softening exponent, n is the strain-hardening exponent, $\sigma = \bar{\tau}\sqrt{3}$, $\dot{\varepsilon} = \dot{\bar{\gamma}}_p / \sqrt{3}$, T is the current temperature, and T_0 is room

temperature. T_m is the melting temperature which, for the current simulations, is taken to vary with pressure (see Equation 3.1). The plastic strain rate function for the Johnson/Cook model is obtained by rearranging Equation (5.21):

$$\Phi = \dot{\bar{\gamma}}_p = \sqrt{3}\dot{\varepsilon}_0 \exp\left[\frac{\bar{\tau}\sqrt{3}}{C\left(A + B\varepsilon^n\right)\left(1-\Theta^m\right)} - \frac{1}{C}\right], \qquad \Theta = \frac{T - T_0}{T_m - T_0} \tag{5.22}$$

Note that strain rate grows exponentially with the effective shear stress. In order to deal with the high stresses during the initial elastic response, it is necessary to limit the strain rate. Therefore, a limiting strain rate, $\dot{\gamma}_0$, is combined with the strain rate from the model, $\dot{\bar{\gamma}}_p$, in a manner that allows the lowest of the two strain rates to dominate and maintains a continuous slope in the stress/strain-rate relation:

$$\dot{\gamma} = \frac{\dot{\bar{\gamma}}_p \dot{\gamma}_0}{\dot{\bar{\gamma}}_p + \dot{\gamma}_0}. \tag{5.23}$$

A set of parameters for the Johnson/Cook model were chosen based on the data available on high purity aluminum (Morrone (1986), Klopp (1987), Yoshida and Nagata (1966), Lindholm and Yeakley (1964), Huang (1986)). The second term in Equation (5.21) governs the strain rate sensitivity, and is modeled as taking the flow stress to have a simple logarithmic dependence on strain rate. As is evident from Figure 4.31, the strain rate sensitivity is not a simple logarithmic relation – one which would appear linear on the semi-log plot. However, if a high reference strain rate ($\dot{\varepsilon}_0$ =1.82 x 10^4 s^{-1}) is used, the simple logarithmic relation for the strain rate sensitivity becomes more appropriate for use in the simulation of high purity aluminum at strain rates on the order of 10^6 s^{-1}. The thermal softening parameter, *m*, was chosen to fit the experimental results for the room temperature (shot SG0402) and 582°C (shot SG0703) tests on 99.999% pure aluminum.

The Johnson/Cook model parameters chosen for high purity aluminum are given in Table 5.1 and are used to simulate shots SG0402 (T_0=22^{o}C), SG0703 (T_0=584^{o}C) and SG0802 (T_0=582^{o}C, with pressure drop).

The computed pressures, normal stresses and shear stresses are plotted versus time in Figure 5.1 for the simulations of shots SG0402 and SG0703. The normal and shear stresses are plotted for the nodes at the front, the back, and the middle of the sample. The pressure is plotted for the node at the middle of the sample. The particle velocities computed in the rear target plates are used to calculate the nominal shear stress in the sample, analogous to how the free-surface velocity profiles are used to calculate the nominal stresses for the experiments. These computed nominal shear stresses are also plotted for both simulations in Figure 5.1.

The normal stress for both simulations becomes nearly uniform across the sample in less than 25 *ns* and stays at a constant level for the duration of the simulation. The normal stress for the simulation of shot SG0703 is higher than that of shot SG0402 due to the higher imposed impact velocity. Refer to Table 4.4 for experimental shot conditions.

When the shear wave first arrives at the sample, there is a spike in the shear stress due to the elastic response of the sample. The shear stress becomes nearly uniform through the thickness of the sample about 35 *ns* after the arrival of the shear wave. In the Johnson/Cook constitutive model (Equation (5.21)), the third term decreases with increasing temperature. Therefore, the overall flow stress decreases monotonically with increases in temperature. This behavior is confirmed in the simulated responses that

show that the computed shear stress is larger for the simulation of shot SG0402 (T_0=22^{o}C) than that for shot SG0703 (T_0=584^{o}C). For both simulations the pressure is nominally the same as the normal stress after the arrival of the shear wave.

The normal and shear strains computed at the front, back and middle of the sample from the simulations of shots SG0402 and SG0703 are shown in Figure 5.2 and Figure 5.3 respectively. The particle velocities computed in the front and rear target plates were used to calculate the nominal shear strain rate in the sample. This nominal strain rate was integrated to find the nominal shear strain, which is plotted for both simulations in Figures 5.2 and 5.3

In both simulations, the normal strain is less than 7.5% and stays uniform through the thickness of the sample. The accumulated shear strains are much larger and are not uniform across the sample. The accumulated shear strain at the middle of the sample is greater than at the front and back of the sample. The shear strains calculated from the target plate particle velocities shows a nominal strain that is less than the strain at the middle of the sample and greater than the strain at the edges of the sample.

The disparity in accumulated shear strain arises from the non-uniformity of the shear strain rate through the thickness of the sample, due to the temperature distribution across the sample. The temperature distributions for the simulation of shots SG0402 and SG0703 are shown at evenly spaced time increments in Figure 5.4 and Figure 5.5 respectively. The temperature of the sample and target plates both increase with pressure. However, since the aluminum sample has a smaller value of specific heat capacity and a much larger coefficient of thermal expansion than the tungsten carbide

target plates, the temperature rise in the sample due to the increase in pressure is significantly greater (see Equation 3.16). Heat from the sample is conducted into the colder target plates, resulting in the temperature computed at the edges of the sample being lower than the temperature computed in the middle of the sample. Approximately 25 *ns* after the longitudinal wave arrives, the temperature difference between the middle and the edges of the sample are 25 degrees and 90 degrees for simulations of shots SG0402 and SG0703 respectively. Noting the effect of temperature on the plastic strain rate function for the Johnson/Cook model (Equation (5.22)), the temperature variation in the sample creates a similar gradient in the strain rate as shown in Figures 5.6 and 5.7. The strain rate appears to settle to a steady value over time without becoming uniform through the thickness.

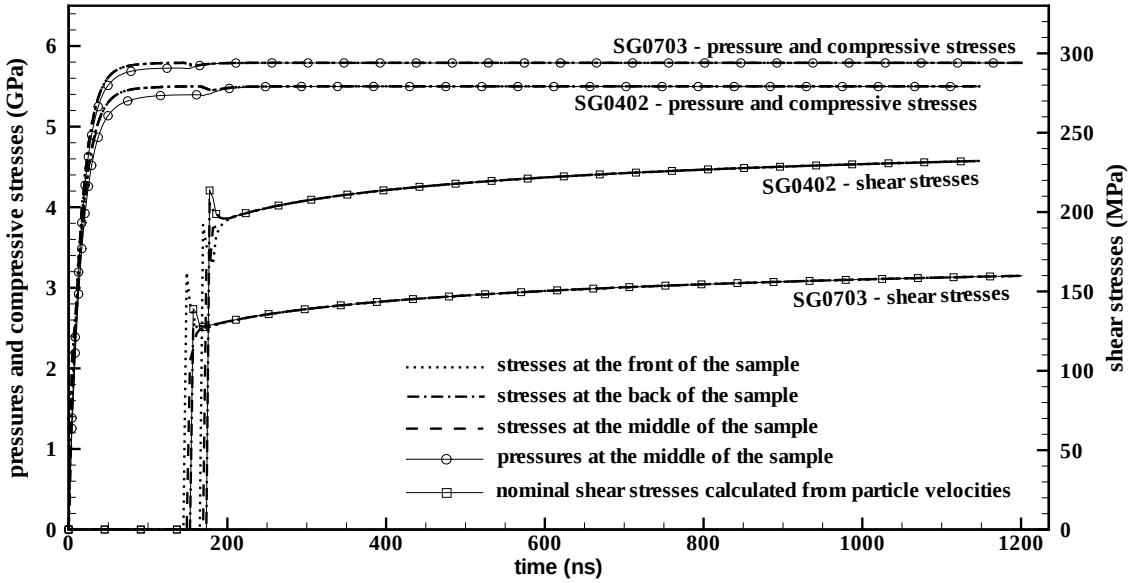

Figure 5.1: Pressures, compressive stresses and shear stresses simulated using the Johnson/Cook model for shots SG0402 (T_0=22°C) and SG0703 (T_0=584°C).

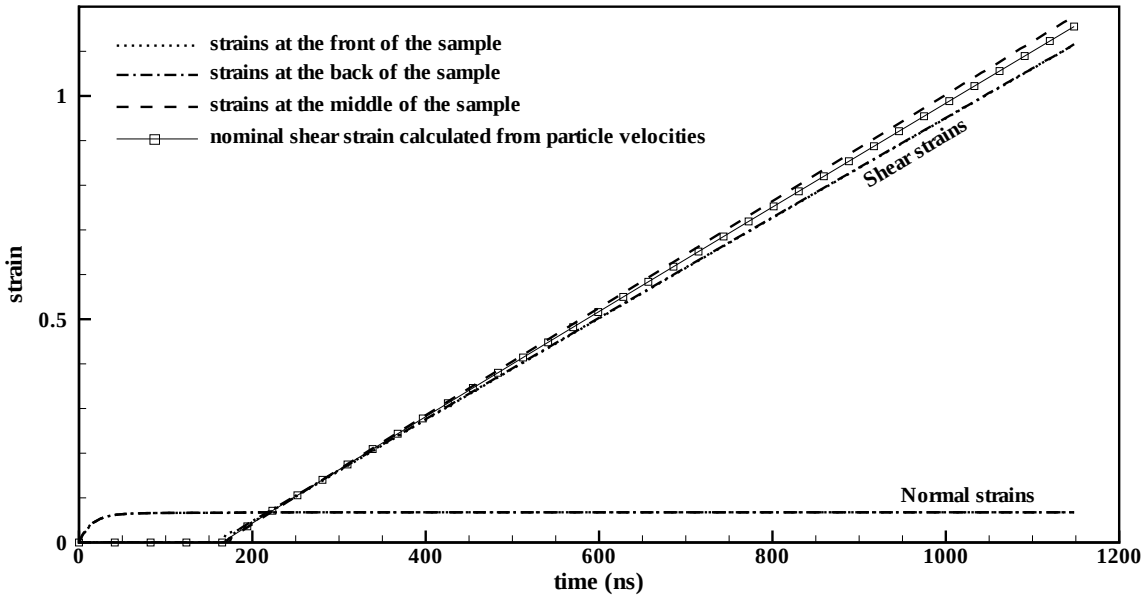

Figure 5.2: Normal and shear strains computed for the simulations of shot SG0402 (T_0=22°C) using the Johnson/Cook model.

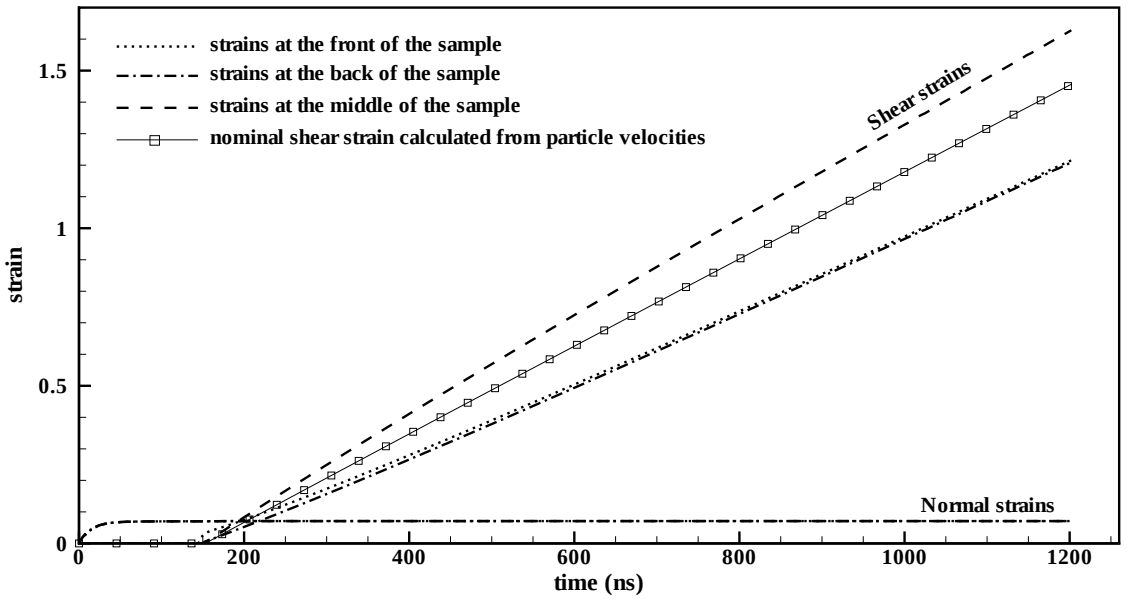

Figure 5.3: Normal and shear strains computed for the simulations of shot SG0703 (T_0=584°C) using the Johnson/Cook model.

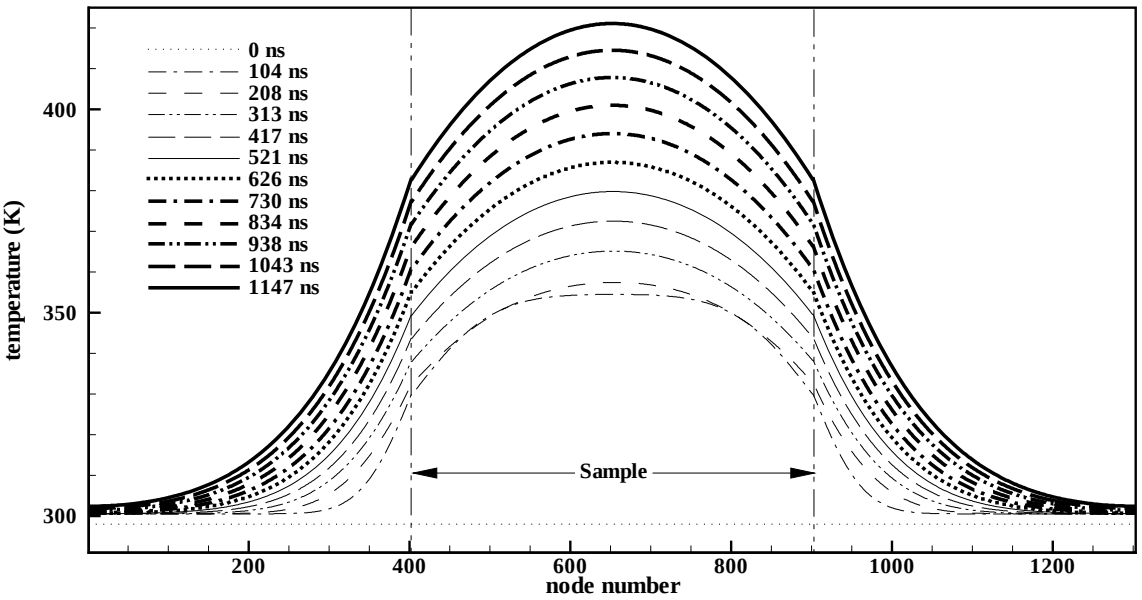

Figure 5.4: Johnson/Cook model temperature distribution for the simulation of shot SG0402 (T_0=22°C).

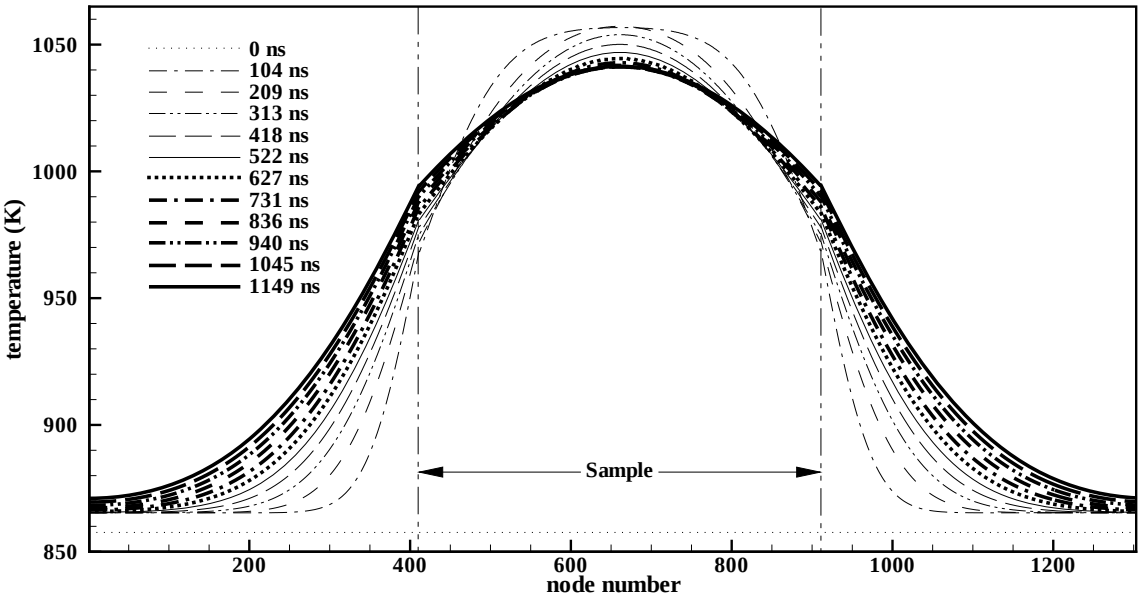

Figure 5.5: Johnson/Cook model temperature distribution for the simulation of shot SG0703 (T_0=584°C).

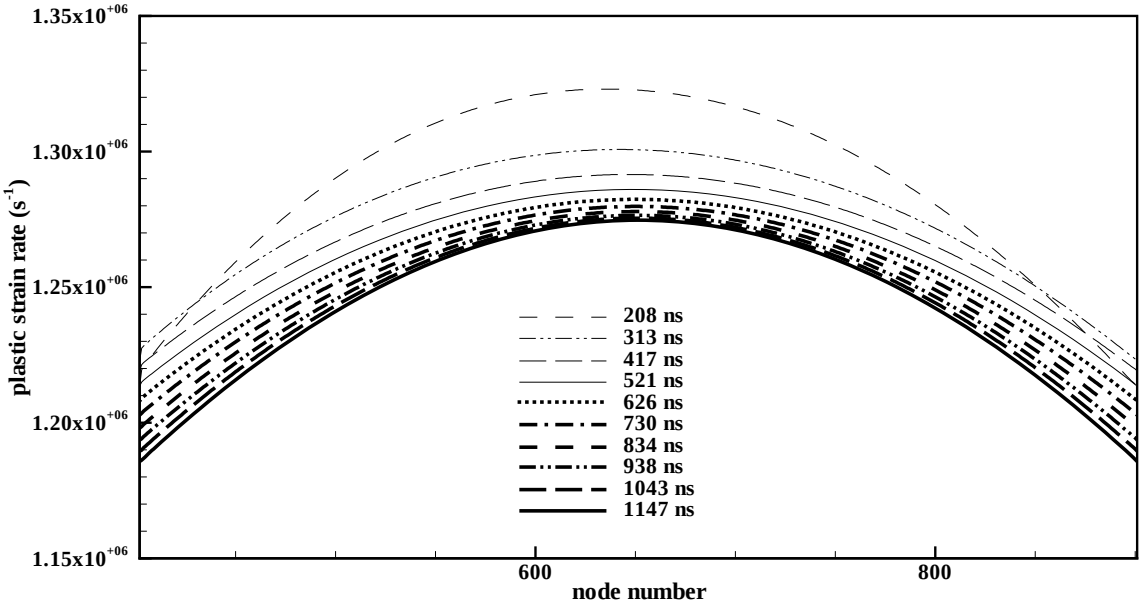

Figure 5.6: Johnson/Cook model strain rate distribution for the simulation of shot SG0402 (T_0=22°C).

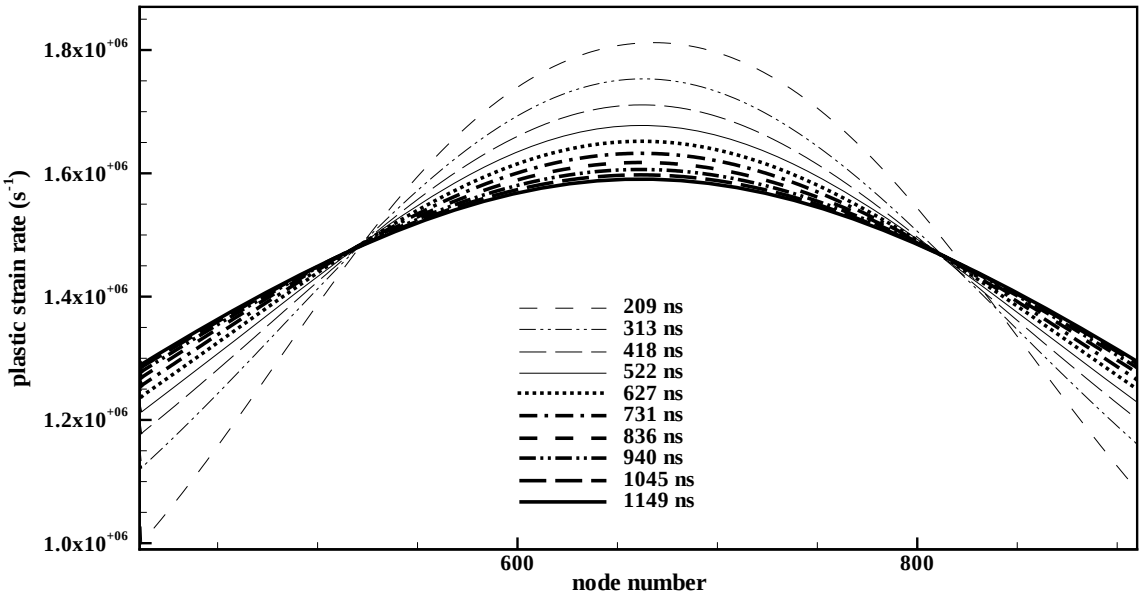

Figure 5.7: Johnson/Cook model strain rate profiles for the simulation of shot SG0703 (T_0=584°C).

The same Johnson/Cook model parameters were use to simulate shot SG0802 at a starting temperature of 582^{o}C with a pressure drop. The normal and shear stresses computed at the front, back and middle of the sample are plotted versus time in Figure 5.8. As in the simulations of SG0402 and SG0703, the normal and shear stresses quickly become uniform through the sample and the pressure is nearly equal to the normal stress. At approximately 1120 *ns*, the simulated unloading wave reflected from the rear surface of the target arrives at the sample and the normal stress and pressure decrease. Figure 5.9 displays the sample temperature (at the middle of the sample) and the melting temperature as a function of time. At the time of the pressure drop, both the sample temperature and the melting temperature decrease, however the ratio of sample temperature to melting temperature increases. Therefore, the term governing thermal softening in the Johnson/Cook constitutive model (third term in Equation (5.21)) decreases after the pressure drops, thereby decreasing the shear stress (see Figure 5.8).

The normal and shear strains computed at the front, back and middle of the sample are also plotted versus time in Figure 5.10. The normal strains are less than 7.5% and stay uniform through the sample. The accumulated shear strains are larger in the middle of the sample until after the pressure drops. As in the simulations for SG0402 and SG0703, the shear strain discrepancy is due to the non-uniformity of the shear strain rate through the thickness of the sample because of the temperature distribution across the sample where the temperature in the middle of the sample is higher than the temperature at the edges before the pressure drops. After the pressure drops, however, the temperature in the middle of the sample is lower than the temperature at the edges of the

sample (as shown in Figure 5.11), leading to the strain rate distribution shown in Figure 5.12.

The sample temperature and melting temperature are plotted versus normalized volume in Figure 5.13. The sample temperature starts at 855 K and rises as the volume of the sample decreases. When the sample reaches a volume of 0.926 times the initial volume, the sample temperature begins to decrease as heat from the sample is conducted in to the colder target plates faster than heat is generated through plastic work. After the unloading wave arrives at the sample, the volume increases and the sample temperature decreases to 850 K. Then, while at the final volume, the temperature begins to increase again. After the pressure drops, the temperature in the surrounding target plates is higher than in the sample and heat diffuses into the sample (see Figure 5.11). Also, the sample is still being deformed in shear and plastic work is contributing to the temperature increase. Direct comparisons of the simulated results to the experimental results will be made in Section 5.3.

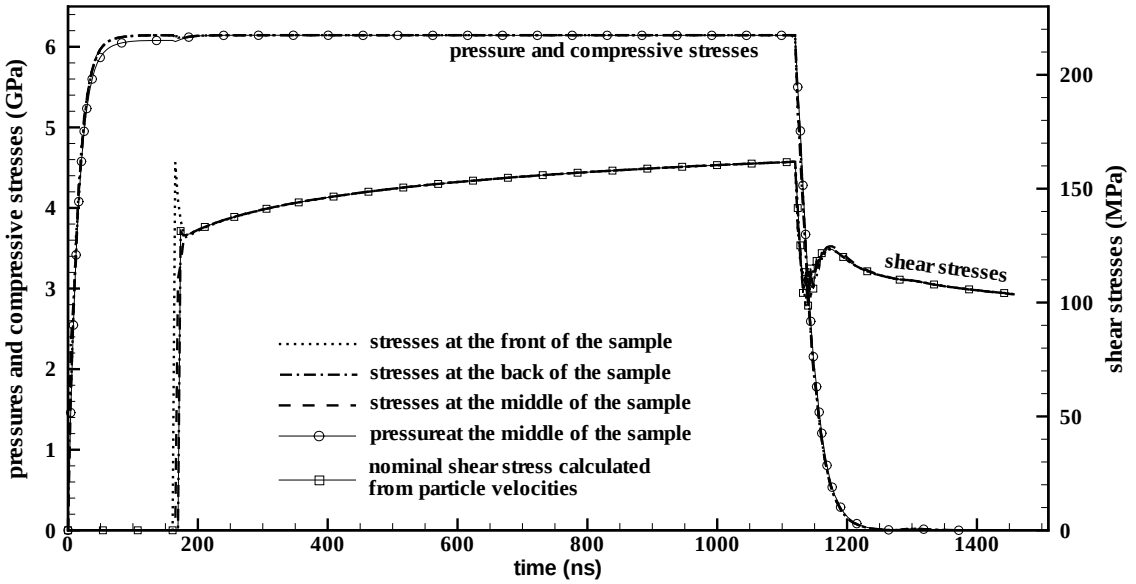

Figure 5.8: Pressures, compressive stresses and shear stresses simulated using the Johnson/Cook model for shot SG0802 (T_0=582°C).

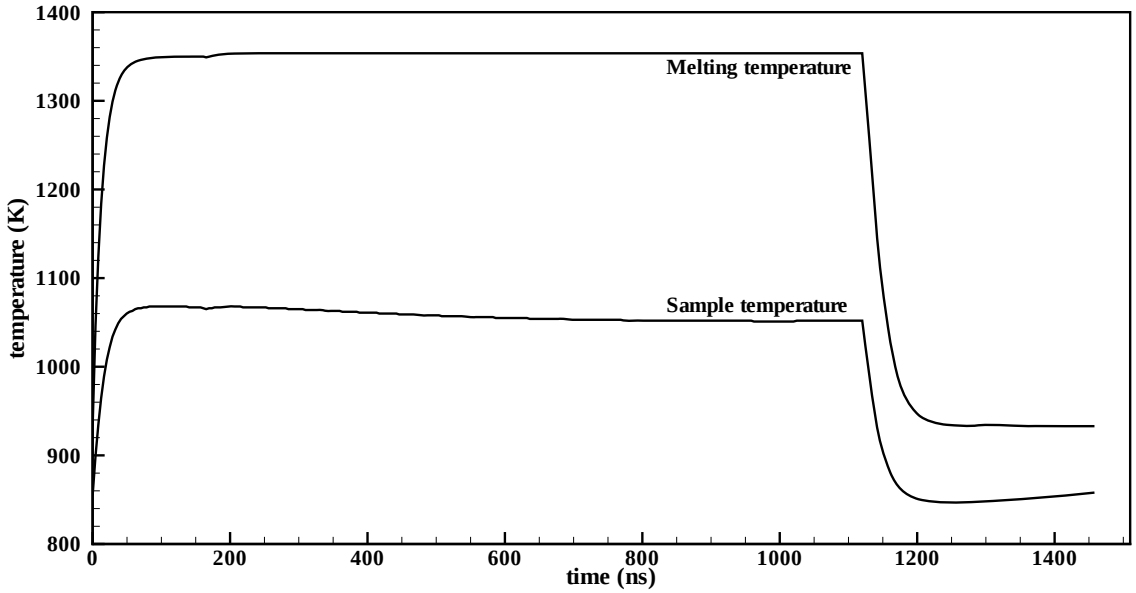

Figure 5.9: Sample temperature and melting temperature simulated using the Johnson/Cook model for shot SG0802 (T_0=582°C) plotted versus time.

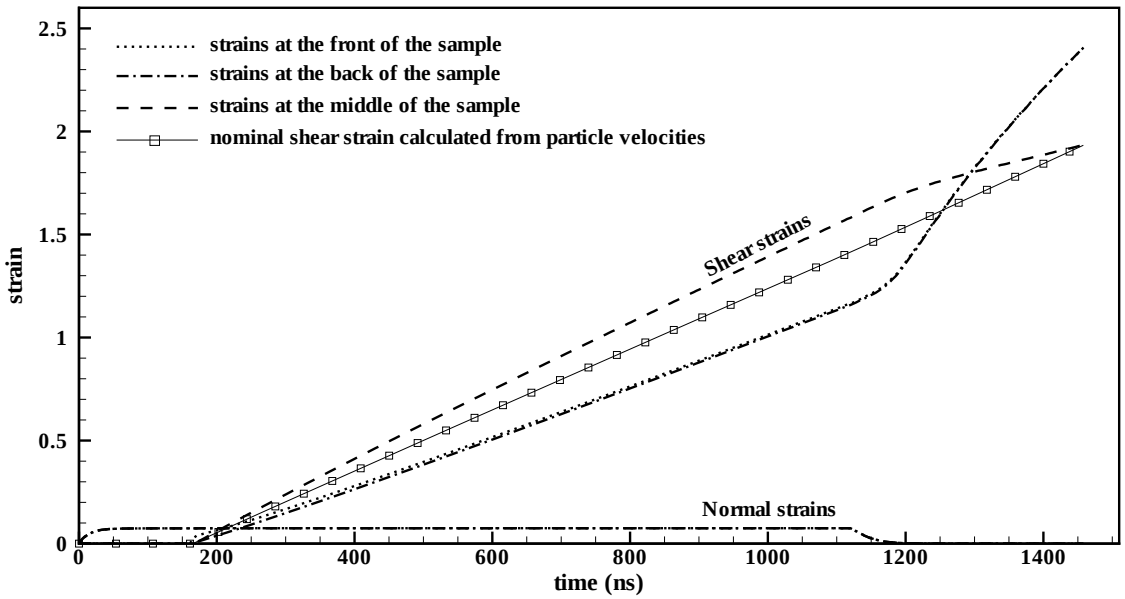

Figure 5.10: Normal and shear strains computed for the simulations of shot SG0802 (T_0=582°C) using the Johnson/Cook model.

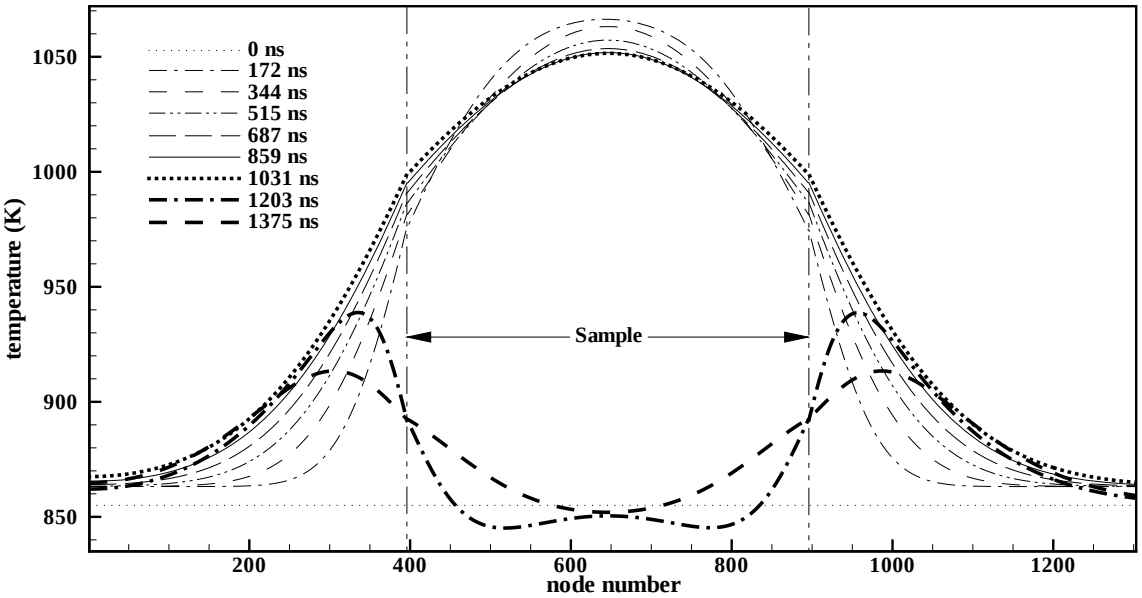

Figure 5.11: Johnson/Cook model temperature distribution for the simulation of shot SG0802 (T_0=582°C).

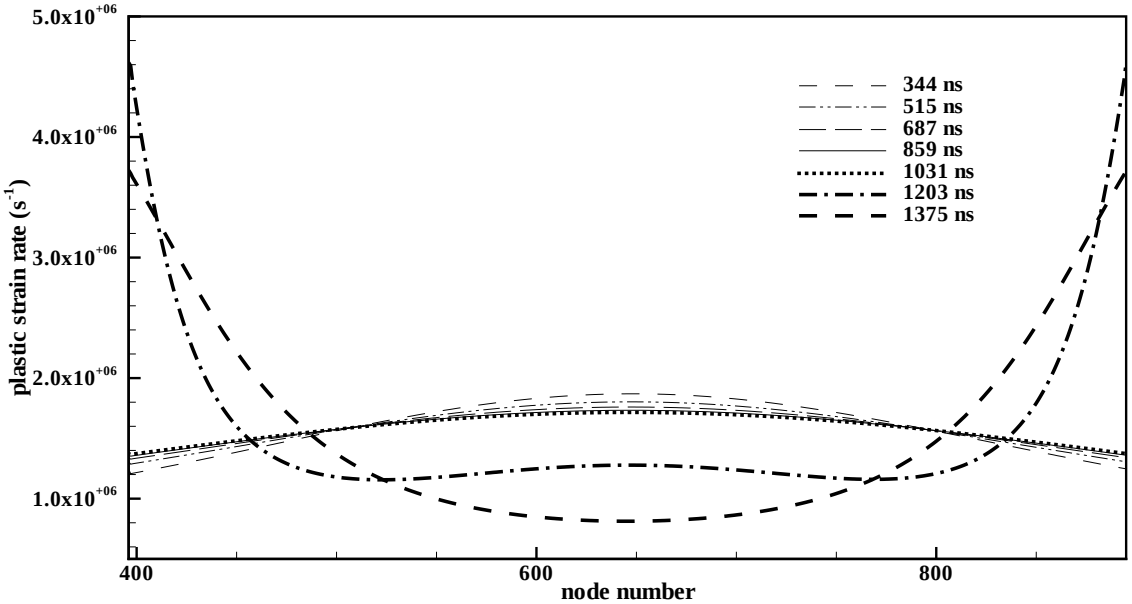

Figure 5.12: Johnson/Cook model strain rate profiles for the simulation of shot SG0802 (T_0=582°C).

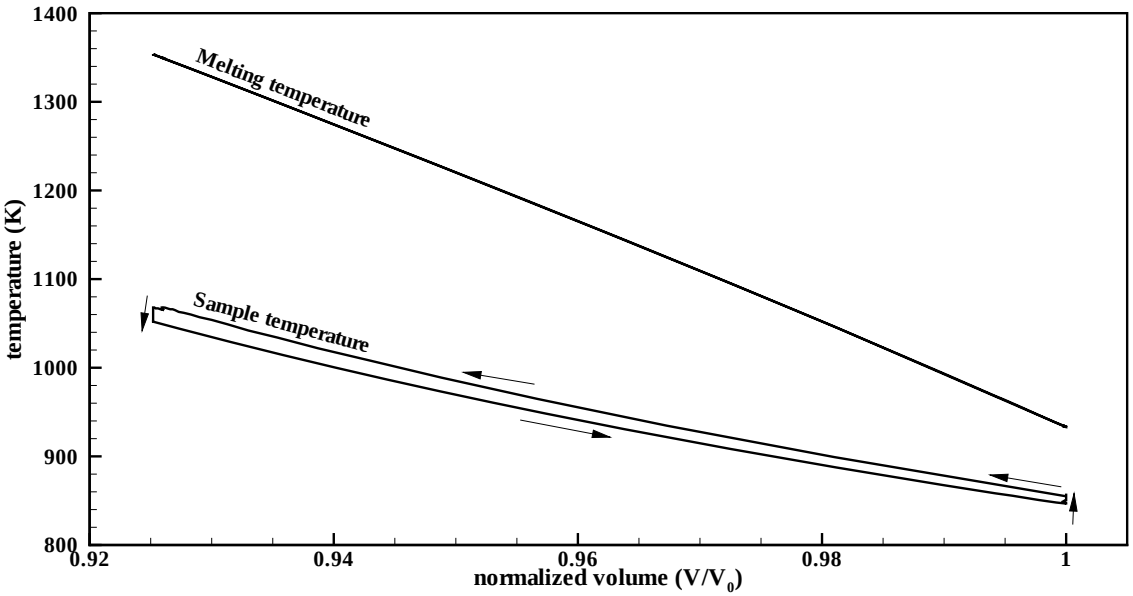

Figure 5.13: Sample temperature and melting temperature simulated using the Johnson/Cook model for shot SG0802 (T_0=582°C) plotted versus normalized volume.

5.2.2 Nemat-Nasser/Isaacs model

The second constitutive model used in the current simulations was developed by Nemat-Nasser and Isaacs (1997). This model divides the flow stress into two parts – an athermal part, τ_a, and a thermally-activated part, τ^*:

$$\bar{\tau} = \tau_a + \tau^* . \tag{5.24}$$

The athermal stress, which is intended to account for the effect of long-range barriers to dislocation motion, is represented in the form

$$\tau_a = \tau_0 \bar{\gamma}_p^n , \tag{5.25}$$

where τ_0 and n are constants and $\bar{\gamma}_p$ is the effective plastic shear strain. The thermally-activated part, which deals with the effect of short range barriers, is given by

$$\tau^* = \hat{\tau}\left\{1 - \left[-\frac{k}{G_0}T\left(\ln\frac{\dot{\bar{\gamma}}_p}{\dot{\gamma}_r}\right)\right]^{1/q}\right\}^{1/p} . \tag{5.26}$$

where k is the Boltzmann constant, $\dot{\gamma}_r$ is a reference strain rate, $\hat{\tau}$ is the threshold stress of the barrier to dislocation motion, G_0 is the total energy of the barrier, and p and q are constants that define the shape of the barrier. The thermally-activated part of the flow stress decreases with increasing temperature. For a given strain rate, there is a critical temperature, T_C, at which the thermally-activated part of the flow stress becomes zero. For temperatures above the critical temperature, the model presented by Nemat-Nasser and Isaacs (1997) sets the total flow stress equal to the athermal flow stress.

By combining and rearranging Equations (5.24), (5.25) and (5.26), the plastic strain rate function for the Nemat-Nasser/Isaacs model is found to be

$$\Phi = \dot{\bar{\gamma}}_p = \dot{\gamma}_r \exp\left(\frac{-G_0}{kT} \left[1 - \left(\frac{\bar{\tau} - \tau_0 \bar{\gamma}_p^n}{\hat{\tau}} \right)^p \right]^q \right) \tag{5.27}$$

This function is valid only for flow stresses that are larger than the athermal stress or, in other words, for temperatures below the critical temperature. For aluminum, tested at strain rates on the order of 10^6 s^{-1}, the critical temperature is ~13250°C. The sample temperature never comes close to reaching the critical temperature in these simulations. Values for G_0 and $\dot{\gamma}_r$ are found for high purity aluminum in the literature (Kocks (1976), Nemat-Nasser and Isaacs (1997) and Klopp et al. (1985)). The remaining parameters are chosen to fit the simulations to the experimental results. The parameter values used for simulations based on the Nemat-Nasser/Isaacs model are given in Table 5.2.

The computed pressures, normal stresses and shear stresses are plotted versus time in Figure 5.14 for the simulations of shots SG0402 and SG0703. The normal and shear strains computed from the simulations of shots SG0402 and SG0703 are shown in

Figure 5.15 and Figure 5.16 respectively. The difference in total accumulated shear strain between the middle of the sample and the edges is significantly less when using the Nemat-Nasser/Isaacs model (5% difference for SG0703) than when using the Johnson/Cook model (35% difference for SG0703). Again, the difference in accumulated shear strain is due to the non-uniformity of the shear strain rate through the thickness of the sample due to the temperature distribution across the sample. The temperature distributions for shot SG0402 and SG0703 are shown Figures 5.17 and 5.18 respectively. In the Nemat-Nasser/Isaacs model, with the parameters chosen, the shear strain rate is less sensitive to temperature than for the Johnson/Cook model. Therefore, a similar temperature distribution field results in a smaller shear strain rate difference between the middle and the edges of the sample. The shear strain rate distributions are shown at various times for the simulations of shot SG0402 and SG0703 in Figure 5.19 and Figure 5.20 respectively.

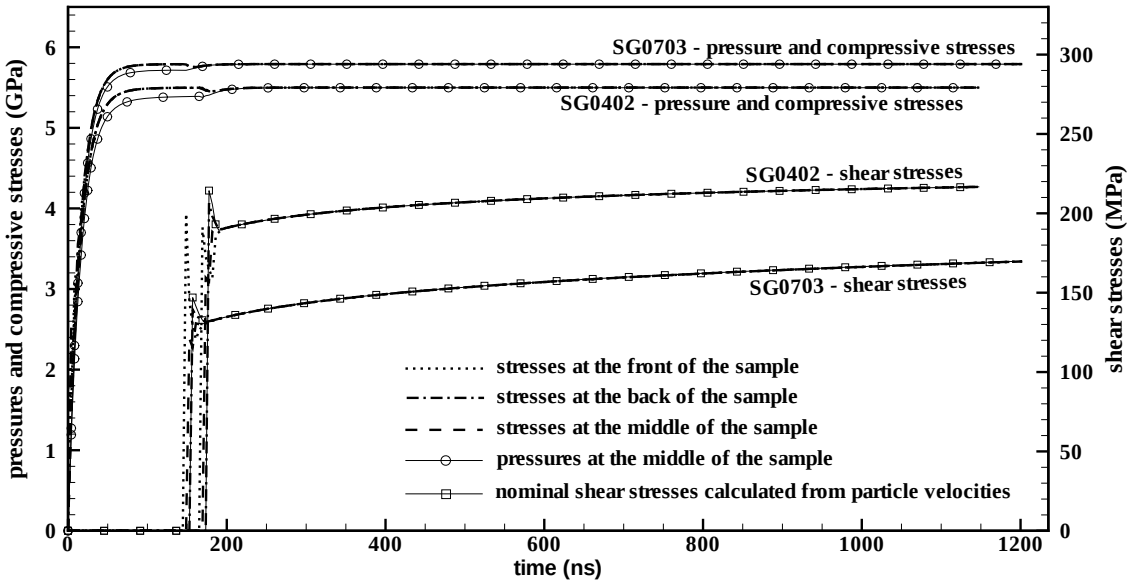

Figure 5.14: Pressures, compressive stresses and shear stresses simulated using the Nemat-Nasser/Isaacs model for shots SG0402 and SG0703.

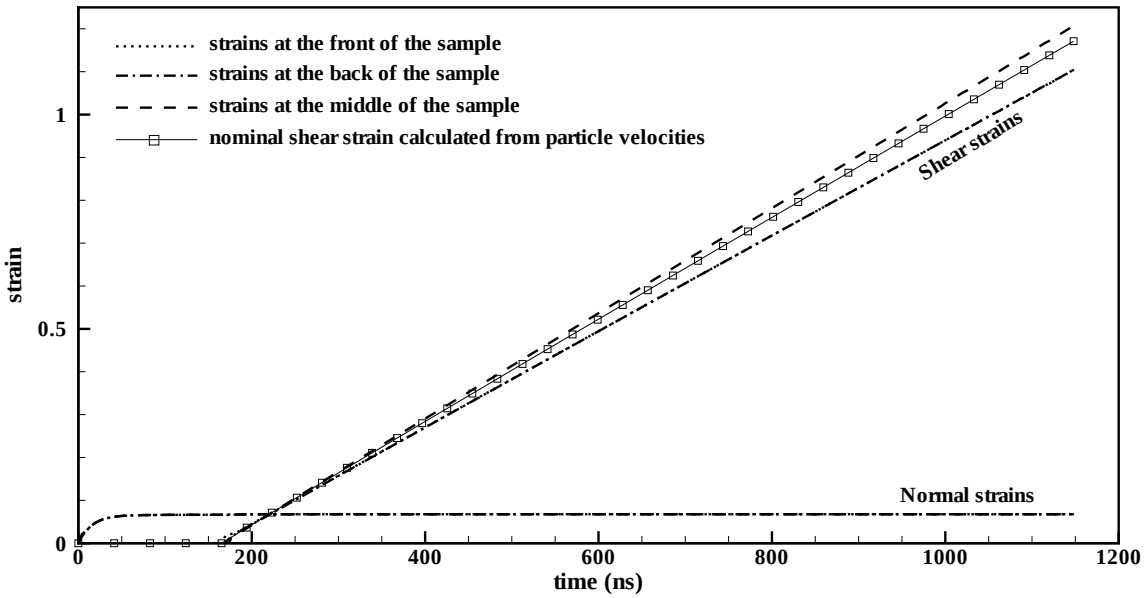

Figure 5.15: Normal and shear strains computed for the simulations of shot SG0402 (T_0=22°C) using the Nemat-Nasser/Isaacs model.

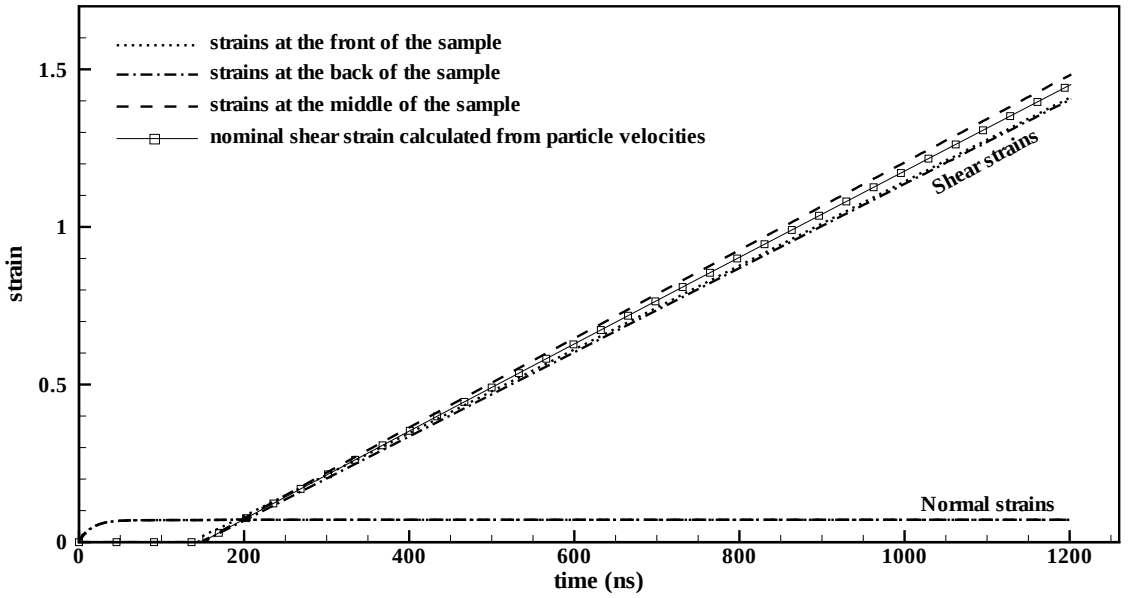

Figure 5.16: Normal and shear strains computed for the simulations of shot SG0703 (T_0=584°C) using the Nemat-Nasser/Isaacs model.

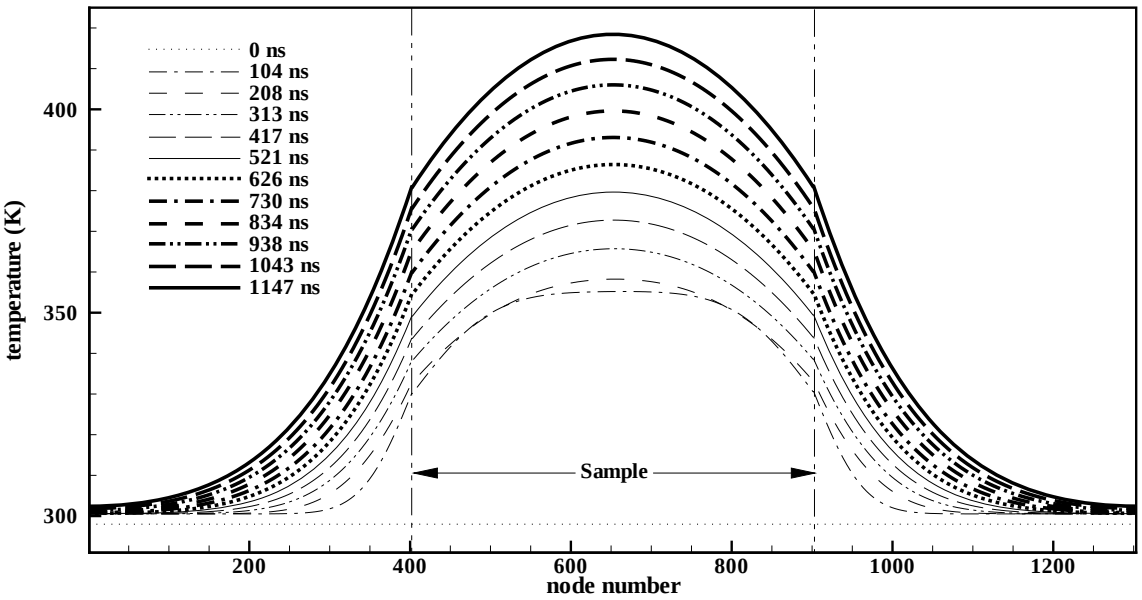

Figure 5.17: Nemat-Nasser/Isaacs model temperature distribution for the simulation of shot SG0402 (T_0=22°C).

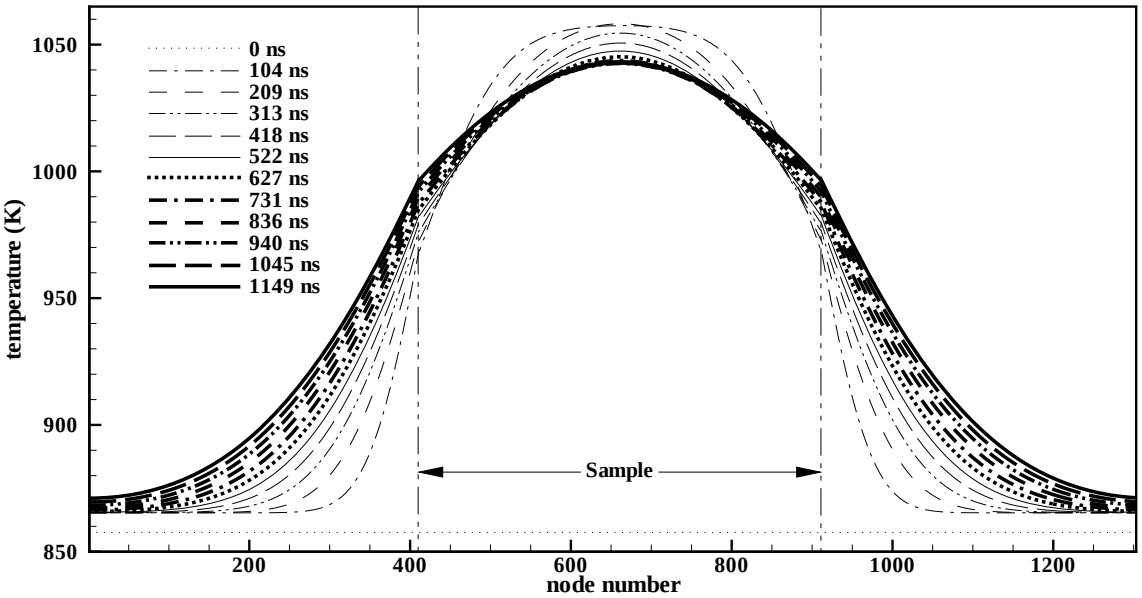

Figure 5.18: Nemat-Nasser/Isaacs model temperature distribution for the simulation of shot SG0703 (T_0=584°C).

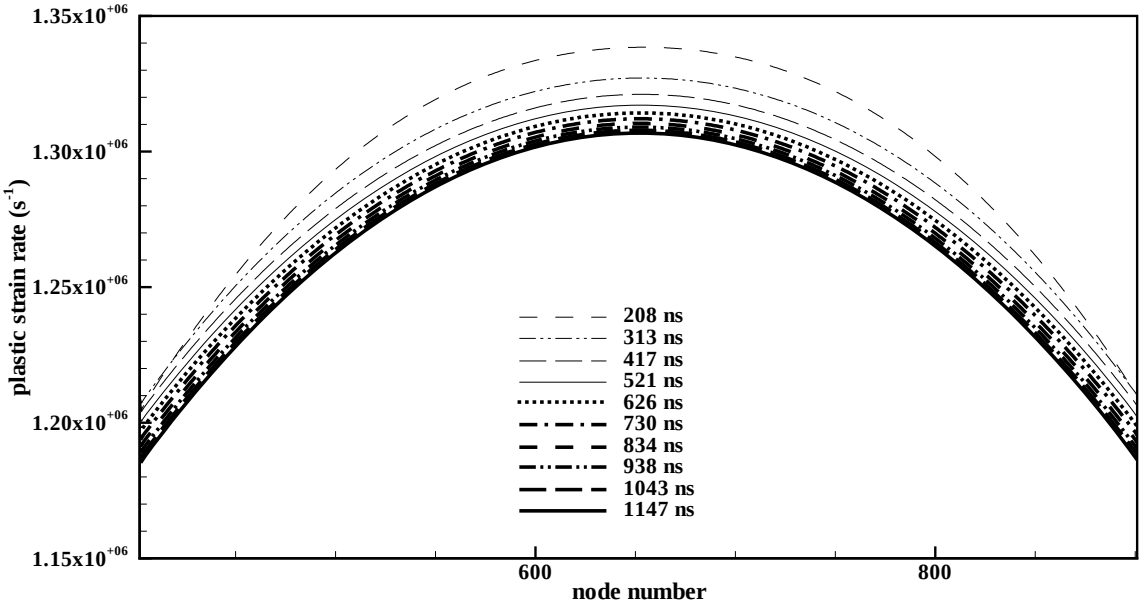

Figure 5.19: Nemat-Nasser/Isaacs model strain rate distribution for the simulation of shot SG0402 (T_0=22°C).

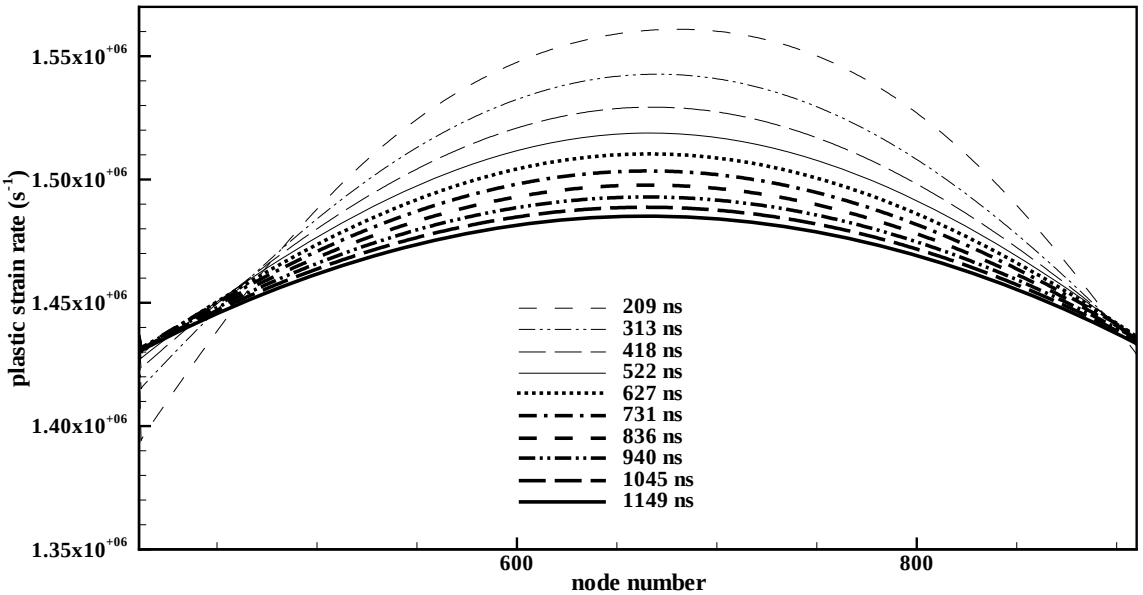

Figure 5.20: Nemat-Nasser/Isaacs model strain rate distribution for the simulation of shot SG0703 (T_0=584°C).

The same Nemat-Nasser/Isaacs model parameters are used to simulate shot SG0802. The computed pressure, normal stress and shear stress are plotted versus time in Figure 5.21. As in the simulated response of shot SG0802 using the Johnson/Cook model, the normal stress, pressure, and shear stress all drop at around 1120 *ns* when the simulated unloading wave arrives at the sample. For the Nemat-Nasser/Isaacs model, however, the shear stress quickly rebounds to a higher shear stress level than before the unloading wave arrived. Since the sample temperature, plotted versus time in Figure 5.22, never reaches the critical temperature (~13250^{o}C) and the melting temperature (also plotted versus time in Figure 5.22) does not explicitly affect the flow stress for this model (see Equation (5.27)), the flow stress will increase monotonically with decreasing temperature independent of the melting temperature. Therefore, the increase in flow stress (at ~1220 *ns*) is due to the temperature drop coinciding with the pressure drop.

The dip in the shear stress observed at 1120 *ns* also occurs in the simulations of shot SG0802 using a modified Nemat-Nasser/Isaacs model, which will be described in the next section (Section 5.2.3). The cause of the dip in the shear stress observed using both models will be discussed in detail in that section.

The normal and shear strains computed from the simulation of shot SG0802 using the Nemat-Nasser/Isaacs model are shown Figure 5.23. The difference in total accumulated shear strain between the middle of the sample and the edges grows slowly until the pressure drops. This difference is due to the slight non-uniformity of the shear strain rate across the sample shown in Figure 5.24, where the rate is higher in the middle of the sample than at the edges. When the pressure drops (at ~ 1120 *ns*) there is a sharp

increase in strain rate followed by a slower decrease as shown for the middle of the sample in Figure 5.25. The middle of the sample, after the pressure drops, is at a lower temperature (Figure 5.26) and a coinciding lower strain rate (Figure 5.24) than the edges of the sample. Therefore, after the pressure drops, the difference in total accumulated shear strain between the middle and edges of the sample slowly decreases as shown in Figure 5.23.

The sample temperature and melting temperature are given as a function of normalized volume in Figure 5.27. Direct comparisons of the simulated results to the experimental results will be made in Section 5.3.

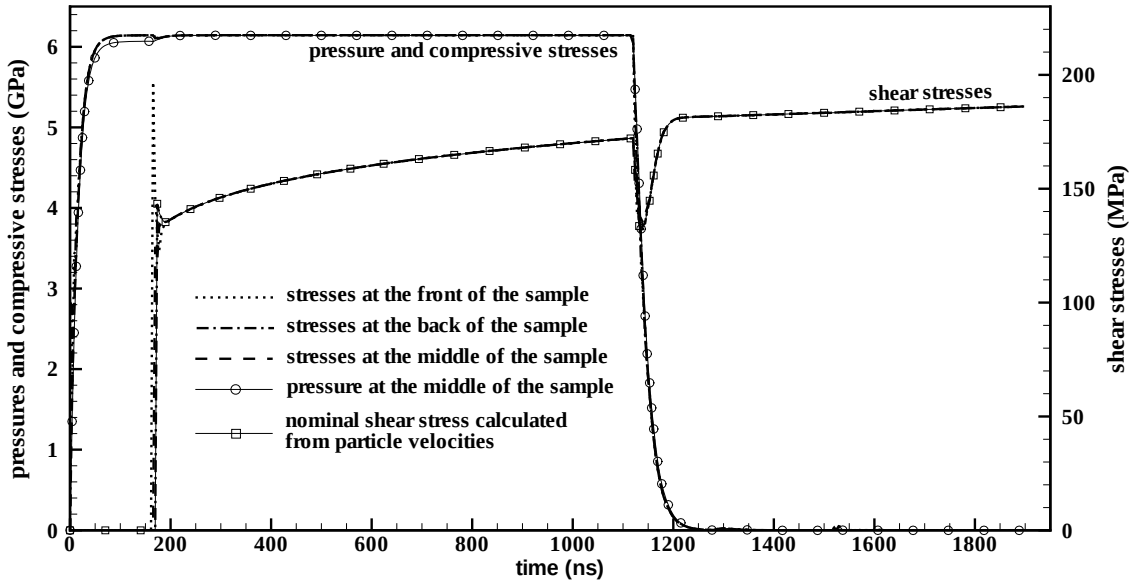

Figure 5.21: Pressures, compressive stresses and shear stresses simulated using the Nemat-Nasser/Isaacs model for shot SG0802 (T_0=582°C).

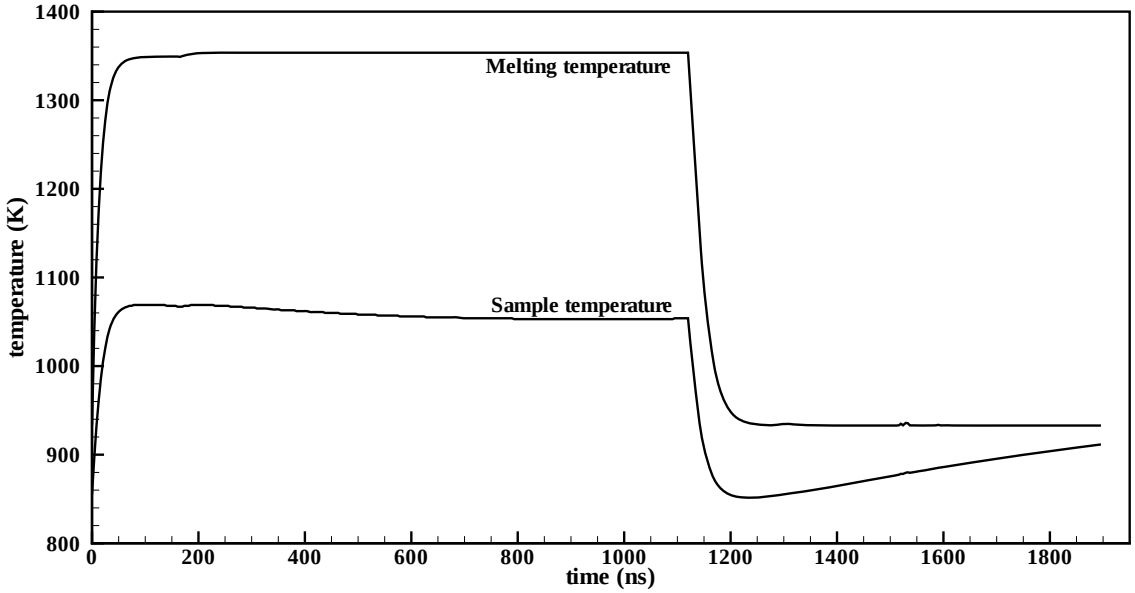

Figure 5.22: Sample temperature and melting temperature simulated using the Nemat-Nasser/Isaacs model for shot SG0802 (T_0=582°C) plotted versus time.

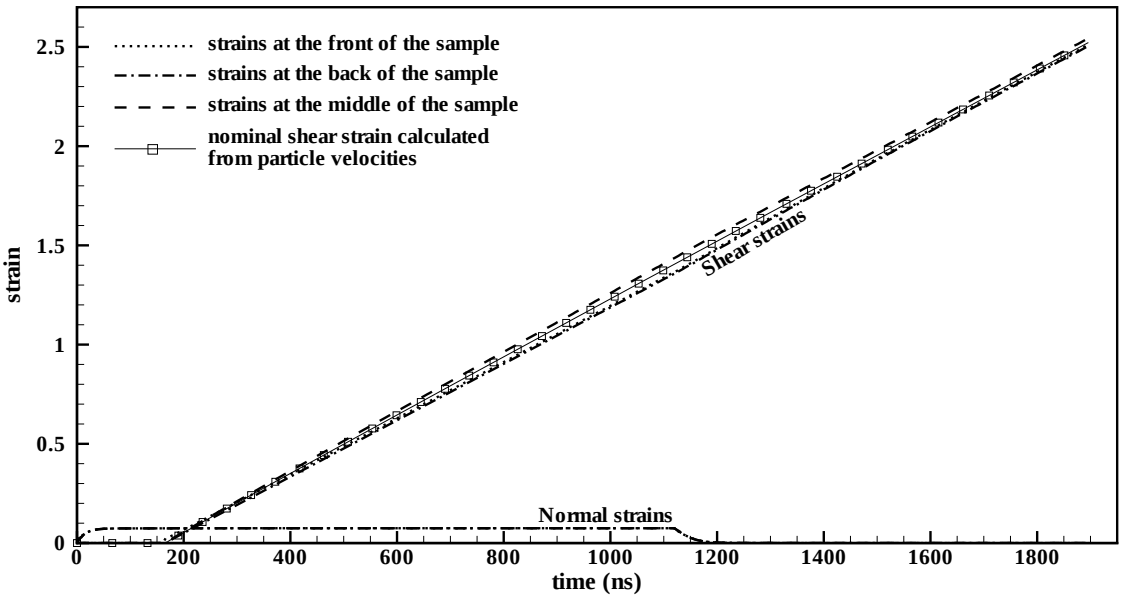

Figure 5.23: Normal and shear strains computed for the simulations of shot SG0802 (T_0=582°C) using the Nemat-Nasser/Isaacs model.

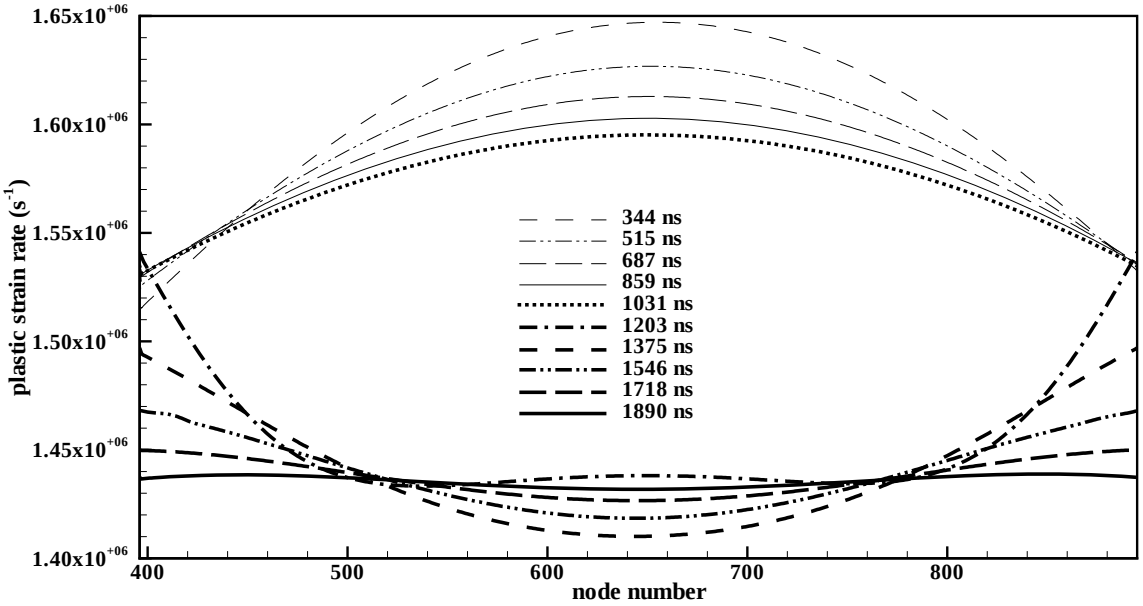

Figure 5.24: Nemat-Nasser/Isaacs strain rate profiles for the simulation of shot SG0802 (T_0=582°C).

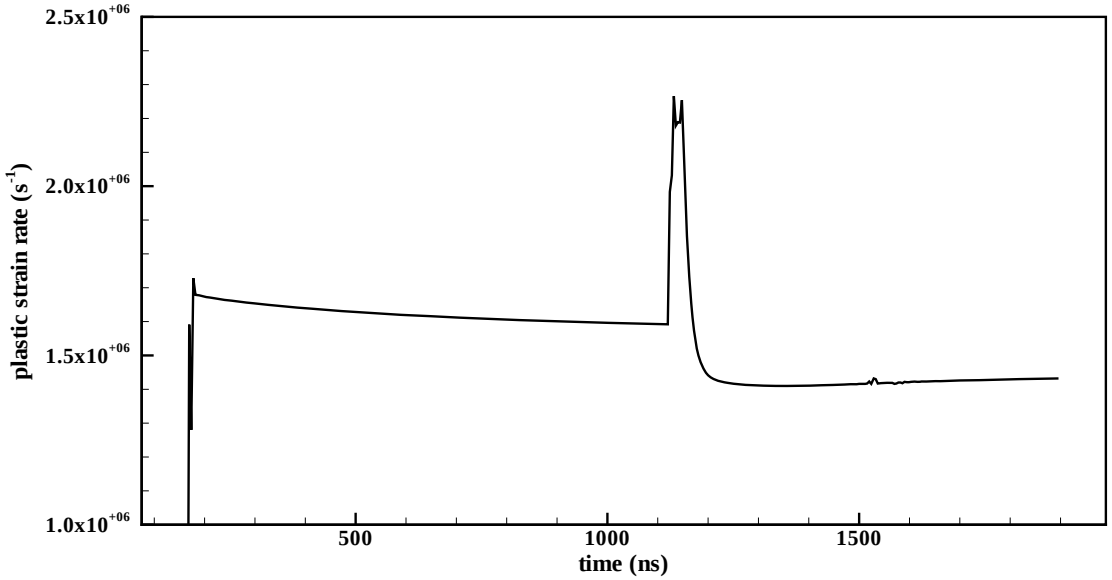

Figure 5.25: Nemat-Nasser/Isaacs strain rate at the middle of the sample for the simulation of shot SG0802 (T_0=582°C).

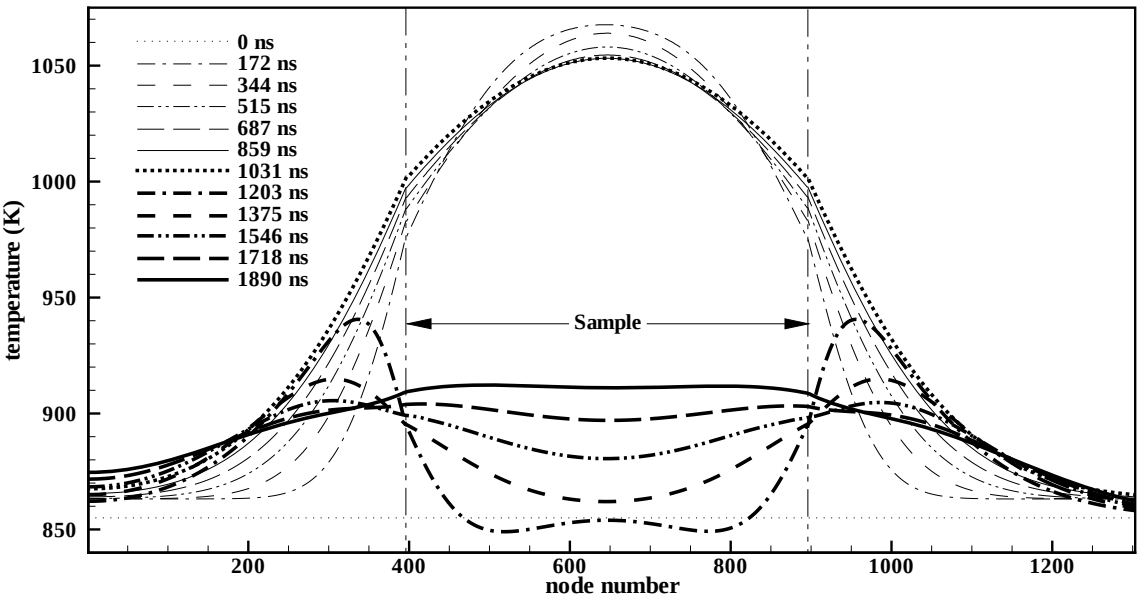

Figure 5.26: Nemat-Nasser/Isaacs model temperature distribution for the simulation of shot SG0802 (T_0=582°C).

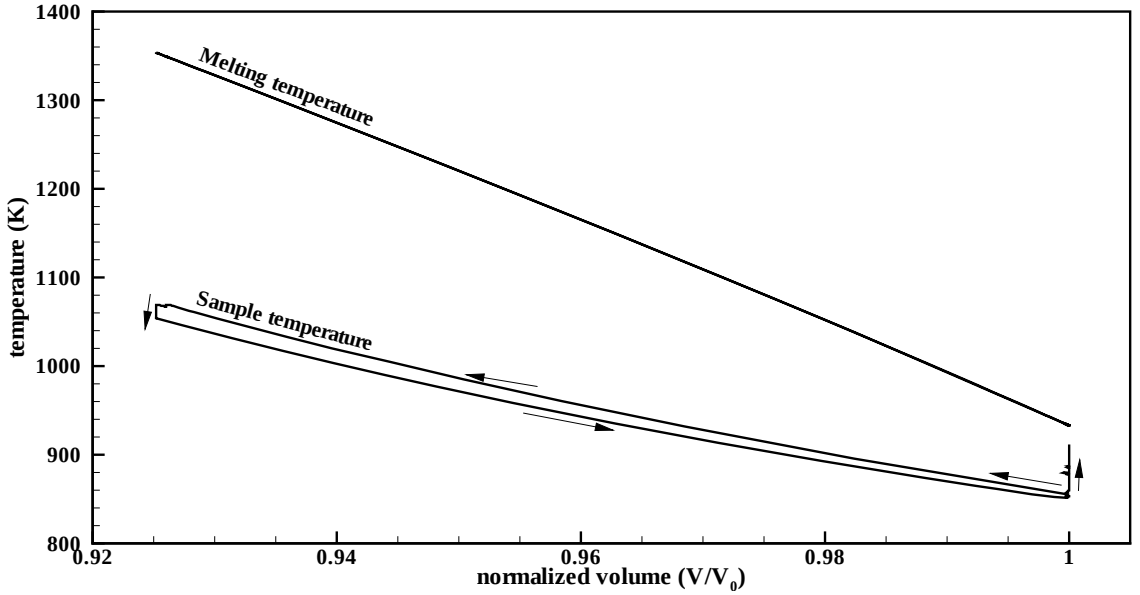

Figure 5.27: Sample temperature and melting temperature simulated using the Nemat-Nasser/Isaacs model for shot SG0802 (T_0=582°C) plotted versus normalize volume.

5.2.3 Modified Nemat-Nasser/Isaacs model

This model incorporates the mechanism of geometric softening. The basic idea of geometric softening is that as the sample is deformed, a slip system will rotate towards an orientation that is more favorable for slip, softening the sample. This softening effect competes with the strain hardening, becoming the dominate effect at large strains. In order to better simulate the softening observed in the experiments, the Nemat-Nasser/Isaacs model was modified to include strain softening as a part of the athermal stress. The modified athermal stress is taken to be

$$\tau_a = \tau_0 \frac{2\bar{\gamma}_p^n \bar{\gamma}_p^m}{\bar{\gamma}_p^n + \bar{\gamma}_p^m} \tag{5.28}$$

where *n*, the hardening parameter, is positive and *m*, the softening parameter, is negative. In this case, the smaller of the two strain terms, $\bar{\gamma}_p^n$ or $\bar{\gamma}_p^m$, dominates. With the addition of geometric softening, the plastic strain rate function for the modified Nemat-Nasser/Isaacs model becomes:

$$\Phi = \dot{\bar{\gamma}}_p = \dot{\gamma}_r \exp\left(\frac{-G_0}{kT} \left[1 - \left(\frac{\bar{\tau} - \tau_0 \dfrac{2\bar{\gamma}_p^n \bar{\gamma}_p^m}{\bar{\gamma}_p^n + \bar{\gamma}_p^m}}{\hat{\tau}} \right)^p \right]^q \right). \tag{5.29}$$

In the elevated temperature experiments, the sample stays at temperature for around two and one half hours prior to impact (Section 4.2.3). Therefore the structure of the aluminum sample tested at elevated temperatures is different than the aluminum sample tested at room temperature. At the time of impact, the sample tested at room temperature has a smaller average grain size than the sample in the elevated temperature

tests. This would explain the quick rise and sharp peak observed in shear response of the 22°C test and the wider peak for the 584°C test (Figure 4.30). Therefore it seems logical that the parameters used for hardening and softening (*n* and *m*) should be different for the room temperature and elevated temperature tests because the samples do not have the same structures at the time of impact. The parameters were chosen to fit the simulations to the experimental results. All of the parameters used to simulate the room temperature test (SG0402) were also used to simulate the elevated temperature tests (SG0703 and SG0802) except for the hardening and softening parameters (*n* and *m*). All of the parameters used for the modified Nemat-Nasser/Isaacs model are given in Table 5.3.

The pressures, normal stresses and shear stresses are plotted versus time in Figures 5.28 for the simulations of shots SG0402 and SG0703. The shear responses computed using the modified Nemat-Nasser/Isaacs model display considerably more softening than the unmodified model (Figure 5.14) for the simulation of both experiments.

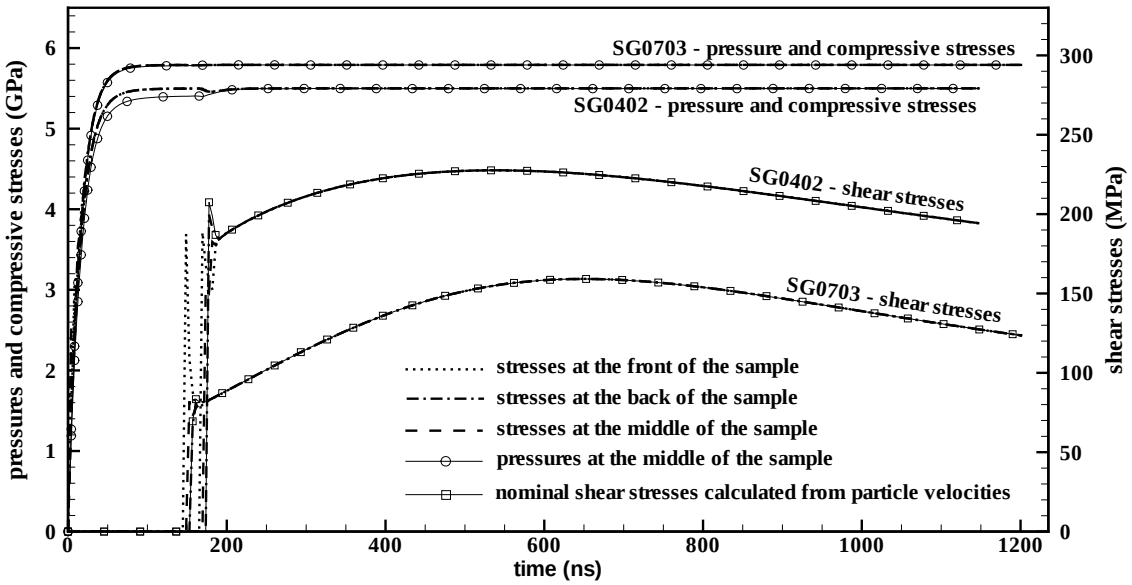

Figure 5.28: Pressures, compressive stresses and shear stresses simulated using the modified Nemat-Nasser/Isaacs model for shots SG0402 and SG0703.

The normal and shear strains computed from the simulations of shots SG0402 and SG0703 are shown in Figure 5.29 and Figure 5.30, respectively. The temperature fields are shown in Figures 5.31 and 5.32 and the strain rate distributions across the sample are shown in Figures 5.33 and 5.34 for shots SG0402 and SG0703, respectively.

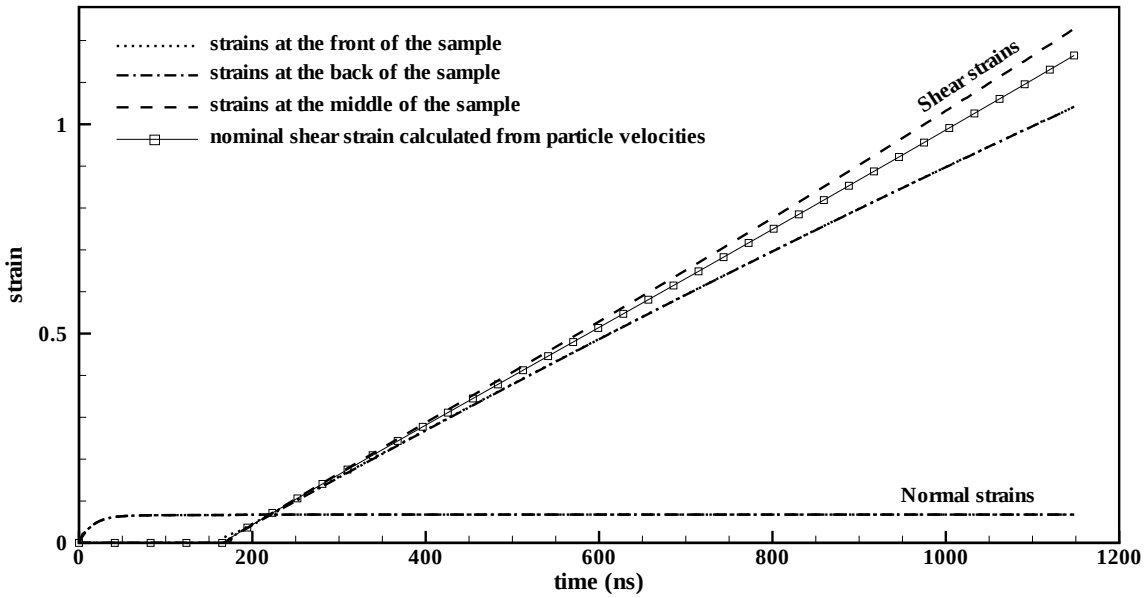

Figure 5.29: Normal and shear strains computed for the simulations of shot SG0402 (T_0=22°C) using the modified Nemat-Nasser/Isaacs model.

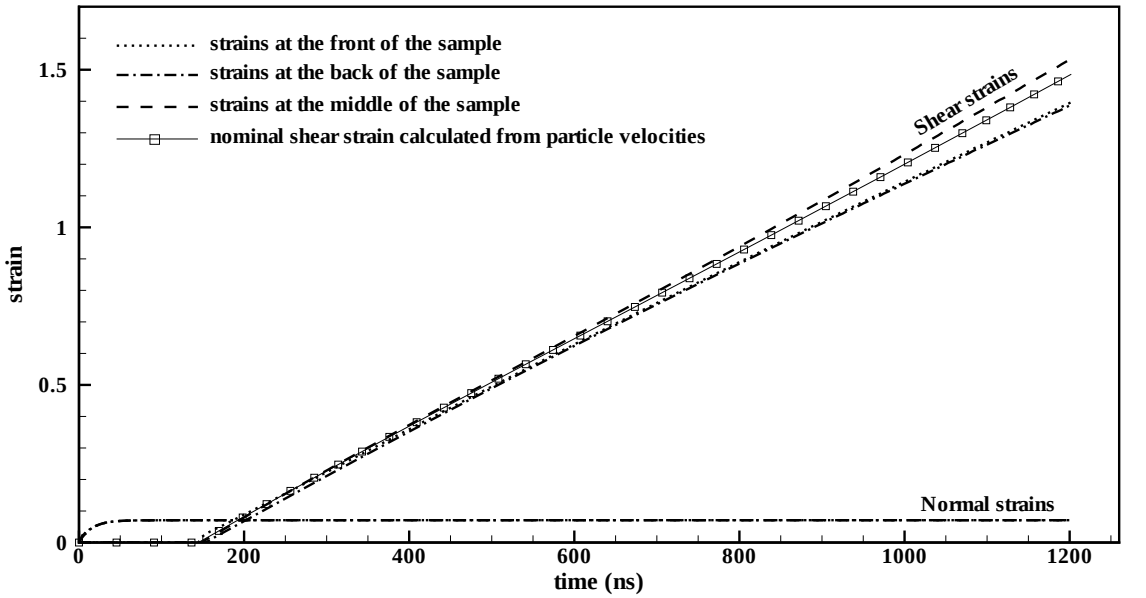

Figure 5.30: Normal and shear strains computed for the simulations of shot SG0703 (T_0=584°C) using the modified Nemat-Nasser/Isaacs model.

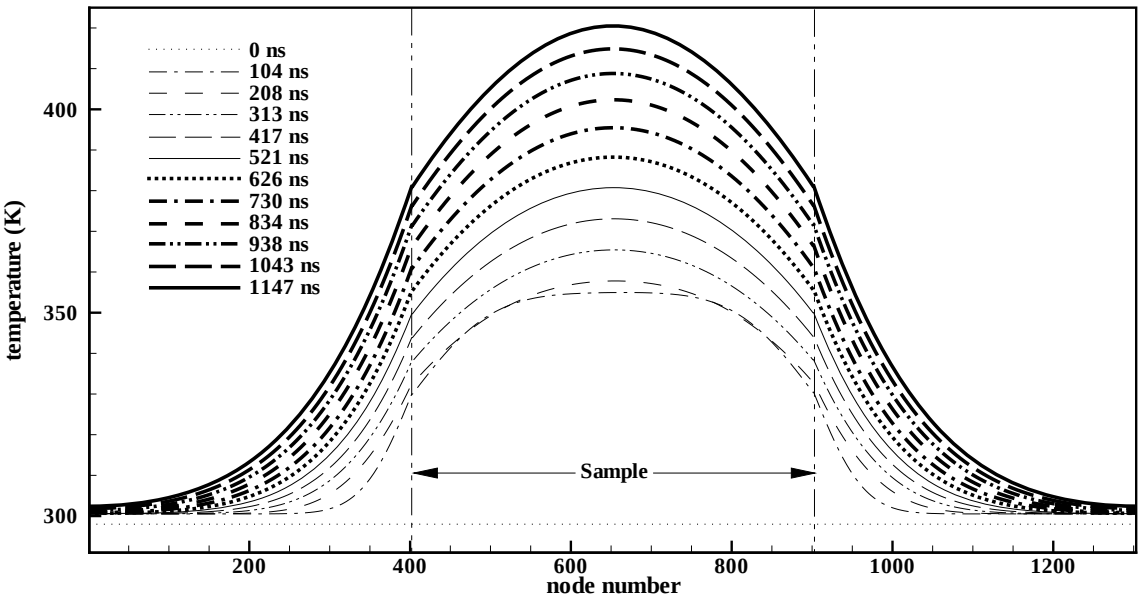

Figure 5.31: The modified Nemat-Nasser/Isaacs model temperature distribution for the simulation of shot SG0402 (T_0=22°C).

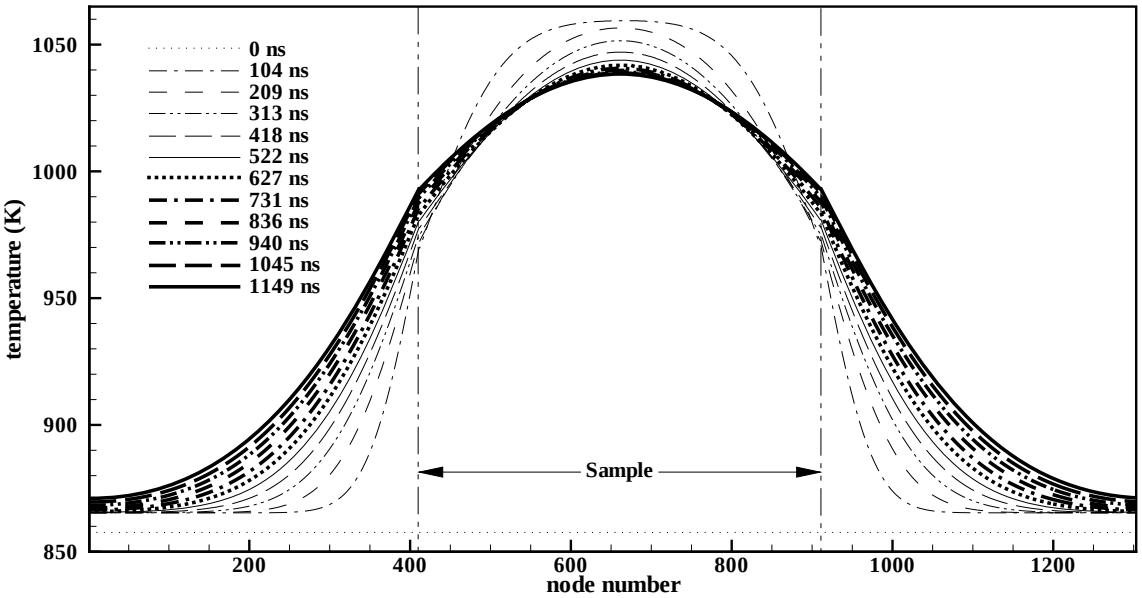

Figure 5.32: The modified Nemat-Nasser/Isaacs model temperature distribution for the simulation of shot SG0703 (T_0=584°C).

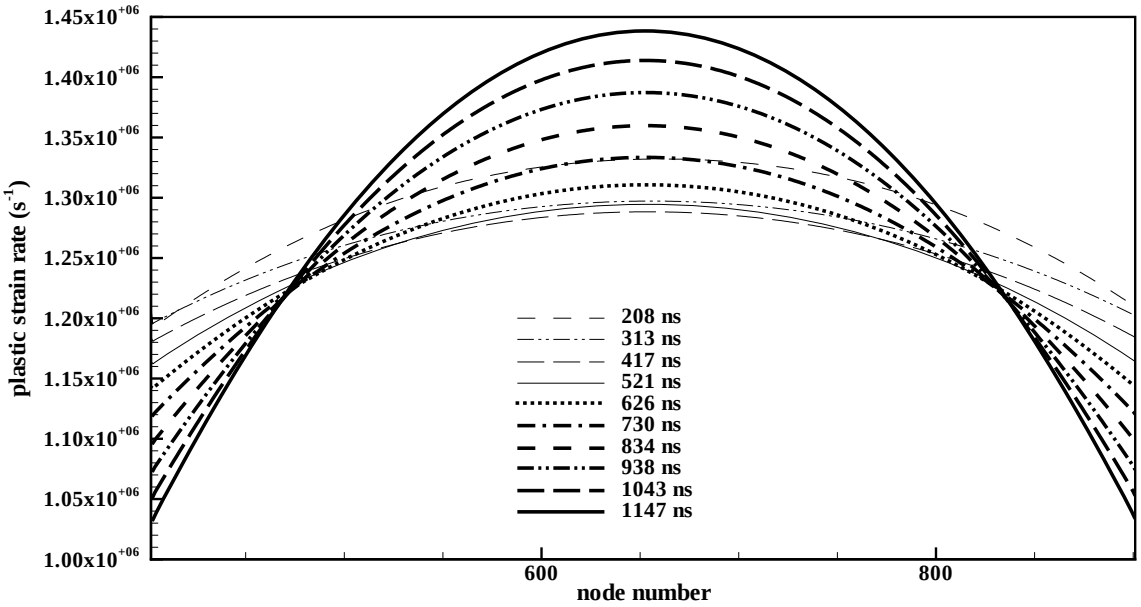

Figure 5.33: The modified Nemat-Nasser/Isaacs model strain rate distribution for the simulation of shot SG0402 (T_0=22°C).

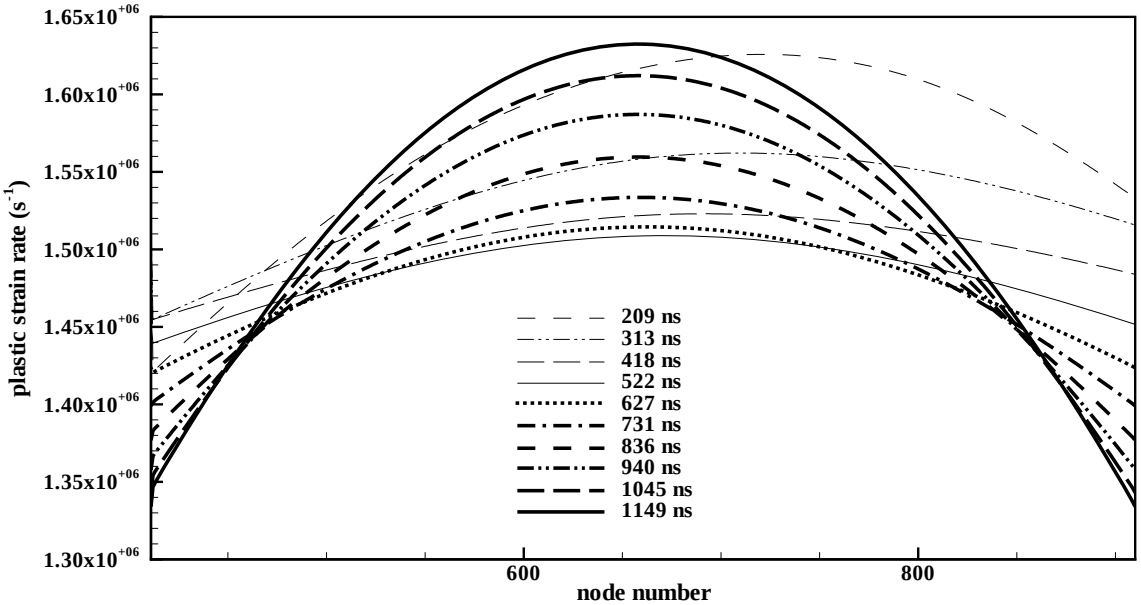

Figure 5.34: The modified Nemat-Nasser/Isaacs model strain rate distribution for the simulation of shot SG0703 (T_0=584°C).

Shot SG0802 is simulated using the same set of parameters used in the simulation of shot SG0703 with the modified Nemat-Nasser/Isaacs model. The computed pressure, normal stress, and shear stress are plotted versus time in Figure 5.35. Considerable softening is observed in the computed shear response. At the time of the pressure drop (~1120 *ns*), there is a dip in the shear stress before it recovers to a slightly higher stress level than before the drop. The shear stress in the simulated response then continues to decrease but at a slower rate than that observed prior to the pressure drop.

The dip in the shear stress, observed at the time of the pressure drop in the simulations of SG0802 using both the modified and unmodified versions of the Nemat-Nasser/Isaacs models, can be better understood by examining the stress state in the sample. In Figure 5.36, the first Piola-Kirchhoff stresses (Σ_{11}, Σ_{22}, Σ_{33}, Σ_{21}), the deviatoric stresses (S_{11}, S_{22}, S_{33}, S_{21}), the pressure, and the effective shear stress $\bar{\tau}$ at the middle of the sample, simulated using the modified Nemat-Nasser/Isaacs model, are plotted as a function of time. Note that the Σ_{21} value has been referred to as the "shear stress" throughout this chapter and is, by definition, equal to S_{21}. The stress trajectory of the middle of the sample is plotted in Figure 5.37 where the abscissa is $(S_{11}\text{-}S_{22})/2$ and the ordinate is S_{21}.

In the stress trajectory, the $(S_{11}\text{-}S_{22})/2$ value jumps up at the arrival of the longitudinal wave and then quickly decreases and settles at approximately 6 MPa prior to the arrival of the shear wave. At the arrival of the shear wave, the S_{21} value jumps up and $(S_{11}\text{-}S_{22})/2$ becomes nearly zero. The S_{21} value then increases gradually up to

approximately 162 MPa and then decreases to approximately 130 MPa before the arrival of the longitudinal unloading wave.

After the arrival of the shear wave (in Figure 5.36), the effective stress ($\bar{\tau}$) is equal to S_{21} and Σ_{21} until the arrival of the longitudinal unloading wave (see Figure 5.36). When the longitudinal unloading wave arrives at the sample, the values for Σ_{11}, Σ_{22}, Σ_{33} and the pressure all drop. However, Σ_{11} drops more quickly than the pressure and therefore S_{11} ($=\Sigma_{11}-P$) also decreases and becomes negative. As observed in Figure 5.36, S_{22} and S_{33} both increase approximately half the amount that S_{11} decreases and the trace of the deviatoric stress remains equal to zero. The changes observed in the deviatoric stresses leads to a spike in the effective shear stress, $\bar{\tau} = \sqrt{S_{ij}S_{ij}/2}$. The plastic strain rate function, for both the modified and unmodified versions of the Nemat-Nasser/Isaacs constitutive model (Equations (5.29) and (5.27) respectively), decrease with decreasing temperature and increase with increasing effective shear stress, $\bar{\tau}$. Despite the large temperature drop (see Figure 5.42) due to the pressure drop, there is a spike in the plastic strain rate (Figure 5.38), which implies that the spike in the effective shear stress has a larger effect. The intrinsic response of the pressure-shear plate impact experiment dictates that, for a given loading and constitutive response, if the nominal shear stress of the sample decreases then the shear strain rate increases. This can be observed by reviewing the equations that are used to calculate the nominal shear stress (Equation (2.20)) and the nominal shear strain rate (Equation (2.23)) from the experimentally measured transverse free-surface velocity. An increase observed in the transverse free-surface velocity gives an increase in shear stress and a decrease in shear strain rate. Therefore, the spike in shear strain rate results in a dip in shear stress (Σ_{21}).

Looking at the stress trajectory (Figure 5.37), the $(S_{11}\text{-}S_{22})/2$ value jumps to approximately negative 150 MPa when the unloading longitudinal wave arrives, while S_{21} is at approximately 126 MPa. This stress state is off the yield surface. The values for S_{21} and $(S_{11}\text{-}S_{22})/2$ both decrease as the stress state returns quickly (within 1 *ns*) to the yield surface. The stress state then starts to move along the yield surface towards the ordinate. The $(S_{11}\text{-}S_{22})/2$ again jumps to a larger negative value. This is due to the ringing down of normal stress in the sample, which is analogous to the ringing up of normal stress described in Section 2.1. Due to the impedance mismatch between the sample and the target plates, the normal stress in the sample is unloaded in small jumps that occur approximately every 4 *ns*. Every time there is an unloading jump, the $(S_{11}\text{-}S_{22})/2$ value decreases sharply and the stress state jumps off the yield surface and a corresponding spike is observed in the S_{11}, S_{22}, S_{33}, and $\bar{\tau}$ curves shown in Figure 5.36. After six or seven unloading jumps, the stress state follows the yield surface until the $(S_{11}\text{-}S_{22})/2$ value is nearly zero again. As the stress state moves along the yield surface, S_{11}, S_{22}, and S_{33} all move towards zero (see Figure 5.36) and the effective shear stress, $\bar{\tau}$, again becomes equal to $S_{21}(=\Sigma_{21})$.

The normal and shear strains computed from the simulation of shot SG0802 using the modified Nemat-Nasser/Isaacs model are given in Figure 5.39. The difference in total accumulated shear strain between the edges and the middle of the sample slowly diverge until the pressure drop occurs. They then diverge at an even slower rate. Figure 5.40 gives the shear strain rate distribution across the sample at various times. The strain rate is getting higher in the middle of the sample and lower at the edges of the sample

until the pressure drop occurs. After the pressure drops, the strain becomes more uniform across the sample. The temperature distribution across the sample, given in Figure 5.41 at various times, does not show a growing difference between the middle of the sample and the edges of the sample prior to the pressure drop. Therefore, the growing difference in strain rate between the middle and the edges of the sample prior to the pressure drop is not due mainly to the temperature distribution as has been the case in the simulations with the previous models. For the modified Nemat-Nasser/Isaacs model the strain hardening/softening is having a larger effect on the strain rate. The sample temperature and the melting temperature are given as function of time in Figure 5.42 and as a function of normalized volume in Figure 5.43.

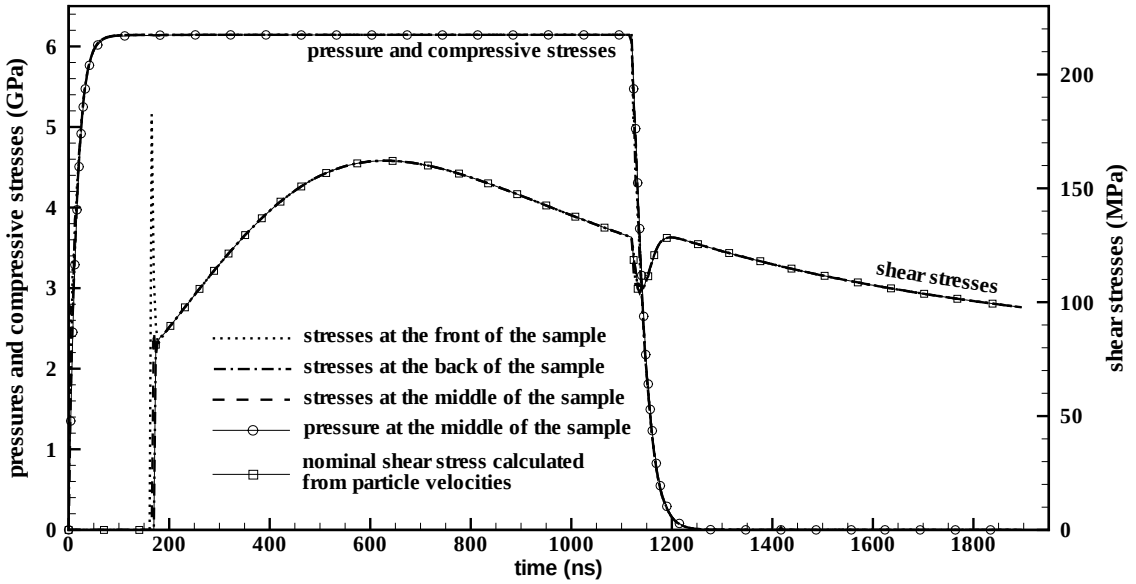

Figure 5.35: Pressures, compressive stresses and shear stresses simulated using the modified Nemat-Nasser/Isaacs model for shot SG0802 (T_0=582°C).

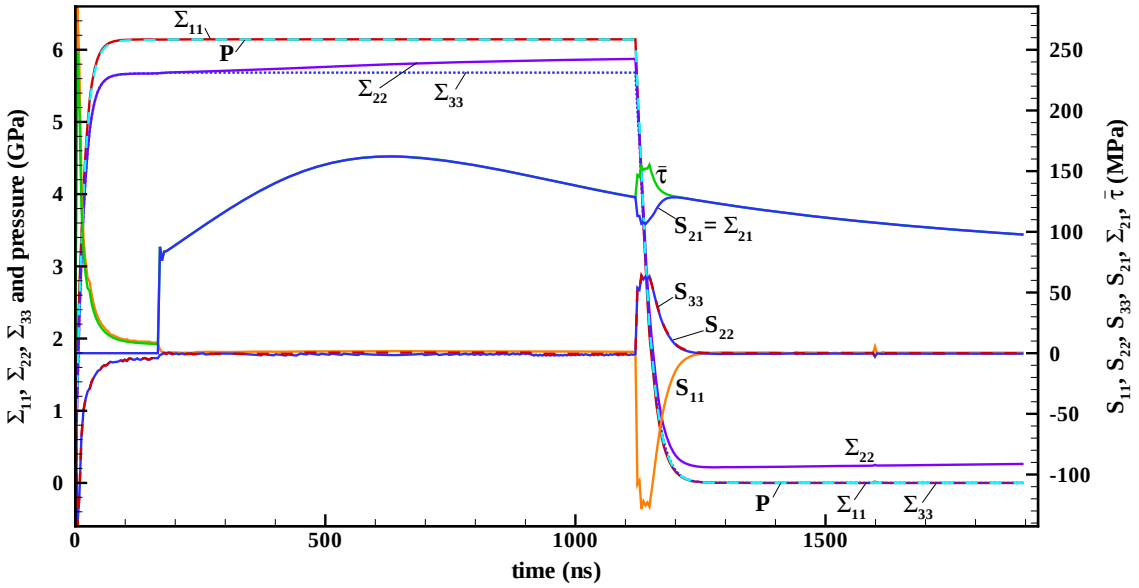

Figure 5.36: Stresses simulated using the modified Nemat-Nasser/Isaacs model for shot SG0802.

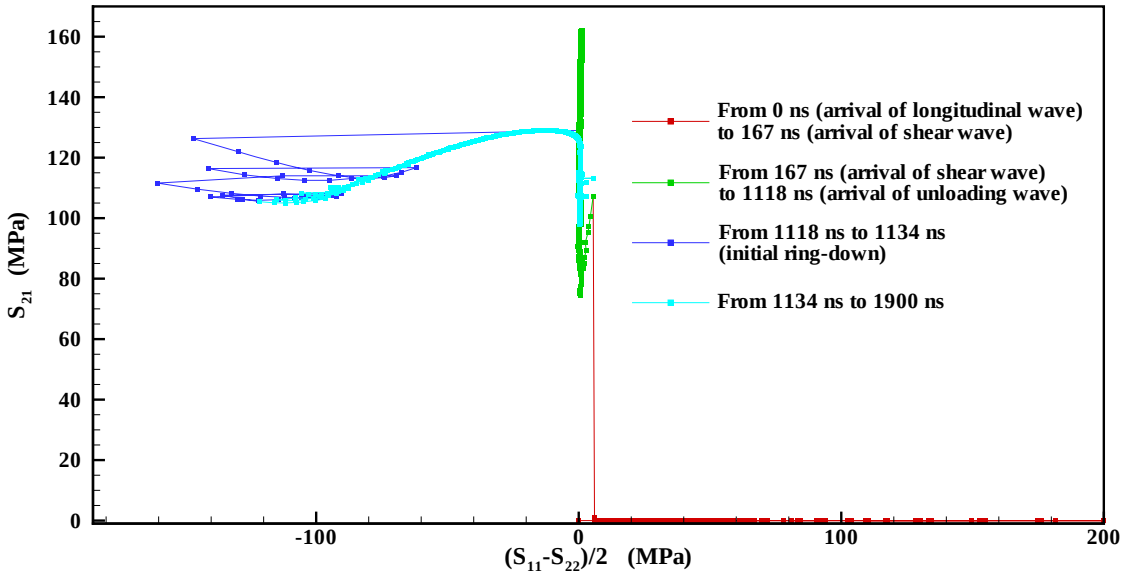

Figure 5.37: Stress trajectory for the simulation of shot SG0802 using the modified Nemat-Nasser/Isaacs model. (The square symbols are plotted every 0.4 *ns*)

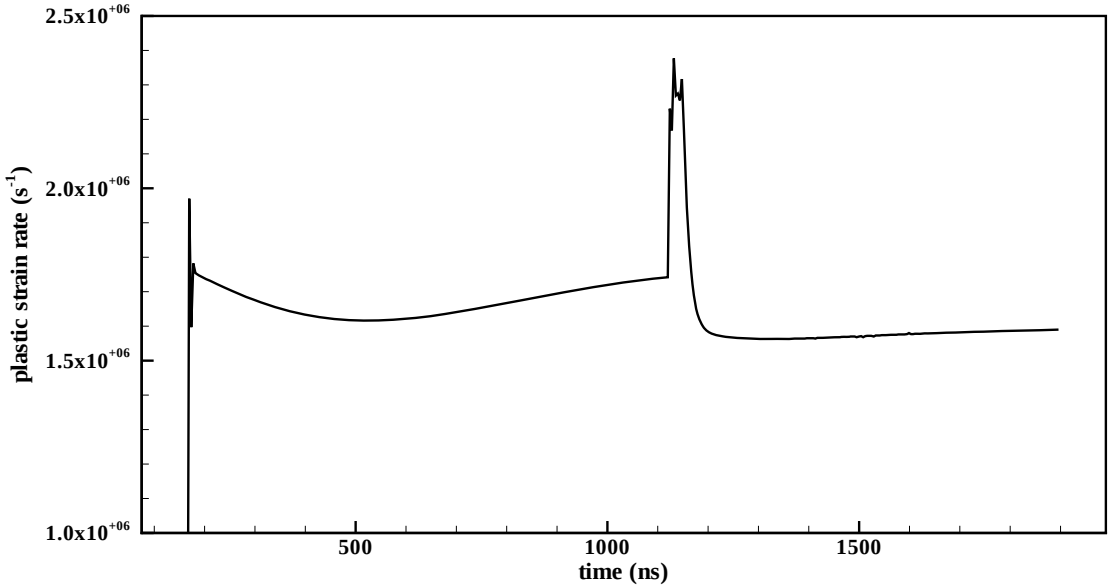

Figure 5.38: Strain rate at the middle of the sample for the simulation of shot SG0802 (T_0=582°C) using the modified Nemat-Nasser/Isaacs model.

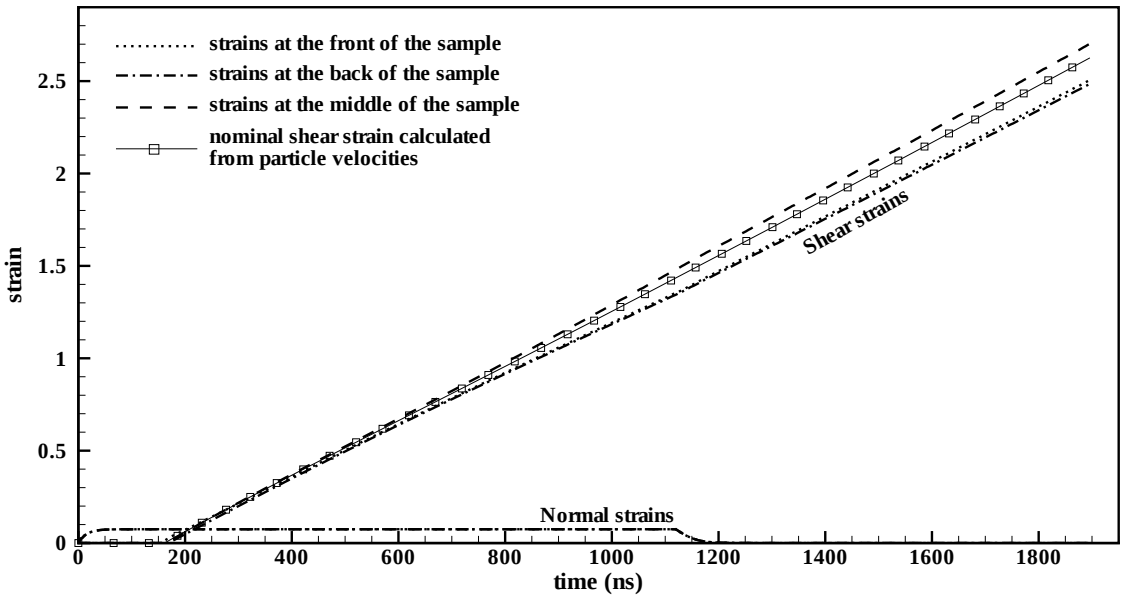

Figure 5.39: Normal and shear strains computed for the simulations of shot SG0802 (T_0=582°C) using the modified Nemat-Nasser/Isaacs model.

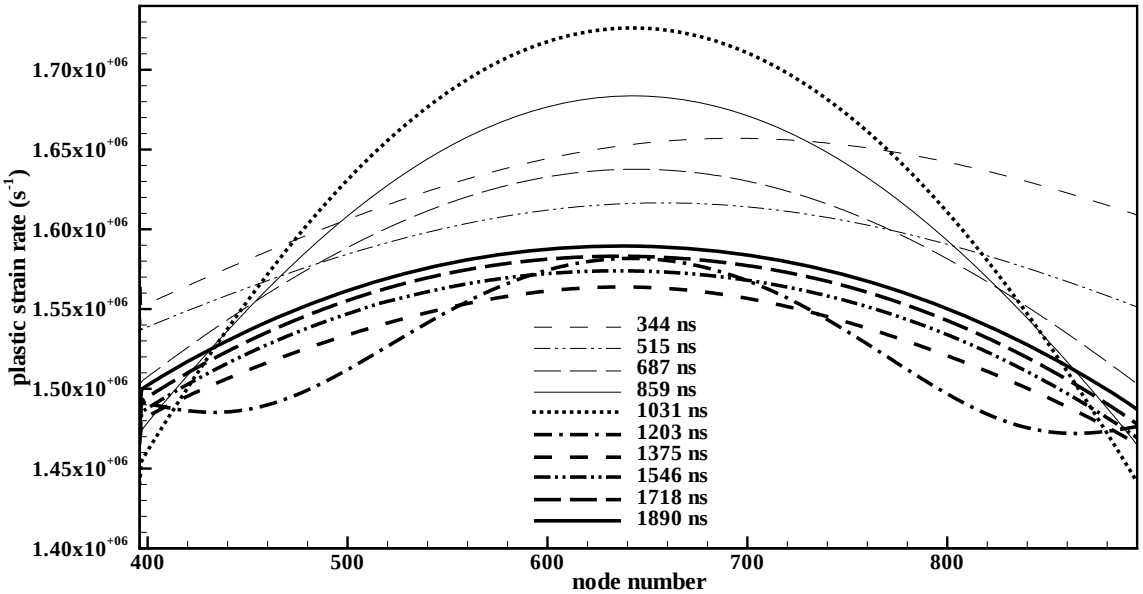

Figure 5.40: The modified Nemat-Nasser/Isaacs strain rate profiles for the simulation of shot SG0802 (T_0=582^{o}C).

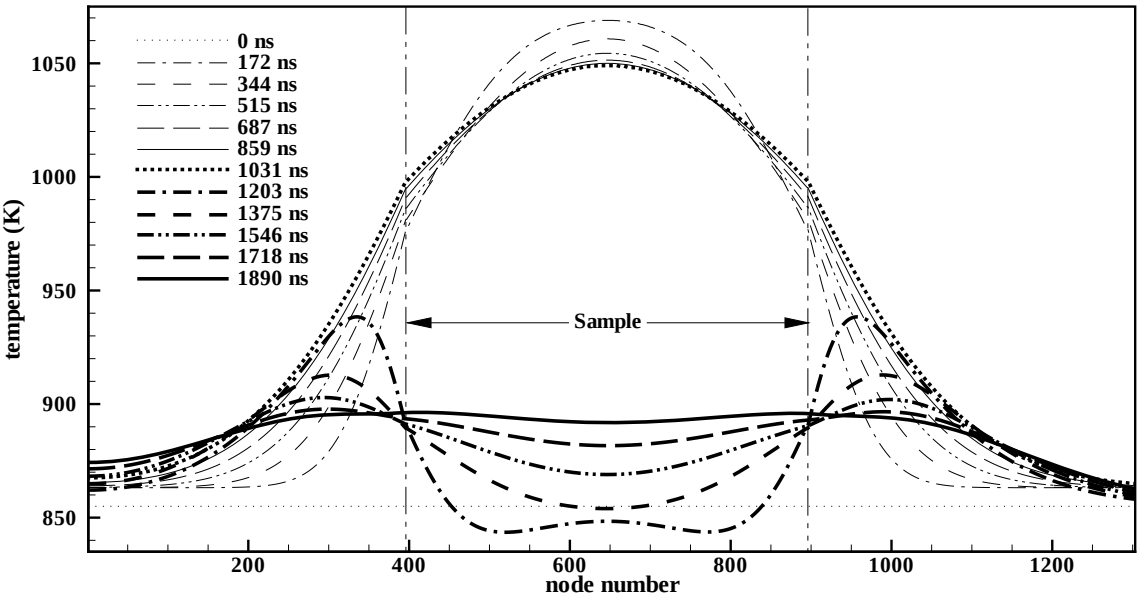

Figure 5.41: The modified Nemat-Nasser/Isaacs model temperature distribution for the simulation of shot SG0802 (T_0=582^{o}C).

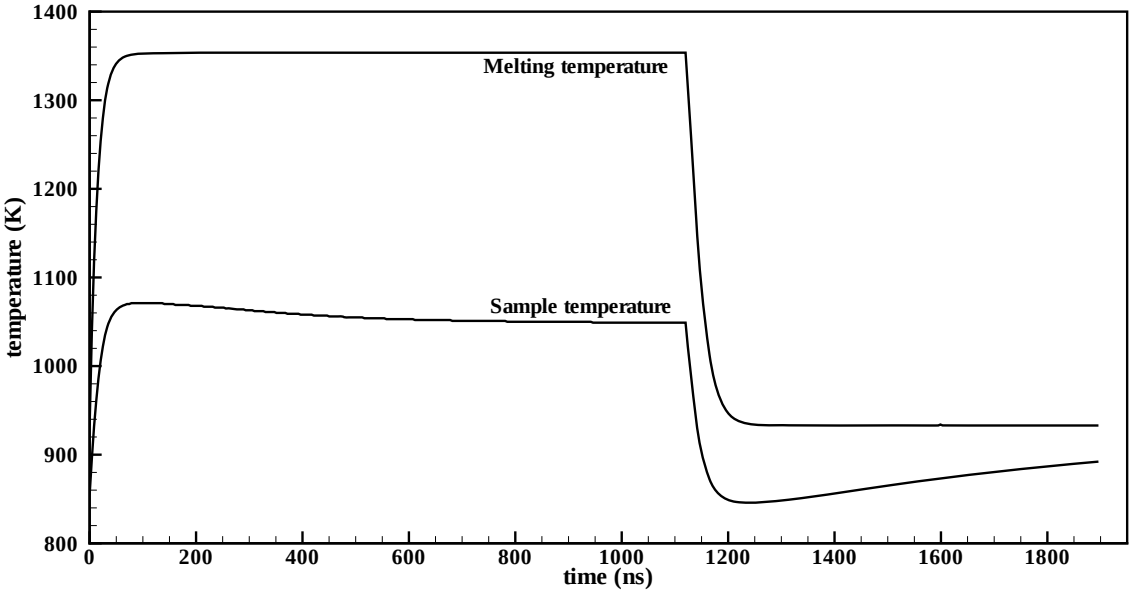

Figure 5.42: Sample temperature and melting temperature simulated using the modified Nemat-Nasser/Isaacs model for shot SG0802 (T_0=582°C) plotted versus time.

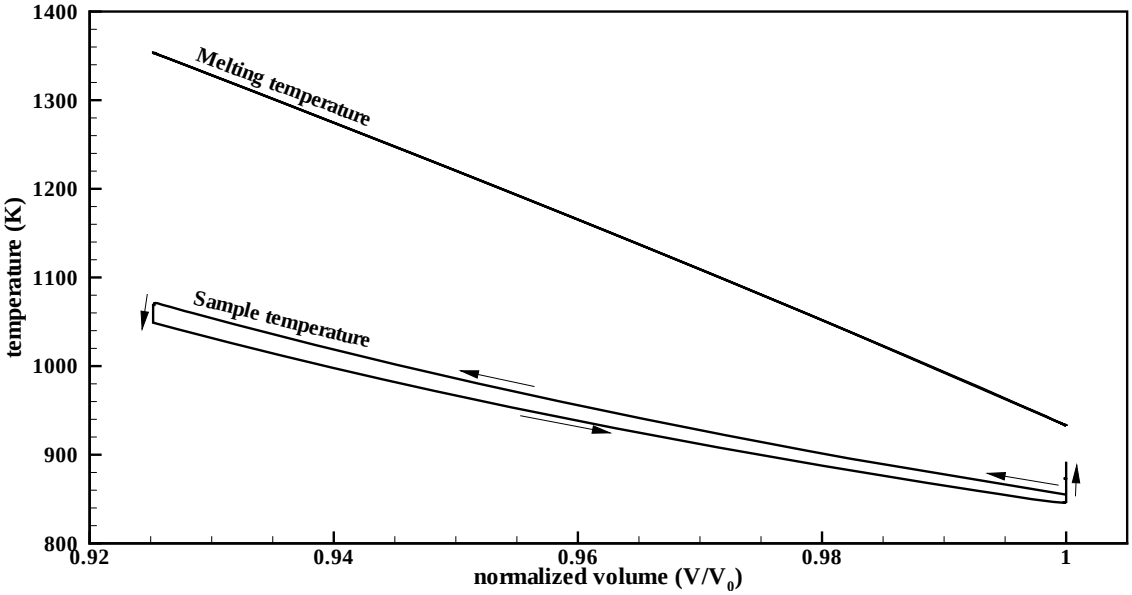

Figure 5.43: Sample temperature and melting temperature simulated using the modified Nemat-Nasser/Isaacs model for shot SG0802 (T_0=582°C) plotted versus normalize volume.

5.3 Comparison of simulations with experimental results

The normal stresses, computed at the middle of the sample, are plotted versus time for all three constitutive models used in the simulations of shots SG0402 and SG0703 along with the normal stresses measured in the experiments in Figure 5.44. To clarify Figure 5.44, it should be noted that the simulated normal response is nominally the same for all three models. In other words, the simulated normal stresses for all three models lie on top of one another for a given shot simulation.

All three models accurately predict the maximum compressive stress level for both shots. The simulated risetime of the normal stress, however, is notably shorter than that observed in the experiments. In Chapter 4, it was shown that the response of the tungsten carbide target plates is not linear in the high stress regime while at elevated temperatures. The nonlinear response of the target plates in shot SG0703 (T_0=584^{o}C) is evidenced in the relatively large risetime of the normal stress. For shot SG0402, conducted at room temperature, the target plates respond nearly linearly in this stress regime and the normal stress rises notably quicker than in shot SG0703. In the simulations, all target plates were taken to respond linearly.

The shear stresses for the simulations of shots SG0402 and SG0703 are plotted against the nominal shear strain with the experimental results in Figure 5.45 for all three constitutive models. Both the Johnson/Cook and Nemat-Nasser/Isaacs models can predict the approximate shear stress levels of the room temperature (SG0402) and elevated temperature (SG0703) tests with empirically fit parameters. However, neither

model can capture the hardening/softening observed in the experimental results. Using the modified Nemat-Nasser/Isaacs model with the addition of geometric softening, the simulation more accurately predicts the shear response.

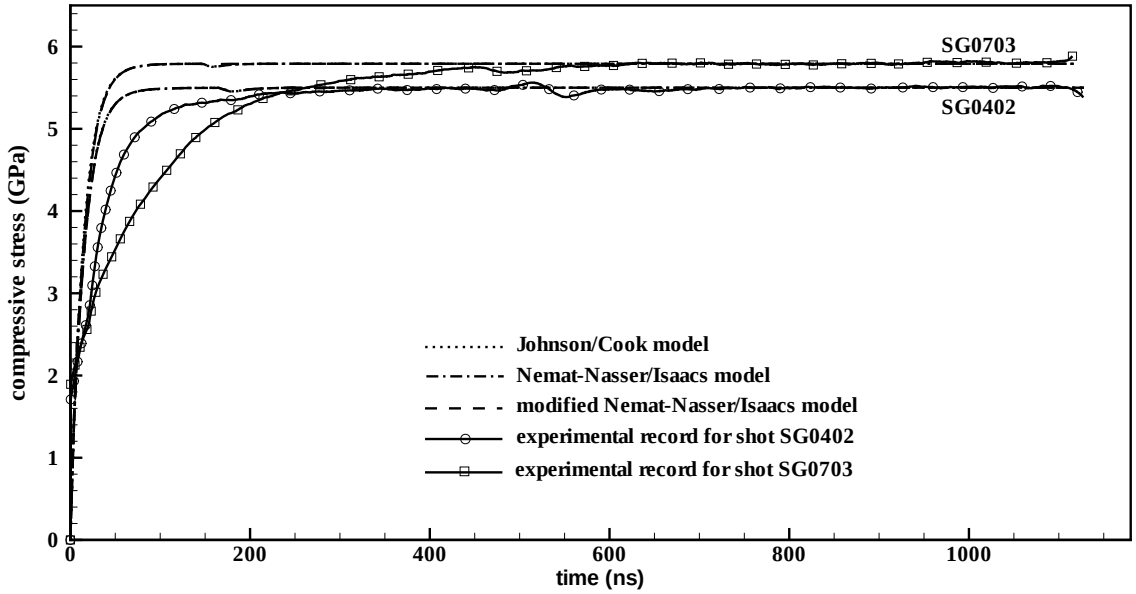

Figure 5.44: Experimental and simulated compressive stresses for shots SG0402 (T_0=22°C) and SG0703 (T_0=584°C).

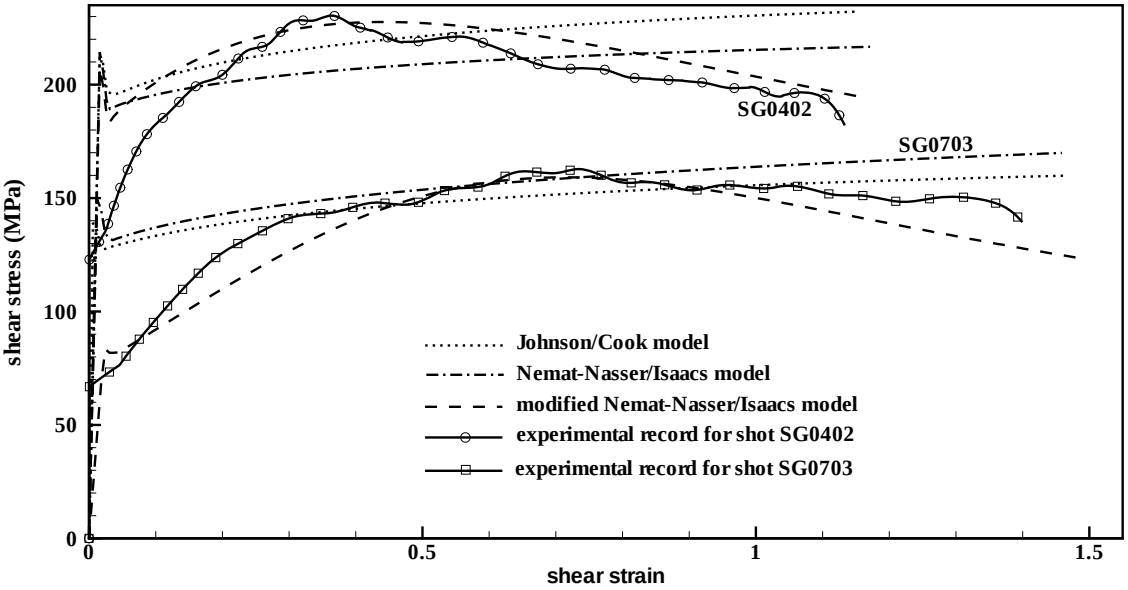

Figure 5.45: Experimental and simulated shear responses for shots SG0402 (T_0=22°C) and SG0703 (T_0=584°C).

The normal stresses computed for all three constitutive models in the simulations of shot SG0802 are plotted versus time with the experimental results in Figure 5.46. Similar to the comparison of normal stresses for shot SG0703, the risetimes for the simulations is markedly shorter than that measured in the experiment. In both the experimental and simulated results, the shape of the unloading wave is the same as the initial loading wave. Thus, when the unloading wave arrives at the sample (~1120 ns) the simulated normal stress drops faster than the experimentally measured normal stress.

The shear stress versus nominal shear strain curves simulated for all three constitutive models are plotted with the experimental response in Figure 5.47. The Johnson/Cook model roughly predicts the shear stress level prior to the pressure drop (at a strain ~1.4), but fails to capture the hardening/softening observed experimentally. At the time of the pressure drop, the simulated response using the Johnson/Cook model drops sharply to approximately 115 MPa and then decreases slowly. After the drop, the simulation appears to accurately predict the experimental result. However, since the simulation does not accurately predict the initial softening observed in the experiment (starting at a strain of around 0.8) it is merely a coincidence that the agreement is good after the pressure drops.

The Nemat-Nasser/Isaacs model roughly predicts the shear stress level observed in the experiment, but fails to capture the hardening/softening observed in the experimental response. After the dip in shear stress associated with the pressure drop, the shear stress rebounds to a higher stress level and continues to harden.

The modified Nemat-Nasser/Isaacs model, using the empirically fit hardening and softening parameters, can accurately predict the experimental result prior to the pressure drop. After the dip in shear stress associated with the pressure drop, the simulated shear stress rebounds to a slightly higher stress level and then continues decreasing, but at a rate slower than observed prior to the pressure drop. After reaching a peak, the experimental shear stress decreases until the time of the pressure drop (corresponding to a strain ~1.4). The experimental result does not show a dip in shear stress associated with the pressure drop or an increase in shear stress at that time; however, the shear stress does begin to decrease less quickly after the time of the pressure drop and that response is predicted using the modified Nemat-Nasser/Isaacs model.

The dip observed in the simulated shear stress was discussed in Section 5.2.3. It was shown that sharp decreases in normal stress resulted in the sharp increase in plastic strain rate and a subsequent decrease in shear stress (Σ_{21}). However, due to the nonlinear response of the target plates, the longitudinal unloading wave in the experiment is not sharp (see Figure 5.46). Therefore, the absence of a dip in the experimental shear stress is consistent with the more gradual unloading of the normal stress. This claim is confirmed by a simulation of shot SG0802, using the modified Nemat-Nasser/Isaacs model, but giving the prescribed normal impact velocity a representative risetime. The normal and shear stresses for that simulation are plotted versus time in Figure 5.48. The normal stress increases and decreases more gradually than the previous simulations and the dip in the shear stress has become much less pronounced.

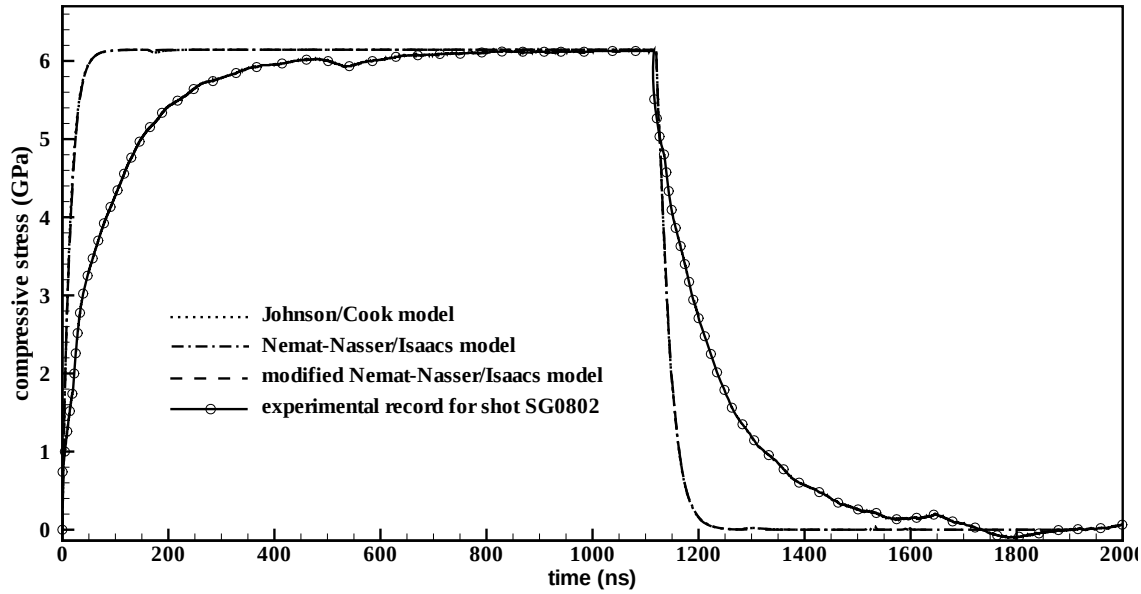

Figure 5.46: Experimental and simulated compressive stresses for shot SG0802 (T_0=582°C).

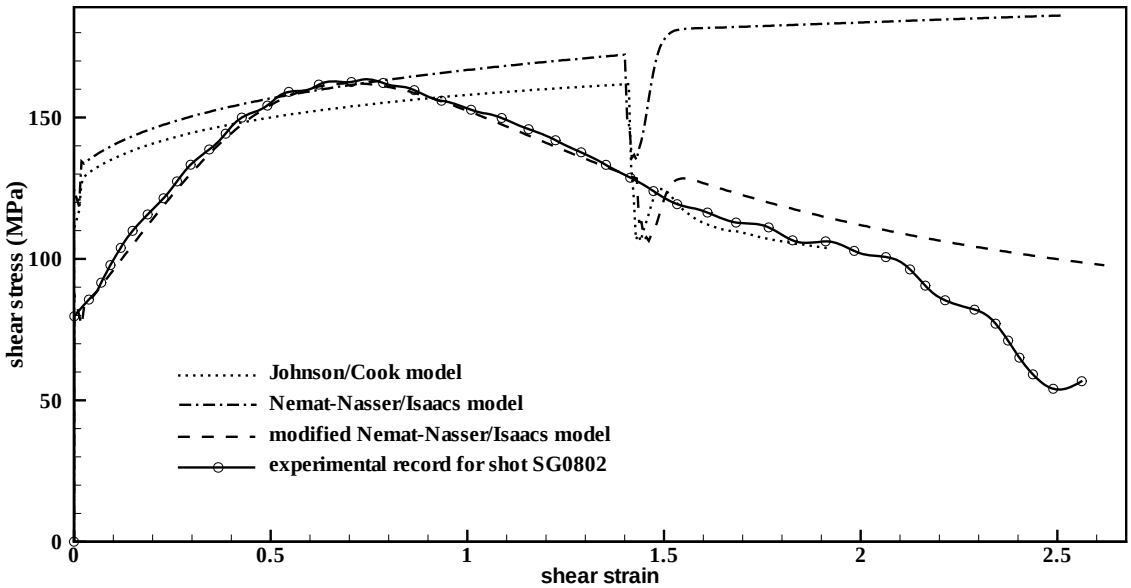

Figure 5.47: Experimental and simulated shear responses for shot SG0802 (T_0=582°C).

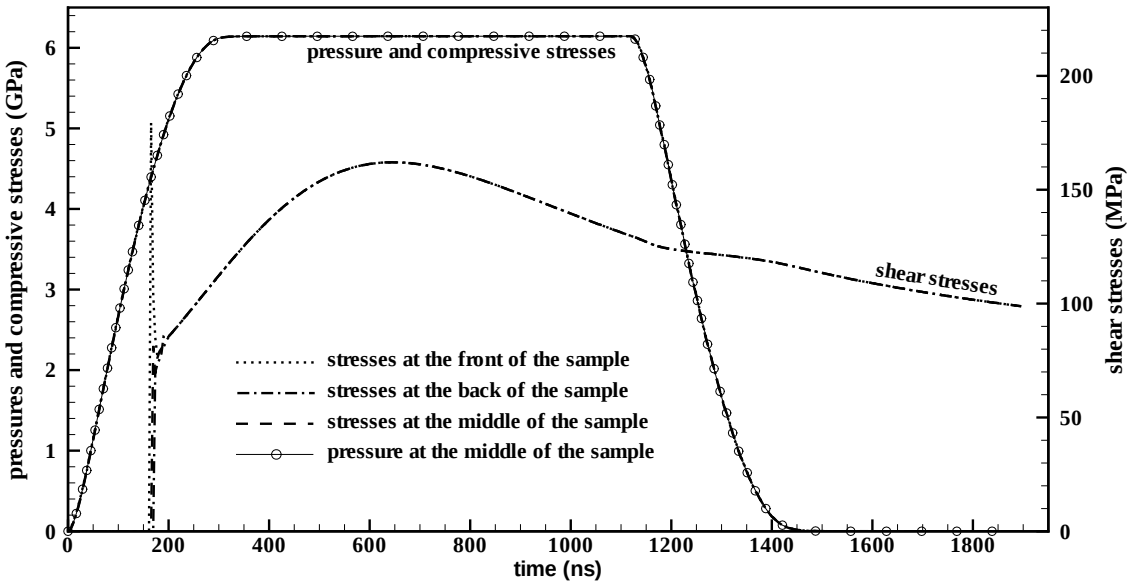

Figure 5.48: Compressive and shear stress simulated using an artificial ramp with the modified Nemat-Nasser/Isaacs model for shot SG0802.

5.4 Adiabatic versus non-adiabatic sample temperature calculations

In Section 4.2.2, the instantaneous sample temperature for each experiment on aluminum was predicted assuming adiabatic conditions. In Section 5.2, the finite difference simulations of these experiments showed that heat conduction can have significant effect on the sample temperature. Since the simulations do not exactly predict the stress-strain response observed in the experiments, the simulated sample temperatures would not be fully accurate estimations of the actual sample temperatures in the experiments. However, the simulated temperature values can provide insight into the degree with which heat conduction plays a role in determining the actual sample temperature. The simulated strains and stresses can used to calculated the sample temperature if adiabatic conditions are assumed. That sample temperature can be compared directly with the temperature of a sample which experiences the same stress-

strain history simulated under non-adiabatic conditions to show the extent to which heat diffusion affects the temperature of a sample.

Taking the compressive stresses, shear stresses and shear strains numerically calculated for shots SG0402, SG0703 and SG0802 – simulated using the modified Nemat-Nasser/Isaacs model – the sample temperatures can be calculated for adiabatic conditions using the method discussed in Section 4.2.2 (Equation (3.16)). This sample temperature predicted using the adiabatic approximation and the temperature calculated at the middle of the sample (under non-adiabatic conditions) are plotted versus time in Figures 5.49, 5.50 and 5.51 for shots SG0402, SG0703 and SG0802 respectively. The melting temperatures calculated using the simulated pressures are also plotted for each shot.

For shot SG0402 (Figure 5.49), the temperature from the full simulation and the temperature obtained with the adiabatic prediction (using simulated strain and stresses) both rise when the longitudinal wave arrives at the sample at time equals zero. The temperature predicted using the adiabatic approximation reaches a higher temperature plateau at around 100 *ns*. This is due to neglecting heat conducted away from the sample into the colder target plates. When the shear wave arrives (~170 *ns*) the temperature predicted using the adiabatic approximation increases steadily due to the plastic work being converted into heat. The sample temperature simulated under non-adiabatic conditions also increases, but at a slower rate. The final sample temperature predicted using the adiabatic approximation is 189^{o}C (462 K) and the final temperature simulated under non-adiabatic conditions reaches 148^{o}C (421 K), which corresponds to 35% and 32% of the current melting temperature respectively. The sample temperature calculated

adiabatically using the simulated strain and stresses over-predicts the simulated sample temperature by approximately 9% for the simulation of shot SG0402 using the modified Nemat-Nasser/Isaacs model.

For shot SG0703 (Figure 5.50), the temperature from the full simulation and the temperature obtained using the adiabatic prediction both rise sharply with the arrival of the longitudinal wave. The temperature predicted using the adiabatic approximation reaches a slightly higher temperature prior to the shear loading. At the arrival of the shear wave (~150 *ns*) the temperature predicted using the adiabatic approximation increases steadily due to the plastic work being converted into heat. The sample temperature simulated under non-adiabatic conditions, however, begins to decrease, which indicates that heat is being conducted away faster than it is being generated by plastic working. The final temperature predicted using the adiabatic approximation is 839^{o}C (1112 K) and the final temperature simulated under non-adiabatic conditions is 766^{o}C (1039 K), which correspond to 84% and 78% of the current melting temperature, respectively. The final sample temperature calculated adiabatically using the simulated strain and stresses over-predicts the final simulated sample temperature by 7% for the simulation of SG0703 using the modified Nemat-Nasser/Isaacs model.

Before the time of the pressure drop for shot SG0802 (~1120 *ns* in Figure 5.51), the temperature response is similar to that of shot SG0703 (Figure 5.50). Both temperatures decrease sharply with the pressure drop and both rise again with further plastic work. Following the pressure drop, the sample temperature simulated under non-adiabatic conditions is actually lower than the surrounding target plates (see Figure 5.41) and heat conducts back into the sample as it continues to generate heat through plastic

work. The final sample temperature predicted using the adiabatic approximation is 651°C (924 K) and the final temperature simulated under non-adiabatic conditions is 617°C (890 K), which is 99.8% and 96.4% of the current melting temperature respectively. The final sample temperature calculated adiabatically using the simulated strain and stresses over-predicts the final simulated sample temperature by 4% for the simulation of SG0802 using the modified Nemat-Nasser/Isaacs model.

This analysis provides insight into how much heat is lost through conduction during the experiment. The results can be used to estimate a more accurate final sample temperature for the experiments. The approximate final sample temperatures are given for each shot in Table 4.4.

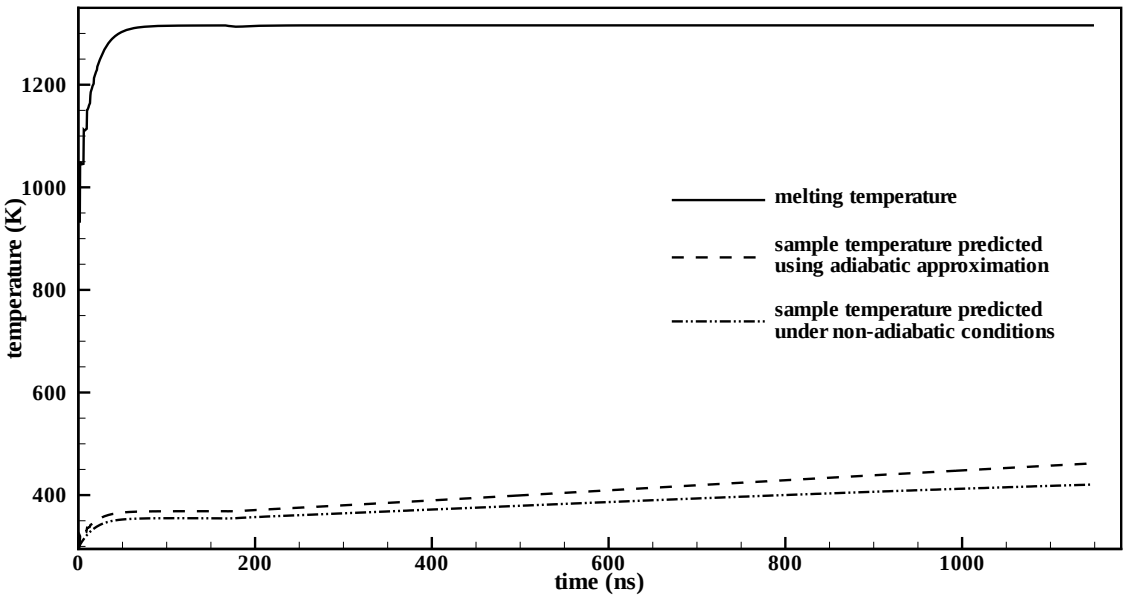

Figure 5.49: Sample temperatures simulated and adiabatically predicted from simulated strain and stresses for shot SG0402 (T_0=22°C) using the modified Nemat-Nasser/Isaacs model.

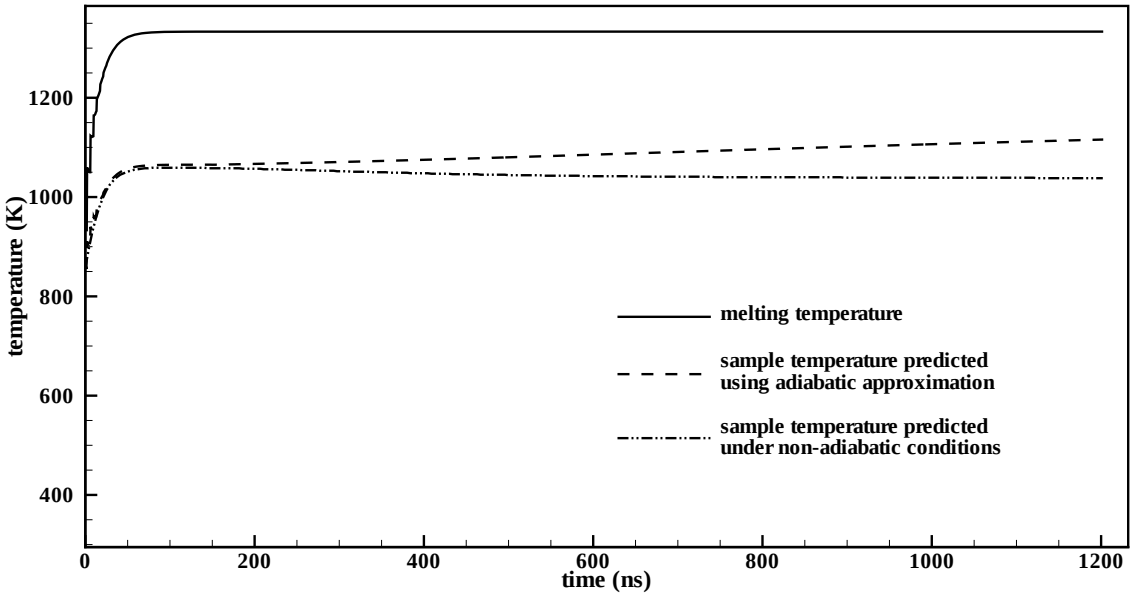

Figure 5.50: Sample temperatures simulated and adiabatically predicted from simulated strain and stresses for shot SG0703 (T_0=584°C) using the modified Nemat-Nasser/Isaacs model.

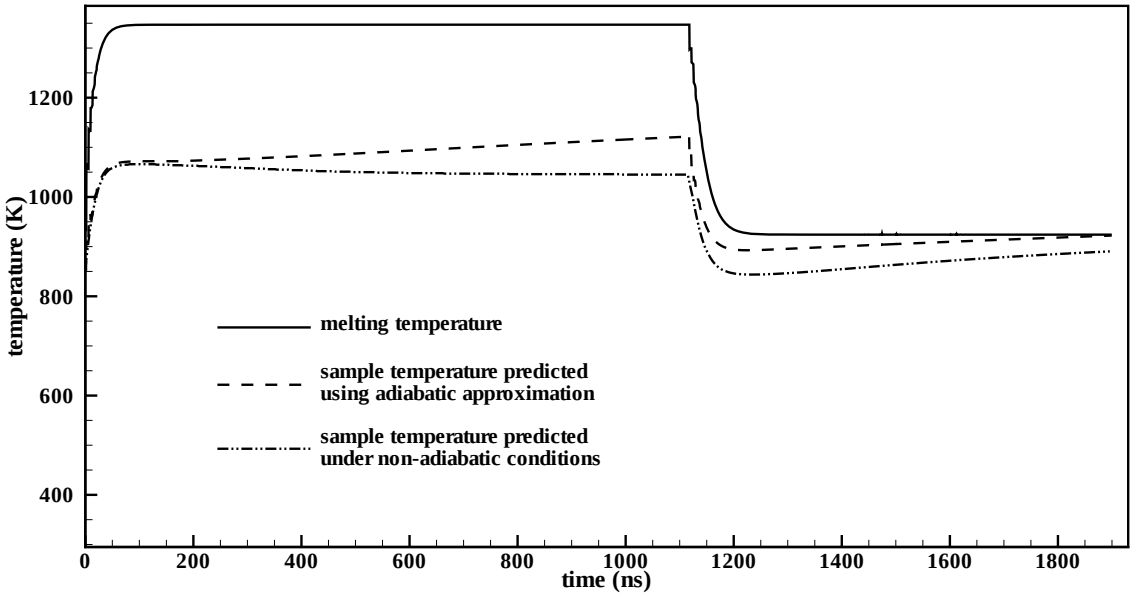

Figure 5.51: Sample temperatures simulated and adiabatically predicted from simulated strain and stresses for shot SG0802 (T_0=582°C) using the modified Nemat-Nasser/Isaacs model.

5.5 Discussion of simulation results

The stress versus time plots for all of the simulations show that the stresses rapidly become uniform through the sample. The strain rates, however, never become uniform in the sample due to the temperature distributions across the sample.

In the experiments, the nominal response of the entire sample is calculated using the velocities measured at the rear surface of the target and the measured projectile velocity. Therefore it was important to simulate the nominal response of the sample so it may be compared with the response at various points in the sample. For all of the simulations, the stresses and strains calculated from the simulated velocities in the target plates provide a good nominal response for the entire sample.

Shot SG0504 was conducted at a starting temperature of 495^{o}C, which is between the starting temperatures of shots SG0402 (T_0=22^{o}C) and SG0703 (T_0=584^{o}C). This shot displayed a lower shearing resistance than the other shots while being deformed at a nominally similar strain rate (see Section 4.2 and Figure 4.30). All of the models presented here produce a monotonic decrease in flow stress with increasing temperature. Therefore, none of the models presented can predict the approximate stress levels of shots SG0402 (T_0=22^{o}C), SG0504 (T_0=5495^{o}C) and SG0703 (T_0=584^{o}C) with a single set of parameters.

Neither the Johnson/Cook model nor the Nemat-Nasser/Isaacs model could accurately simulate the amount of hardening/softening observed in experiments. The strain softening term introduced to the modified Nemat-Nasser/Isaacs model showed that a geometric softening effect is necessary for accurate predictions of the hardening and softening observed in pressure-shear plate impact experiments on high purity aluminum.

Chapter 5 Tables

Table 5.1: Parameters for the Johnson/Cook model

Parameter	value
A	25 MPa
B	175 MPa
C	0.3
n	0.096
m	0.387
$\dot{\varepsilon}_0$	1.82×10^4 s^{-1}
T_0	295 K
T_m (ambient)	933 K
$\dot{\gamma}_0$	1×10^7 s^{-1}
mesh points	500

Table 5.2: Parameters for the Nemat-Nasser/Isaacs model

Parameter	value
τ_a	97 MPa
$\dot{\gamma}_r$	4.99×10^6 s^{-1}
p	0.1
q	1.82
n	0.179
G_0/k	42372 K
$\hat{\tau}$	300 MPa
mesh points	500

Table 5.3: Parameters for the modified Nemat-Nasser/Isaacs model

	SG0402	SG0703 & SG0802
Parameter	**value**	**value**
τ_a	97 MPa	97 MPa
$\dot{\gamma}_r$	4.99×10^6 s^{-1}	4.99×10^6 s^{-1}
p	0.104	0.104
q	2	2
n	0.5	1.1
m	-1.5	-1.8
G_0/k	42372 K	42372 K
$\hat{\tau}$	360 MPa	360 MPa
mesh points	500	500

Chapter 6

Concluding Remarks

The work presented in this thesis was motivated by the desire to improve understanding of the behavior of materials deformed at high rates and at temperatures approaching melt. To this end, high-temperature, pressure-shear plate impact experiments were conducted on high-purity, polycrystalline aluminum. Symmetric impact experiments were also conducted on the tungsten carbide loading plates in order to characterize their response over the range of temperatures and stresses observed in the tests on aluminum.

Experiments were conducted at ultra-high shear strain rates ($1.19 \times 10^6 - 1.85 \times 10^6$ s^{-1}) and at temperatures ranging from room temperature to temperatures that reached approximately 95% of the concurrent melting temperature. The results of the test conducted at room temperature (shot SG0402) were in good agreement with previously reported responses of aluminum. The responses of two elevated temperature tests (SG0703 and SG0802), tested at nominally similar strain rates and starting temperatures, showed excellent agreement prior to the pressure drop in shot SG0802. This agreement indicates good repeatability in high-temperature, pressure-shear plate impact experiments.

As predicted by models based on rate-controlling processes involving the thermally activated motion of dislocations, the shear flow stresses measured at elevated temperatures are notably lower than the flow stresses measured at room temperature. However, the shearing resistance for 99.999% pure aluminum, measured in shot SG0504 (T_0=495^{o}C), is lower than observed for shots SG0703 and SG0802, which were conducted at higher starting temperatures, 584^{o}C and 582^{o}C respectively. This result remains unexplained. Further experiments would be required to see whether or not such a reversal is an anomaly or an indication of a more complicated dependence of flow stress on temperature at high strain rates.

The effect of pressure on the sample temperature and the melting temperature of the sample were considered in this investigation. A pressure-release type experiment was designed and conducted (shot SG0802) in order to measure the shearing resistance of aluminum at lower pressures and correspondingly lower melting temperatures. The shearing resistance was measured in this test (shot SG0802) as the sample temperature reached approximately 95% of the melting temperature. The measured resistance to shearing deformation was shown to be remarkably high for temperatures in such close proximity to the melting temperature. Because the reduction in pressure resulted in a rapid drop in the temperature this experiment can also be viewed as a 'temperature-change' experiment in which the flow stress is measured continuously as the temperature changes quickly. Such temperature-change experiments have been notably difficult to do at high strain rates because of the time required for heat conduction. The measurements reported here may have fundamental implications for the form of constitutive equations

to describe the mechanical response of metals at high strain rates and elevated temperatures.

A modified version of the Nemat-Nasser/Isaacs constitutive model has been proposed to explain the observed experimental behavior. The model incorporates the mechanism of geometric softening and does an adequate job of capturing the hardening/softening observed experimentally. Even better agreement of the details of the shearing response may be possible by accounting for the nonlinearity of the response of the tungsten carbide plates.

References

Abousayed, A. S., Clifton, R. J., and Hermann, L. (1976). "Oblique-Plate Impact Experiment." *Experimental Mechanics*, 16(4), 127-132.

Boehler, R., and Ross, M. (1997). "Melting curve of aluminum in a diamond cell to 0.8 Mbar: implications for iron." *Earth and Planetary Science Letters*, 153(3-4), 223-227.

Brooks, C. R., and Bingham, R. E. (1968). "The specific heat of aluminum from 330 to 890°K and contributions from the formation of vacancies and anharmonic effects." *Journal of Physics and Chemistry of Solids*, 29(9), 1553-1560.

Clifton, R. J., and Bodner, S. R. (1966). "Analysis of Longitudinal Elastic-Plastic Pulse Propagation." *Journal of Applied Mechanics*, 248-255.

Dawhil, W., and Mal, M. K. (1965). "Contribution to the Study of the Deformation Behaviour and Structure of WC-TiC-TaC-Co Alloys." *Cobalt*, 26, 25-35.

DeSorbo, W., and Turnbull, D. (1959). "Kinetics of Vacancy Motion in High-Purity Aluminum." *Physical Review*, 115(3), 560.

Duprey, K. (1999). "High Strain Rate Constitutive Response of Thin Tantalum Foils and Tungsten Heavy Alloys," Ph.D. thesis, Brown University, Providence, RI.

Escobar, J. C., and Clifton, R. J. "Pressure-shear impact-induced phase transformations in Cu-14.44Al-4.19Ni single crystals." *Active Materials and Smart Structures*, College Station, TX, USA, 186-197.

Espinosa, H. D. (1992). "Micromechanics of the dynamic response of ceramics and ceramics composites," Ph.D. thesis, Brown University, Providence, RI.

Espinosa, H. D., Mello, M., and Xu, Y. (1996). "A desensitized displacement interferometer applied to impact recovery experiments." *Applied Physics Letters*, 69(21), 3161-3163.

Federighi, T. (1959). "A possible determination of the activation energy for self-diffusion in aluminium." *Philosophical Magazine*, 4, 502-510.

Feltham, P., and Copley, G. J. (1958). "Grain-growth in [alpha]-brasses." *Acta Metallurgica*, 6(8), 539-542.

Frutschy, K. J. (1996). "Plate impact facility lab book." Brown University, Providence, RI.

Frutschy, K. J. (1997). "High-Temperature Pressure-Shear Plate Impact Experiments on OFHC Copper and Pure Tungsten Carbide," Ph.D. thesis, Brown University, Providence, RI.

Frutschy, K. J., and Clifton, R. J. (1998a). "High-temperature pressure-shear plate impact experiments on ofhc copper." *Journal of the Mechanics and Physics of Solids*, 46(10), 1723-1744.

Frutschy, K. J., and Clifton, R. J. (1998b). "High-temperature pressure-shear plate impact experiments using pure tungsten carbide impactors." *Experimental Mechanics*, 38(2), 116-125.

Gilat, A., and Clifton, R. J. (1985). "Pressure-shear waves in 6061-T6 aluminum and alpha-titanium." *Journal of the Mechanics and Physics of Solids*, 33(3), 263-284.

Gust, W. H. (1982). "High impact deformation of metal cylinders at elevated temperatures." *Journal of Applied Physics*, 53(5), 3566-3575.

Hauser, F. E., Simmons, J. A., and Dorn, J. E. (1961). "Strain Rate Effects in Plastic Wave Propagation." Response of Metals to High Velocity, Interscience, NY, 93-114.

Holt, D. L., Babcock, S. G., and Green, S. J. (1967). "The strain-rate dependence of the flow stress in some aluminum alloys." *Trans. of the ASM*, 60, 152-159.

Huang, S. H. (1986). "Plate impact facility lab book." Brown University, Providence, RI.

Jiao, T., Clifton, R. J., and Grunschel, S. E. (2007). "Pressure-sensitivity and tensile strength of an elastomer at high strain rates." *Aip Conference Proceedings*, 955(1), 707-710.

Johnson, G. R., and Cook, W. H. (1985). "Fracture characteristics of three metals subjected to various strains, strain rates, temperatures and pressures." *Engineering Fracture Mechanics*, 21(1), 31-48.

Kim, K. S., Clifton, R. J., and Kumar, P. (1977). "Combined Normal-Displacement and Transverse-Displacment Interferometer with an Application to Impact of y-cut Quartz " *Journal of Applied Physics*, 48(10), 4132-4139.

Klopp, R. W. (1987). "Plasticity of Aluminum and Iron at High Shear Strain Rate and High Pressure," Ph.D. thesis, Brown University, Providence, RI.

Klopp, R. W., and Clifton, R. J. (1990). "Analysis of tilt in the high-strain-rate pressure-shear plate impact experiment " *Journal of Applied Physics*, 67(11), 7171-7173.

Klopp, R. W., Clifton, R. J., and Shawki, T. G. (1985). "Pressure-shear impact and the dynamic viscoplastic response of metals." *Mechanics of Materials*, 4(3-4), 375-385.

Kocks, U. (1976). "Laws for work-hardening and low-temperature creep." *ASME J. Eng. Mater. Technol.*, 98, 76-85.

Kuchhal, P., Kumar, R., and Dass, N. (1997). "Temperature-dependent equation of state of condensed matter." *Journal of Physics: Condensed Matter*, 9(14), 2987-2998.

Kuchhal, P., Kumar, R., and Dass, N. (1998). "Pressure and temperature dependence of heat capacity and entropy in condensed matter." *Journal of Physics: Condensed Matter*, 10(35), L603-L606.

Kumar, P., and Clifton, R. J. (1977). "Optical alignment of impact faces for plate impact experiments " *Journal of Applied Physics*, 48(3), 1366-1367.

Kumari, M., and Dass, N. (1990). "An equation of state applied to sodium chloride and caesium chloride at high pressures and high temperatures." *Journal of Physics: Condensed Matter*, 2(14), 3219-3229.

Li, C. H., and Clifton, R. J. (1981). "Dynamic stress-strain curves at plastic shear strain rates of 105s-1." *Bulletin of the American Physical Society*, 26(4), 658-658.

Lindholm, U. S., and Yeakley, L. M. (1965). "Dynamic deformation of single and polycrystalline aluminium+." *Journal of the Mechanics and Physics of Solids*, 13(1), 41-53.

Lundy, T. S., and Murdock, J. F. (1962). "Diffusion of Al26 and Mn54 in Aluminum." *Journal of Applied Physics*, 33(5), 1671-1673.

Meyers, M. A., Nesterenko, V. F., LaSalvia, J. C., and Xue, Q. (2001). "Shear localization in dynamic deformation of materials: microstructural evolution and self-organization." *Materials Science and Engineering A*, 317(1-2), 204-225.

Morrone, A. (1986). "Strain Rate and Temperature Effects During Dynamic Deformation of Polycrystalline and Monocrystalline High Purity Aluminum Including TEM Studies," Ph.D. thesis, Brown University, Providence, RI.

Morrone, A., and Duffy, J. (1986). "Strain rate and temperature effects during dynamic deformation of polycrystalline and monocrystalline high purity aluminum including TEM studies." Report, Division of Engineering, Materials Research Laboratory, Brown University.

Nemat-Nasser, S., and Guo, W. (2000). "High strain-rate response of commercially pure vanadium." *Mechanics of Materials*, 32(4), 243-260.

Nemat-Nasser, S., and Isaacs, J. B. (1997). "Direct measurement of isothermal flow stress of metals at elevated temperatures and high strain rates with application to Ta and TaW alloys." *Acta Materialia*, 45(3), 907-919.

Nowak, W. (1976). "Discussion of grain growth in aluminum." *Metallurgical and Materials Transactions a-Physical Metallurgy and Materials Science*, 7A, 1503-1509.

Prakash, V. (1993). "Plate impact investigations of dynamic fracture initiation and time-resolved friction," Ph.D. thesis, Brown University, Providence, RI.

Raju, S., Sivasubramanian, K., and Mohandas, E. (2002). "The high temperature bulk modulus of aluminium: an assessment using experimental enthalpy and thermal expansion data." *Solid State Communications*, 122(12), 671-676.

Ramesh, K. T., and Clifton, R. J. (1987). "A pressure-shear plate impact experiment for studying the rheology of lubricants at high-pressures and high shearing rates." *Journal of Tribology-Transactions of the Asme*, 109(2), 215-222.

Ramesh, K. T., and Clifton, R. J. (1992). "Finite Deformation Analysis of Pressure-Shear Plate Impact Experiments on an Elastohydrodynamic Lubricant." *Journal of Applied Mechanics*, 59(4), 754-761.

Ranganath, S., and Clifton, R. J. (1972). "A second-order accurate difference method for systems of hyperbolic partial differential equations." *Computer Methods in Applied Mechanics and Engineering*, 1(2), 173-188.

Ravichandran, G. (1987). "Dynamic fracture under plane wave loading," Ph.D. thesis, Brown University, Providence, RI.

Seo, S., Min, O., and Yang, H. (2005). "Constitutive equation for Ti-6Al-4V at high temperatures measured using the SHPB technique." *International Journal of Impact Engineering*, 31(6), 735-754.

Shawki, T. G., and Clifton, R. J. (1989). "Shear band formation in thermal visco-plastic materials." *Mechanics of Materials*, 8(1), 13-43.

Sundaram, S. (1994). "Shearing resistance of ceramic powder under high pressures and high shear rates," Sc.M. thesis, Brown University, Providence, RI.

Sundaram, S. (1998). "Pressure-shear plate impact studies of alumina ceramics and the influence of an intergranular glassy phase," Ph.D. thesis, Brown University, Providence, RI.

Syassen, K., and Holzapfel, W. B. (1978). "Isothermal compression of Al and Ag to 120 kbar." *Journal of Applied Physics*, 49(8), 4427-4430.

Tanaka, K., Nojima, T., and Kinoshita, M. (1970). "The effect of temperature and strain rate on the strength of aluminum." *Proceedings 13th Japan Congress on Materials Research, Soc. of Mat. Sci., Japan - Kyoto*, 101-105.

Tong, W., Clifton, R. J., and Huang, S. (1992). "Pressure-shear impact investigation of strain rate history effects in oxygen-free high-conductivity copper." *Journal of the Mechanics and Physics of Solids*, 40(6), 1251-1294.

Trozera, T. A., Sherby, O. D., and Dorn, J. E. (1957). "Effect of strain rate and temperature of the plastic deformation onf high purity aluminum." *Trans. of the ASM*, 49, 1750-1754.

Yoshida, S., and Nagata, N. (1966). "Deformation of Polycrystalline Aluminum at High Strain Rates." *Trans. Japan Inst. Met.*, 7, 273-279.

Zhang, Z., and Clifton, R. J. (2003). "Shear band propagation from a crack tip." *Journal of the Mechanics and Physics of Solids*, 51(11-12), 1903-1922.

Zhou, M. (1993). "Dynamic shear localization in a tungsten heavy alloy and ductile rupture in a spheroidized 1045 steel," Ph.D. thesis, Brown University, Providence, RI.